WL-TR-93-1133

AD-A282 540

WIDEBAND ELECTROMAGNETIC SCATTERING
PROGRAM

FOURIER-BASED RADAR IMAGING TECHNIQUES

B.L. CHAN, J.D. YOUNG AND R.C. RUDDUCK

THE OHIO STATE UNIVERSITY
ELECTROSCIENCE LABORATORY
1320 KINNEAR ROAD
COLUMBUS, OHIO 43212

DTIC
S ELECTE
JUL 2 6 1994
F

SEPTEMBER 1993

INTERIM REPORT FOR 05/01/92–05/01/93
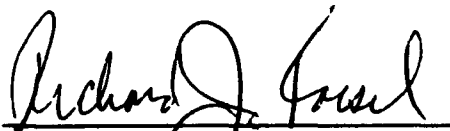
APPROVED FOR PUBLIC RELEASE; DISTRIBUTION IS UNLIMITED.

AVIONICS DIRECTORATE
WRIGHT LABORATORY
AIR FORCE MATERIEL COMMAND
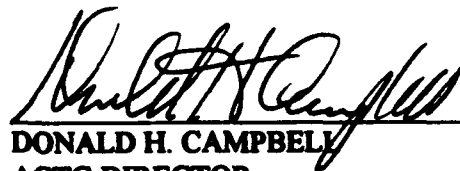WRIGHT-PATTERSON AIR FORCE BASE, OHIO 45433-7409

94 7 25 161

NOTICE

WHEN GOVERNMENT DRAWINGS, SPECIFICATIONS, OR OTHER DATA ARE USED FOR ANY PURPOSE OTHER THAN IN CONNECTION WITH A DEFINITELY GOVERNMENT-RELATED PROCUREMENT, THE UNITED STATES GOVERNMENT INCURS NO RESPONSIBILITY OR ANY OBLIGATION WHATSOEVER. THE FACT THAT THE GOVERNMENT MAY HAVE FORMULATED OR IN ANY WAY SUPPLIED THE SAID DRAWINGS, SPECIFICATIONS, OR OTHER DATA, IS NOT TO BE REGARDED BY IMPLICATION, OR OTHERWISE IN ANY MANNER CONSTRUED, AS LICENSING THE HOLDER, OR ANY OTHER PERSON OR CORPORATION; OR AS CONVEYING ANY RIGHTS OR PERMISSION TO MANUFACTURE, USE, OR SELL ANY PATENTED INVENTION THAT MAY IN ANY WAY BE RELATED THERETO.

THIS TECHNICAL REPORT HAS BEEN REVIEWED AND IS APPROVED FOR PUBLICATION.

RICHARD J. KOESEL
PROJECT ENGINEER

DENNIS M. MUKAI, SEC CHIEF
TECHNOLOGY DEVELOPMENT SECTION

DONALD H. CAMPBELL
ACTG DIRECTOR
MISSION AVIONICS DIVISION
AVIONICS DIRECTORATE

IF YOUR ADDRESS HAS CHANGED, IF YOU WISH TO BE REMOVED FROM OUR MAILING LIST, OR IF THE ADDRESSEE IS NO LONGER EMPLOYED BY YOUR ORGANIZATION, PLEASE NOTIFY WL/AARM-1, WRIGHT-PATTERSON AFB OH 45433-7408 TO HELP MAINTAIN A CURRENT MAILING LIST.

COPIES OF THIS REPORT SHOULD NOT BE RETURNED UNLESS RETURN IS REQUIRED BY SECURITY CONSIDERATIONS, CONTRACTUAL OBLIGATIONS, OR NOTICE ON A SPECIFIC DOCUMENT.

REPORT DOCUMENTATION PAGE

Public reporting burden for this collection of information is estimated to average 1 hour per response, including the time for reviewing instructions, searching existing data sources, gathering and maintaining the data needed, and completing and reviewing the collection of information. Send comments regarding this burden estimate or any other aspect of this collection of information, including suggestions for reducing this burden, to Washington Headquarters Services, Directorate for Information Operations and Reports, 1215 Jefferson Davis Highway, Suite 1204, Arlington, VA 22202-4302, and to the Office of Management and Budget, Paperwork Reduction Project (0704-0188), Washington, DC 20503

1. AGENCY USE ONLY (Leave blank)	2. REPORT DATE SEP 1993	3. REPORT TYPE AND DATES COVERED INTERIM 05/01/92--05/01/93

4. TITLE AND SUBTITLE WIDEBAND ELECTROMAGNETIC SCATTERING PROGRAM FOURIER-BASED RADAR IMAGING TECHNIQUES	5. FUNDING NUMBERS C F33615-91-C-1729 PE 62204 PR 7622
6. AUTHOR(S) B.L. CHAN, J.D. YOUNG, R.C. RUDDUCK	TA 07 WU 71

7. PERFORMING ORGANIZATION NAME(S) AND ADDRESS(ES) OHIO STATE UNIVERSITY ELECTRO-SCIENCE LABORATORY 1320 KINNEAR ROAD COLUMBUS, OHIO 43212	8. PERFORMING ORGANIZATION REPORT NUMBER 724733-2

9. SPONSORING MONITORING AGENCY NAME(S) AND ADDRESS(ES) AVIONICS DIRECTORATE WRIGHT LABORATORY AIR FORCE MATERIEL COMMAND WRIGHT PATTERSON AFB OH 45433-7409	10. SPONSORING/MONITORING AGENCY REPORT NUMBER WL-TR-93-1133

11. SUPPLEMENTARY NOTES

12a. DISTRIBUTION/AVAILABILITY STATEMENT APPROVED FOR PUBLIC RELEASE; DISTRIBUTION IS UNLIMITED.	12b. DISTRIBUTION CODE

13. ABSTRACT (Maximum 200 words)

This report describes the implementation of Fourier based radar imaging algorithms in a computer program. In particular, the algorithms are derived for wide bandwidth and for specific geometries. These geometries are often measured by radar cross section measurement systems such as compact ranges and near field linear synthetic aperture radar systems. The limitations of different implementations of the algorithms are presented. Imaging results from radar measurements are also presented for an F-4 fighter aircraft, an M35 truck (1/16 scale model), and a forest.

14. SUBJECT TERMS			15. NUMBER OF PAGES 103
			16. PRICE CODE

17. SECURITY CLASSIFICATION OF REPORT UNCLASSIFIED	18. SECURITY CLASSIFICATION OF THIS PAGE UNCLASSIFIED	19. SECURITY CLASSIFICATION OF ABSTRACT UNCLASSIFIED	20. LIMITATION OF ABSTRACT UL

Contents

Figures

Tables

SECTION 1

Introduction

Radar imaging is used to identify scattering centers in a target region. In most current implementations of radar imaging, the images are generated using narrow bandwidth data for far-field targets which are hundreds of wavelength in size. In addition, the target response is usually limited to a narrow angular region because a limited aperture is used. Thus, these images are generated using approximations that are valid for far-field narrowband data with very large targets. In contrast, the characterization of the scattering centers in this study is done over a large bandwidth and wide aperture, for relatively small target sizes ranging from 1/60 to 20 wavelengths. Under these conditions, the approximations used in far-field narrowband limited aperture imaging are not necessarily valid. Furthermore, dispersion in frequency and angle might invalidate imaging as a useful scattering diagnostic technique.

A computer program was developed for generating monostatic coherent radar images using large bandwidth and wide aperture data. The program uses Fourier based methods for producing the image. Fourier based imaging has advantages for several reasons. First, it is widely used and serves as a basis of comparison to other imaging techniques. More importantly, the frequency and angle characteristics of the scattering centers are preserved in the image, so that the radar cross section,

1

of a specific scattering center, can be generated from the image by windowing and transforming back into the data domain.

In developing the computer program, different Fourier based algorithms are needed because the different scanning geometries are used to measure the radar cross section. Chapter 2 describes the different measurement systems that the program was written for. Chapter 3 contains an overview of the imaging algorithm and details of its implementation. Since the images are Fourier based, Gibb's phenomena will be present in each image. Consequently, a brief discussion of two-dimensional filtering techniques to remove the Gibb's phenomena are presented in Chapter 4. In Chapter 5, imaging results are shown for an F-4 Phantom model, an M35 truck model, and foliage. Overall conclusions are given in Chapter 6.

SECTION 2

Measurement of Radar Cross Section

2.1   OSU Compact Range

Many of the radar cross section measurements were done in the Ohio State University's compact range. The compact range is shown in Figure 1. The range may be set up in several configurations.

The typical configuration is shown in Figure 1. In this configuration, the range uses a parabolic reflector to illuminate targets with a plane wave. As seen in Figure 2, the antenna feed is placed at the focal point of the parabolic reflector. The transmitted spherical wave is converted to a plane wave by the reflector. As a result, the targets can be studied in the far field.

The targets are placed on a metal ogival pylon located in the center of an anechoic chamber. By placing targets on the pylon, the target may be rotated by computer control by machinery inside the pylon. This allows the user to conveniently measure the radar cross section, RCS, vs look angle of a target in a polar coordinate system. Each look angle of the target is characterized by its orientation in elevation angle, θ, and in azimuth, ϕ. The target has an associated RCS, $\sigma(\omega)$, that is frequency dependent. By associating target orientation and RCS frequency dependency, one can define a data space, $\sigma(\omega, \theta, \phi)$. By placing the target at various elevation angles,

3
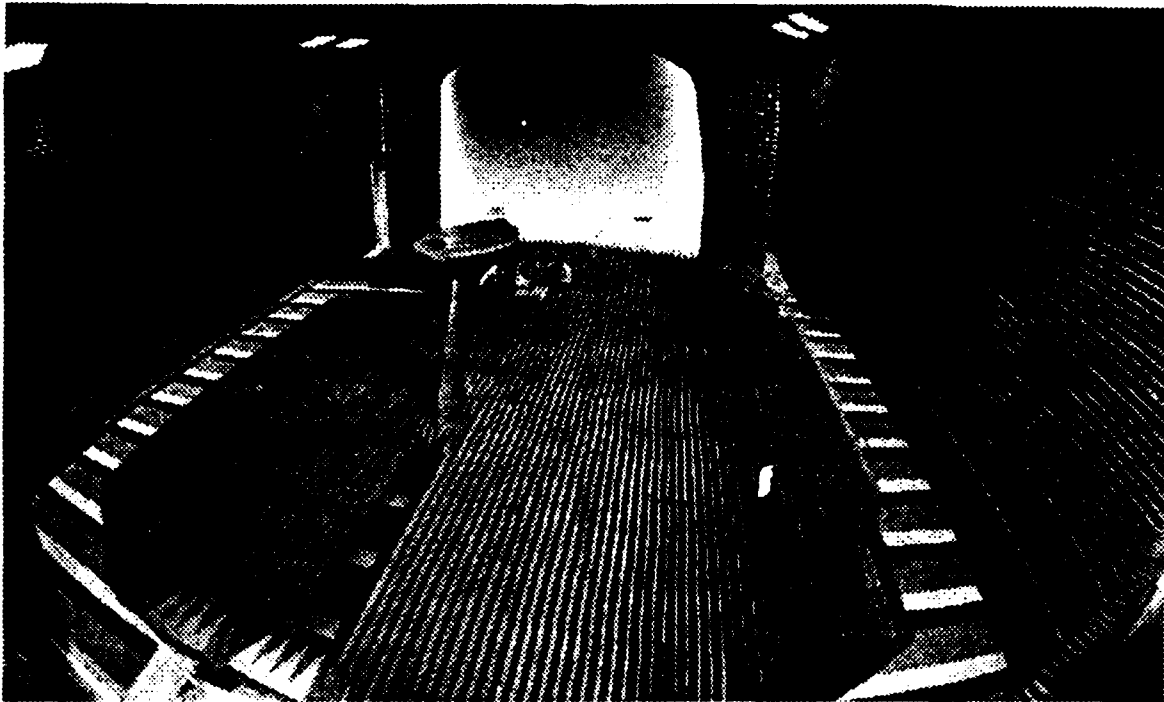
Figure 1: OSU Compact Range
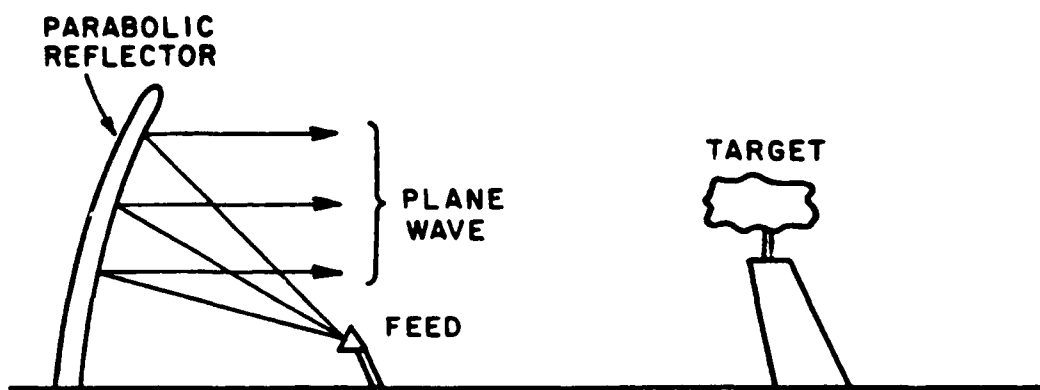
Figure 2: Operation of the Compact Range

this configuration measures the points in the data space located in a plane containing the origin of the data space.

This data space is measured by a continuous wave stepped frequency radar system. Figure 3 shows a block diagram of the system. Further information on the OSU radar may be found in Reference [1].

By placing a metal ground plane on the ogive, the range can measure conical cuts of the data space. The ground plane fixture may be tilted up to 60 degrees. In this configuration, the ground plane can be rotated under computer control. This rotation causes the data to be measured at a constant elevation angle with respect to the ground plane (θ is a constant). The mounted ground plane is shown in Figure 4.

By using an automated system, one can easily obtain large amounts of data. For the system used here, the data are directly sent from radar computer to either an XD88 Tektronix workstation or a VAX 8550. By sending data directly to these computer systems, the data may be immediately processed to provide the RCS in dBsm.

2.2 "Big Ear" Compact Range

The OSU compact range can measure targets up to 10 feet in length. For larger targets, RCS measurements can be measured at The Ohio State University's Radio Observatory designed by Professor John Kraus and known as "Big Ear." A photograph of the observatory is shown in Figure 5. The Big Ear can be used as a compact range because it is designed to reflect an incoming signal from the sky by using a flat reflector. The reflected wave is focussed by a parabolic reflector into an antenna feed. This process is illustrated in Figure 6.

The "Big Ear" can be used in a similar manner as the OSU compact range. This similarity can be achieved by correctly positioning the antennas at the focal distance of the parabolic reflector, but offset from the symmetry axis. The transmitted spherical wave strikes the parabolic reflector, which converts it to a plane wave.
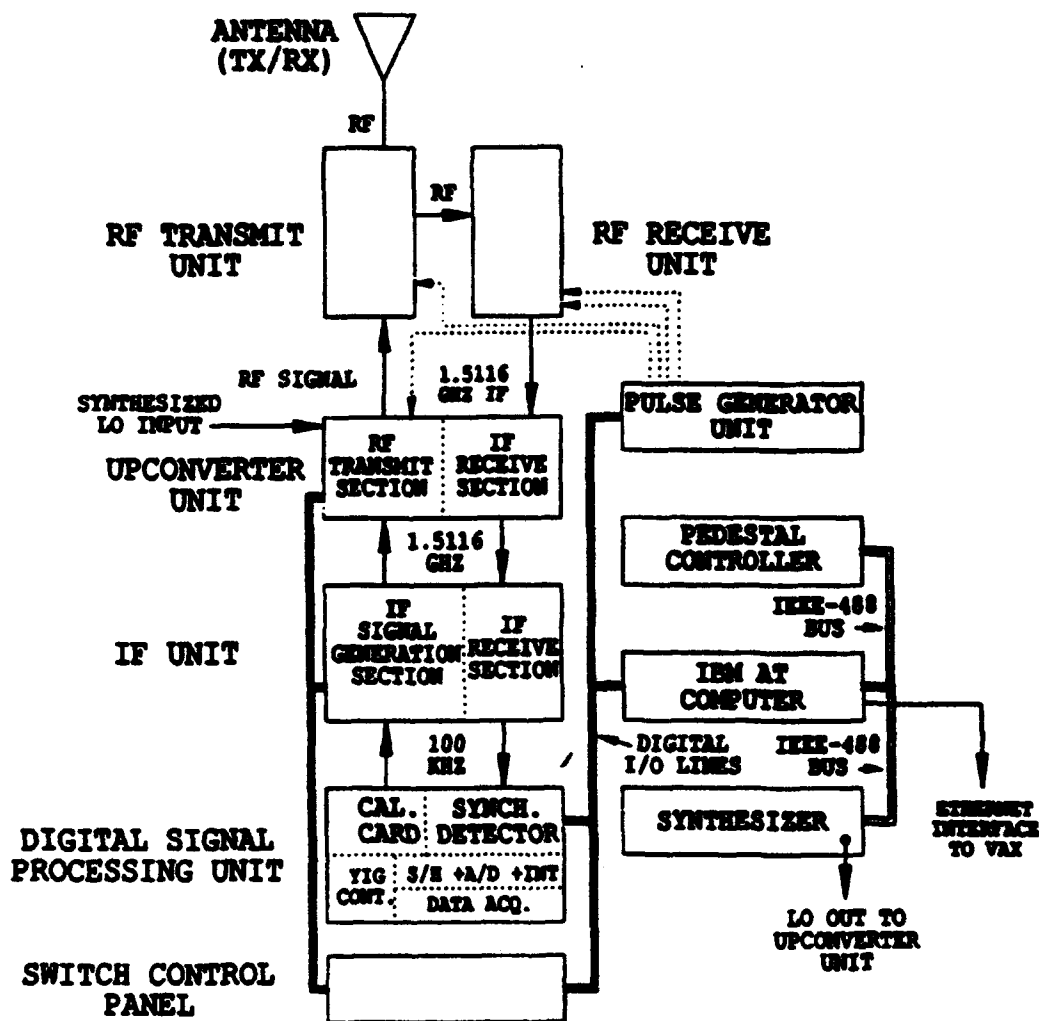
Figure 3: Block Diagram of the OSU Radar System

Figure 4: Ground Plane Mount
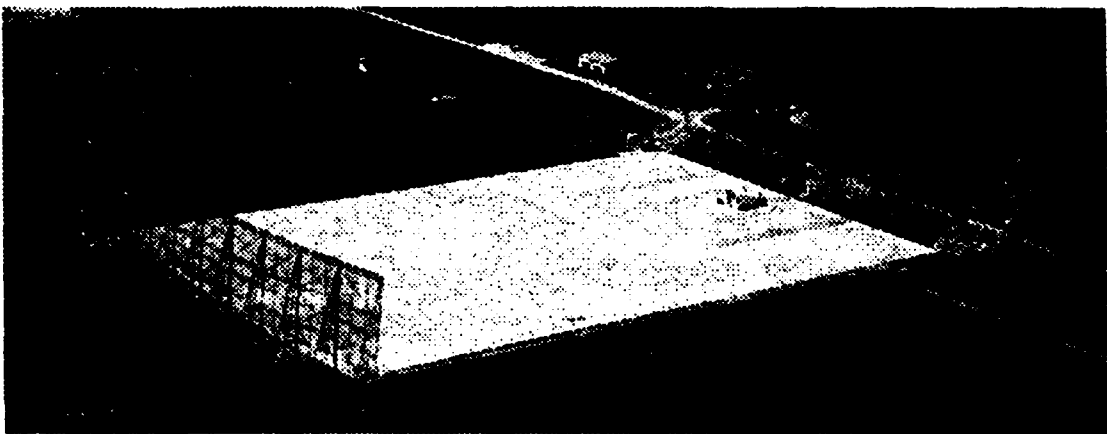
Figure 5: Big Ear Radio Observatory.
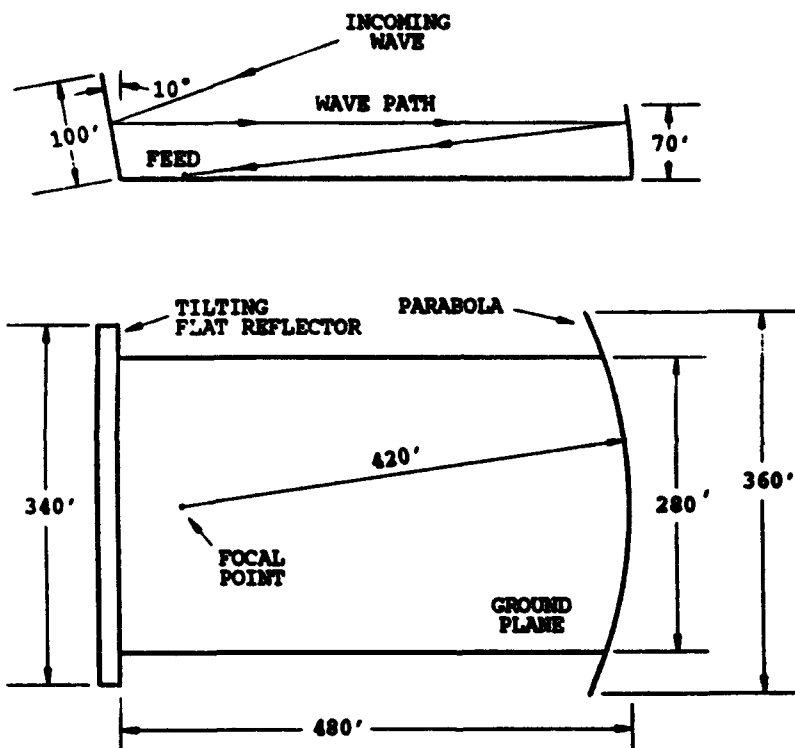
Figure 6: Operation of the "Big Ear" as a Radio Telescope

The plane wave strikes the target and reflects energy back to the parabolic reflector. This reflection focuses the energy back to the feed antenna. This process is illustrated in Figure 7. The Big Ear works well in vertical polarization, VP. Measurements for horizontal polarization, HP, may be made in a similar manner with some difficulties. These difficulties arise because of the antenna. In order to radiate an HP wave, the antenna cannot be placed on the conducting ground plane. As a result, the HP antenna must be suspended in the air which causes a ground bounce. The ground bounce must be eliminated in order to obtain the true RCS of the target.

Measurements made at the Big Ear are done using a novel radar system. The radar is a stepped-frequency system that operates from 47.3 MHz to 2.0473 GHz. Measurements made at the Big Ear are much more difficult because of several factors such as weather and radio frequency interference. The use of the Big Ear system as a compact range is also discussed in References [2] and [3].

2.3 Synthetic Aperture Radar at the "Big Ear"

While the parabolic reflector is used to simulate the far-field, the parabolic reflector is not used in synthetic aperture radar (SAR) measurements. The flat reflector is used in the SAR measurements only to provide a stable rail system in which a linear aperture is synthesized.

Figure 8 shows a rail located at the top of the flat reflector. This rail is used to support a cart containing the antennas and radar system. As seen in Figure 9, two rhombic antennas are mounted on the cart. The rhombic antenna pattern information may be found in [4]. Both time domain and frequency domain radar systems can be mounted on the cart. The basic block diagram for the frequency domain radar system is shown in Figure 10.

Figure 11 shows the basic configuration of the system. As seen in the figure, a pair of antennas are free to move along a track. One can make RCS measurements anywhere along the track. Under the assumption that the target region is stable,

9

FEED POSITION #1
(VP MEASUREMENTS ONLY)

GRAZING ANGLE FEED LOCATION

FEED POSITION #2
(HP & VP MEASUREMENTS)

SHALLOW DEPRESSION ANGLE FEED LOCATION

PTZ

FOCAL POINT

250'

VERTEX

ATZ

10°

100'

420'

FEED POSITION #1

FEED POSITION #2
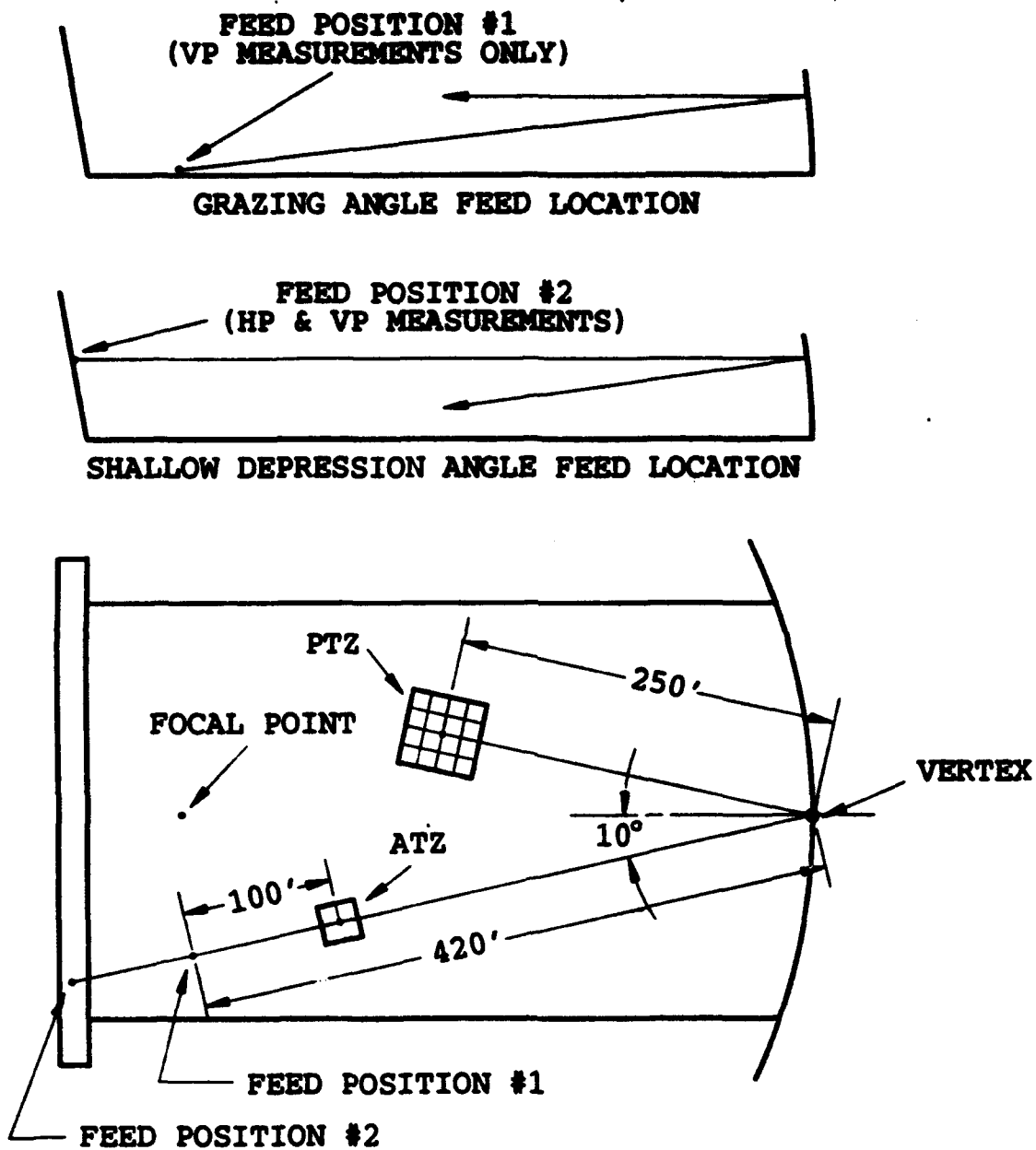
Figure 7: Operation of the "Big Ear" as a Compact Range

10
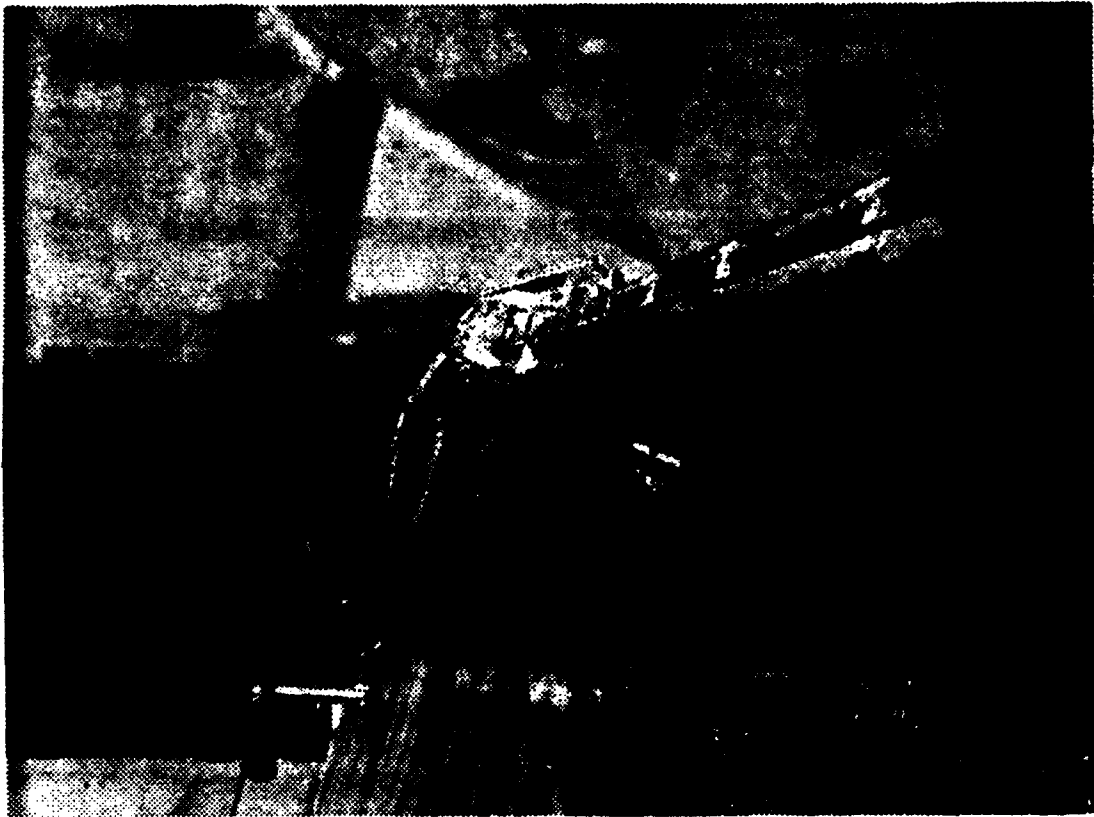
Figure 8: Big Ear Rail Used as a Support Structure for an SAR Radar

11

Figure 9: Rhombic Antennas Used for SAR Measurements at the "Big Ear"

Figure 10: Block Diagram of the Frequency Domain Radar Used in "Big Ear" SAR Measurement

Figure 11: SAR Geometry at the "Big Ear"

the system can behave as an SAR system, if multiple measurements are done along the track and the data are processed.

2.4 Calibration

The raw data contain the radar system response which can normally be removed by a calibration procedure. If $\Gamma(t)$ is the range and phase normalized complex scattering amplitude, $h(t)$, the lumped system transfer function, then the resulting measured data, $m(t)$, has a response of $\Gamma(t) * h(t)$, where $*$ denotes a convolution. As a result, the system response must be deconvolved. The deconvolution may be done as a simple division in the frequency domain[7] which results in

$$\Gamma(\omega) = \frac{M(\omega)}{H(\omega)} \tag{1}$$

One method of determining the system response is by measuring a target with a theoretically known normalized response, $\Gamma_e(t)$. The system response may be simply determined by deconvolution of the measured data, $M_e(t)$ with the known theoretical response. In the frequency domain, deconvolution is done by

$$\frac{M_e(\omega)}{\Gamma_e(\omega)} = \frac{\Gamma_e(\omega) \cdot H(\omega)}{\Gamma_e(\omega)} = H(\omega) \tag{2}$$

Theoretically, the deconvolution can easily be done. In practice, the deconvolution by $\Gamma_e(\omega)$ is difficult when there are nulls in $\Gamma_e(\omega)$. Therefore, the selection of a calibration target is extremely important. The calibration target should not contain any nulls. Figures 12 and 13 show the frequency response of a 2-foot trihedral corner reflector which was used in the calibration of the Big Ear SAR measurements.

The lumped system response contains many hidden dependencies. For example, the response of $H(\omega)$ contains the free space propagation loss at the range distance of the calibration target. This propagation loss factor is usually not a problem in compact range measurements because the illuminating wave is a plane wave and the target is at the same range as the calibration target. For large downrange profiles, the propagation loss may be compensated by range processing after calibration [5].

14
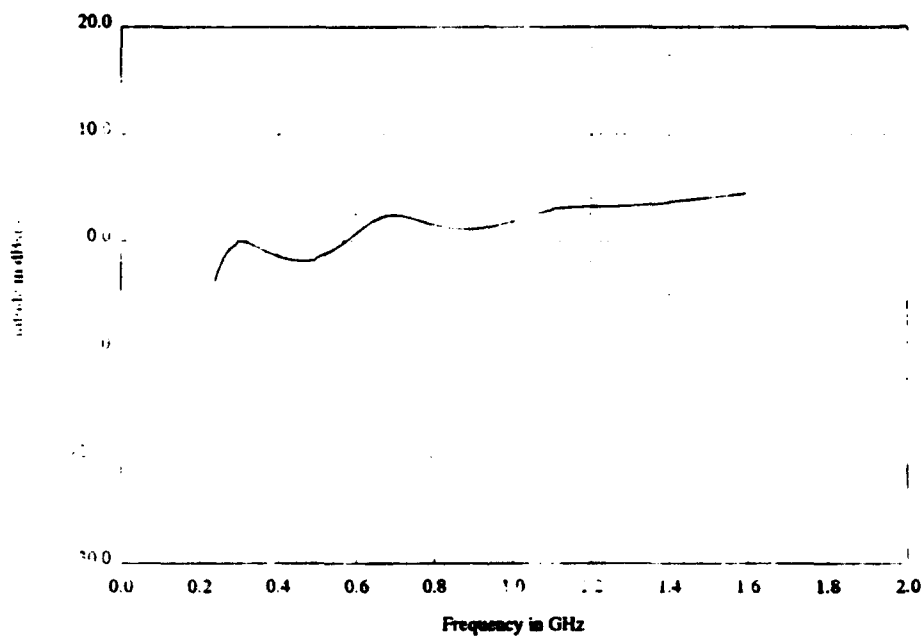
Figure 12: Theoretical RCS of a 2-Foot Dihedral for the Electric Field Perpendicular to the Dihedral Joint
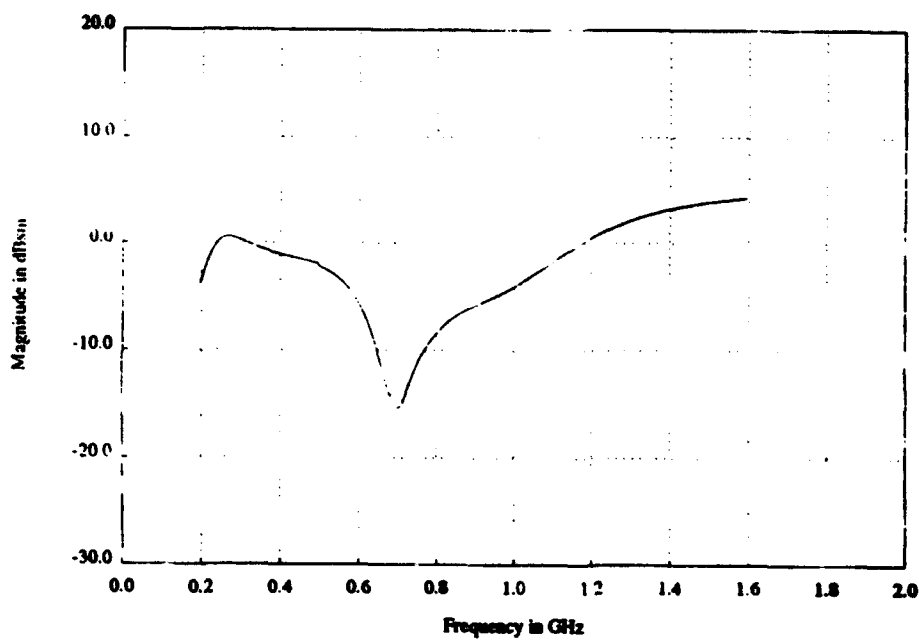
Figure 13: Theoretical RCS of a 2-Foot Dihedral for the Electric Field Parallel to the Dihedral Joint.

16

Deconvolution usually requires a large signal to noise ratio. However, most measurements are usually clutter limited. One technique for reducing clutter is background subtraction. In using background subtraction, several assumptions need to be made. The assumptions are [6] :

1.   Interactions between the target and background
      are negligible.
2.   Th⌐ background remains unchanged during the measurements.
3.   A stable radar system is used.

If these assumptions are valid, then the target background measurement, $T^b(\omega)$, and the reference target background measurement, $C^b(\omega)$ respectively, may be subtracted from the target measurement, $T^t(\omega)$, and calibration measurement, $C^c(\omega)$, to give effective target, $M^t(\omega)$, and effective calibration measurements, $M^c(\omega)$, given in the following equations:

$$M^t(\omega) = T^t(\omega) - T^b(\omega) \tag{3}$$

$$M^c(\omega) = C^c(\omega) - C^b(\omega) \tag{4}$$

For the reference target measurements, if the subtraction does not work well outside the target zone, then errors in determining the system transfer function occur. In order to minimize the error, one may observe the target response in the time domain if the subtraction is working well in the target region. Since the data returned by the continuous wave radar are in the frequency domain, a Fourier transform, FT, must be used to observe the time response. The FT may be defined in many different conventions, the author will be using

$$F(\omega) = \int_{-\infty}^{+\infty} f(t)e^{j\omega t}\, dt \tag{5}$$

for the forward transform, and

$$f(t) = \frac{1}{2\pi} \int_{-\infty}^{+\infty} F(\omega)\, e^{-j\omega t}\, d\omega \tag{6}$$

17

for the inverse transform. Note that for any practical implementation, a discrete Fourier transform would be used and the data should be sampled adequately, as stated in [6] and [7]. The FT cannot be directly applied to the data. One must note that a time domain response of a radar is a real signal, $r(t)$. Because the response is real, its Fourier transform has the property

$$r(-\omega) = r^*(\omega), \tag{7}$$

where * represents the complex conjugate. Also, the data are a bandpassed signal; so, one should essentially zero pad the frequencies that are not measured. By zero-padding the data, Gibb's phenomena will be present in the time domain. Harris, in [13], recommends a Kaiser-Bessel filter with an α value of 2.0 to provide the best suppression. In summary, the time domain response may be found by

$$r(t) = \frac{1}{2\pi} \int_0^{+\infty} r(\omega) e^{-j\omega t} d\omega + \frac{1}{2\pi} \int_0^{+\infty} r^*(\omega) e^{j\omega t} d\omega. \tag{8}$$

If the background subtraction does not work well outside the calibration target range, for the calibration measurements, then a time gate, $G(t)$, may be performed on $C^c(\omega) - C^b(\omega)$. $G(t)$ should be chosen to contain all of the calibration target energy. This time gate can be performed, if the radar system decays rapidly enough so that none of the calibration target energy is smeared outside of the time gate. Under these conditions, Equation (4) becomes

$$M^c(\omega) = G(\omega) * \left(C^c(\omega) - C^b(\omega) \right) \tag{9}$$

The RCS, $\Gamma(\omega)$, may be then found by deconvolving the system response as mentioned earlier. By combining (1), (2), (4), and (3) then

$$\Gamma(\omega) = \frac{T^t(\omega) - T^b(\omega)}{C^c(\omega) - C^b(\omega)} \Gamma_e(\omega) \tag{10}$$

If a time gate of the calibration target is used, Equations (1), (2), (4) and (9) result in

$$\Gamma(\omega) = \frac{T^t(\omega) - T^b(\omega)}{G(\omega) * \left(C^c(\omega) - C^b(\omega) \right)} \tag{11}$$

18

Equation (10) may be used when the background subtraction works well by itself, whereas Equation (11) is used with the time gating. The main advantage of Equation (10) over (11) is that it has more useful bandwidth. The time gating done in Equation (11) reduces the useful bandwidth because of the convolution done by the time gate.

Now that the groundwork has been laid on the techniques for acquiring measured data, a discussion of the imaging techniques is given in the next chapter.

SECTION 3

Imaging Techniques

Identification of scattering mechanisms from the RCS measurements can sometimes be difficult, especially for complex targets. By imaging the data, one may gain some insight. In addition, imaging reduces the necessity of taking an in depth look at all of the data, individually. The image provides a means of examining trends in the entire data set at the same time. This chapter will describe several methods of presenting the data. Waterfall plots will be discussed in Section 3.1. In order to produce images, several assumptions need to be made. These assumptions are discussed in Section 3.2. Imaging algorithms are dependent upon the different measurement geometries. These algorithms are presented in Sections 3.3–3.5 for different polar geometries and Section 3.6 for linear SAR geometry. In addition to the algorithms presented for the particular geometries, these sections also describe measurement requirements such as sampling and crossrange resolution. Then, the computer program implementation of some of these algorithms are discussed in Section 3.7.

3.1   Waterfall Plots

One of the simplest imaging techniques is to produce a waterfall plot of the data. The waterfall plots provide information on target behavior over given experimental changes. One, commonly used waterfall plot, is target behavior over measurement
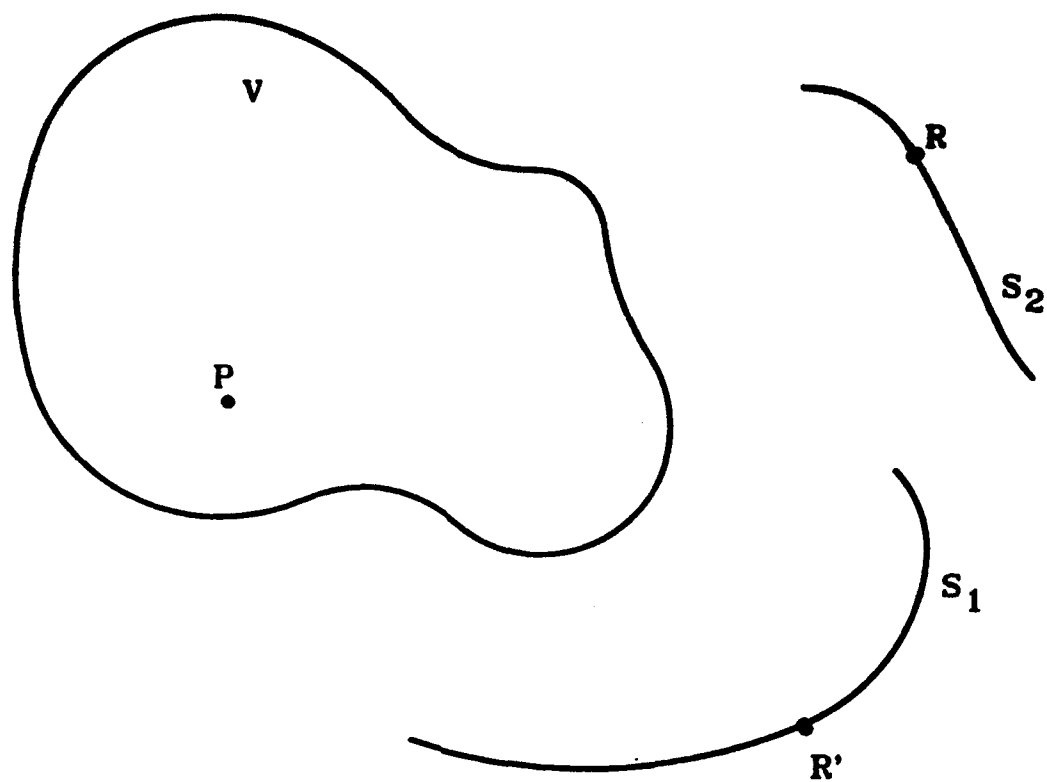
Figure 14: Geometry of an Inverse Scattering Problem

samples. This allows a person to make an easier comparison of target behavior, see Chapter 5.

3.2 Imaging Assumptions

Although the waterfall plots are informative, the plots do not have any processing gain. Other imaging techniques provide processing gain. However, several assumptions are needed before any imaging techniques are used.

Imaging may be thought of as a special case of the inverse scattering problem. The inverse scattering problem may be stated as follows. The geometric structure or contour of an unknown object, as seen in Figure 14, is desired. Let the object be

located in a volume of space, V. The material parameters, such as conductivity, of the objects inside V are assumed to be different so that the object may be identified from its surroundings. A known excitation source, located at $\overline{R'}$ on surface S_1, produces a known incident field, Φ_i. The surface S_1 may be an open or closed surface. Φ_i strikes an object in V which causes a scattered field, Φ_s. Φ_s is known from measurements on a surface S_2, which may be an open or closed surface, at a point $\overline{R}$. The inverse scattering problem is not unique and usually cannot be solved exactly. Most of the current inverse scattering problems are solved after making several assumptions.

In generating the solution of the inverse scattering problem, several assumptions must be made. The first assumption is that the direct scattering is the only scattering mechanism. The second is that the propagation velocity remains constant. Another assumption is that the scattering centers cannot be shadowed, so that the scattering centers behave like isotropic point scatters. In addition, the scattering must come only from the the target region. Also, the scattered field is assumed to be colinear with the incident field. Under these conditions, Langenberg has shown in [8], that the inverse problem can be solved.

These assumptions allow the scattered field at a field point, $\vec{r}$, from a source point, $\vec{P}$, to be written for the volume V in free space as [8]

$$\Phi_s(\vec{r}) = \int \int \int_V g(\vec{P})\Phi_i(\vec{P})G_o \, d\vec{P} \tag{12}$$

where G_o is the free space Green's function and where $g(\vec{r})$ represents the two dimensional scattering center distribution in two dimensions. Mensa, in [9], has termed this the *reflectivity density function*. From this equation, the calibrated radar response, Γ, may be found in the time domain by the following equation:

$$\Gamma(t) = \int \int \int_V g(\vec{P})\delta(2\vec{k}_s \cdot \vec{r} - t)d\vec{P} \tag{13}$$

where $\vec{k}_s$ represents the wavenumber. Since monostatic radar measurements are used throughout the rest of this report, an effective wavenumber, $\vec{k}$, will be defined as $\vec{k} = 2\vec{k}_s$.

22
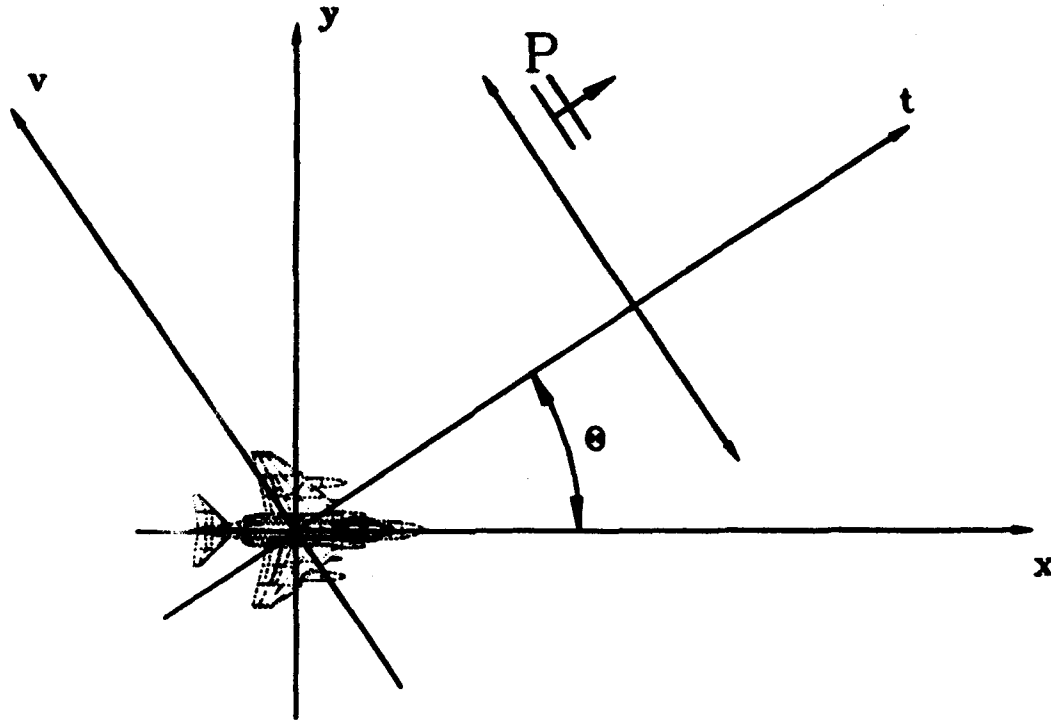
Figure 15: Measurement Geometry

3.3 Two-Dimensional Fourier Method

Methods for determining the two dimensional scattering center distribution is dependent upon the measurement geometry. In the particular case of polarimetric ISAR (Inverse Synthetic Aperture Radar) imaging, the measurement geometry is shown in Figure 15, where the center of rotation of the target is located at the origin. The coordinate system shown is the target coordinate system. In the target coordinate system, the target remains stationary, so that when the support column rotates, the antenna moves while the target remains still. The target is illuminated by a plane wave, P at an incident angle θ. Note that the plane wave travels in the positive t-axis direction in the t-v coordinate system. The assumptions made in Section 3.2

23

allow one to write the radar impulse response as follows [9]:

$$\Gamma(t, \theta) = \int_{-\infty}^{+\infty} g_t(t, v) dv \tag{14}$$

where $g_t(t, v)$ is $g(x, y)$ in the t-v coordinate system.

One interpretation of (14) is as follows. As the plane wave travels, a portion of the wave is reflected at each point. The reflected contributions, from each point, form a wave which is reflected back to the antenna. The antenna sums up all the energy from the incoming wave.

The Fourier transform, of Equation (14), results in

$$\Gamma(\omega, \theta) = \int_{-\infty}^{+\infty} \int_{-\infty}^{+\infty} g_t(t, v) e^{j\omega t} dv \ dt. \tag{15}$$

Writing $g_t(t, v)$ in terms of the x-y coordinate system uses a coordinate transformation of

$$x = t \ \cos(\theta) - v \ \sin(\theta) \tag{16}$$

$$y = t \ \sin(\theta) + v \ \cos(\theta). \tag{17}$$

Equation (15) becomes

$$\Gamma(\omega, \theta) = \int_{-\infty}^{+\infty} \int_{-\infty}^{+\infty} g(t \ \cos \ \theta \ - v \ \sin \ \theta, t \ \sin \ \theta \ + v \ \cos \ \theta) e^{j\omega t} dv \ dt. \tag{18}$$

A change of the integration variables in (18) to the $x - y$ coordinate system is done by a simple coordinate rotation given

$$t = x \ \cos(\theta) + y \ \sin(\theta), \tag{19}$$

$$v = -x \ \sin(\theta) + y \ \cos(\theta). \tag{20}$$

The change of variables results in

$$\Gamma(\omega, \theta) = \int_{-\infty}^{+\infty} \int_{-\infty}^{+\infty} g(x, y) e^{j\omega(x \ \cos \ \theta + y \ \sin \ \theta)} dx \ dy. \tag{21}$$

24

Now consider the two-dimensional Fourier transform in the $x - y$ coordinate system of the reflectivity density function given by

$$G(k_x, k_y) = \int_{-\infty}^{+\infty} \int_{-\infty}^{+\infty} g(x, y) e^{j(k_x x + k_y y)} dx\, dy. \tag{22}$$

Comparing (21) and (22), one can see that the two equations are equal, where

$$k_x = \omega \cos \theta \tag{23}$$

$$k_y = \omega \sin \theta. \tag{24}$$

Equations (21) and (22) allow one to easily determine $G(k_x, k_y)$ from

$$G(k_x, k_y) = G(\omega \cos \theta, \omega \sin \theta) = \Gamma(\omega, \theta). \tag{25}$$

This result is known as the Fourier Slice theorem. Equation (25) allows one to determine $g(x, y)$.

The equation allows one to determine spectrum $G(k_x, k_y)$ from the measured data. $G(k_x, k_y)$ may be determined easily by interpolating the values of $\Gamma(\omega, \theta)$. Once $G(k_x, k_y)$ has been determined, $g(x, y)$ may be easily determined by a two-dimensional inverse fourier transform such as (26)

$$g(x, y) = \frac{1}{4\pi^2} \int_{-\infty}^{+\infty} \int_{-\infty}^{+\infty} G(k_x, k_y) e^{-j(k_x x + k_y y)} dk_x\, dk_y. \tag{26}$$

In practice, one cannot obtain all the data required to implement (25). Instead, one must sample enough data to accurately approximate $g(x, y)$. If equally spaced samples are used to implement (25) or (35), (39) must satisfy the Nyquist criterion. If the object is space limited, has a maximum distance, L, from the axis of rotation, and the data are bandlimited with a maximum frequency, f_{max}, then the sampling required for (39) is

$$\Delta f < \frac{c}{2L}. \tag{27}$$

Now consider when the object rotates at an angle, $\Delta\theta$, the point at L moves a distance in the direction of the propagating wave, $\Delta d \approx L \sin \Delta\theta$. The two way
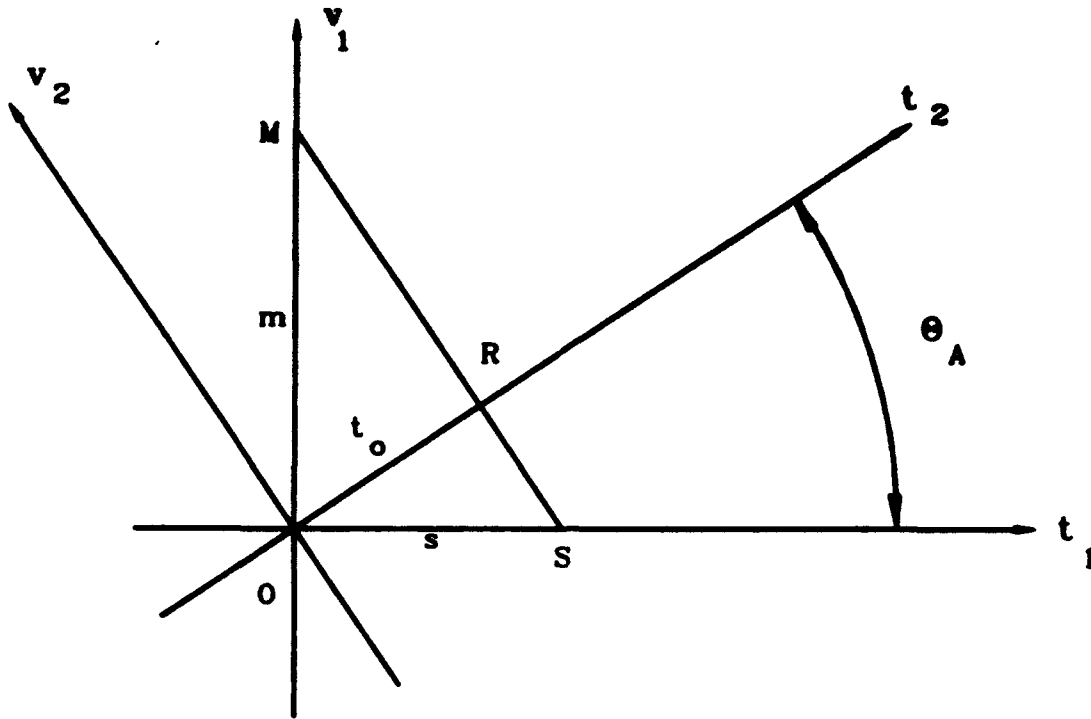
Figure 16: Crossrange Resolution Calculation Geometry

path length in time for Δd is $\Delta t = 2 \frac{\Delta d}{c}$. To satisfy the Nyquist criterion, $f_{max} < \frac{1}{\Delta t}$ or $f_{max} < \frac{c}{2L \sin \Delta \theta}$. Rearranging, it becomes

$$\sin \Delta \theta < \frac{c}{2L f_{max}}. \tag{28}$$

Usually, the approximation of $\Delta \theta \approx \sin \Delta \theta$ is used in (28) to give

$$\Delta \theta < \frac{c}{2L f_{max}}. \tag{29}$$

An image will sometimes be generated with a limited number of angular samples. If this limited sampling is done, the image will have a limited crossrange resolution. One can calculate the crossrange resolution by considering the resolution from scans separated by an angle of Θ_A. In Figure 16, angular measurements are represented for plane waves traveling along the t_1 and t_2 axes of coordinate frames $t_1 - v_1$ and $t_2 - v_2$, respectively. If the point M located on the v_1 axis is the minimum crossrange distance

that needs to be resolved with the origin, the point M will be seen in measurement t_2 at time t_m. An object at S also contributes to the response of t_m. The object at S on the t_1 axis produces a response at time t_s in measurement t_1. Since S cannot be resolved in measurement t_1, then $s < \frac{\lambda_{min}}{2}$ or equivalently, $s < \frac{c}{2f_{max}}$. From the geometry, $s = m \tan \Theta_a$, so

$$m = \frac{c}{2 \, f_{max} \, \tan \Theta_A} \tag{30}$$

Usually, crossrange resolution is measured from the center of the look angles. If ϕ is the measured angle range, the crossrange resolution, C_r becomes

$$C_r = \frac{c}{2 \, f_{max} \, \tan \frac{\phi}{2}} \tag{31}$$

because of symmetry. Equation (31) is essentially valid for $\phi < 90°$. For $\phi > 90°$, $C_r = \frac{c}{2 \, f_{max}}$.

3.4 Two-Dimensional Convolution Backprojection Method

As seen in the last section, the Fourier Slice theorem may be used to generate an image. Implementation of Fourier imaging may be done in another manner which will be described in this section. Equation (26) may be rewritten in polar coordinates as

$$g(x,y) = \frac{1}{4\pi^2} \int_0^{2\pi} \int_0^{+\infty} \omega \, G(\omega \cos \theta, \omega \sin \theta) e^{-j\omega(x \cos \theta + y \sin \theta)} \, d\omega \, d\theta. \tag{32}$$

Note that $G(k_x, k_y)$ has the following property:

$$G(\omega \cos (\theta + \pi), \omega \sin (\theta + \pi))) = G(-\omega \cos \theta, -\omega \sin \theta). \tag{33}$$

Making use of the trigonometric identities $\cos(\theta + \pi) = -\cos \theta$ and $\sin(\theta + \pi) = -\sin \theta$, Equation (32) may be manipulated with (33) to yield

$$g(x,y) = \frac{1}{4\pi^2} \int_0^{\pi} \int_{-\infty}^{+\infty} |\omega| \, G(\omega \cos \theta, \omega \sin \theta) e^{-j\omega(x \cos \theta + y \sin \theta)} \, d\omega \, d\theta. \tag{34}$$

27

Note in (34) that only 180 degrees of data are needed to characterize g(x,y). This fact is true because of the assumption that scattering centers cannot be shadowed.

Substituting (25) and (19) into (34) results in

$$g(x,y) = \frac{1}{4\pi^2} \int_0^\pi \int_{-\infty}^{+\infty} |\omega| \; \Gamma(\omega,\theta)e^{-j\omega t} \; d\omega \; d\theta, \tag{35}$$

where

$$t = x\cos\theta + y\sin\theta. \tag{36}$$

Equation (35) is known as the convolution backprojection theorem. The inner integral may be rewritten as a convolution.

$$g(x,y) = \frac{1}{2\pi} \int_0^\pi \Gamma(t,\theta) \; * \; \Omega(t) \; d\theta \tag{37}$$

where

$$\Omega(t) = \frac{1}{2\pi} \int_{-\infty}^{+\infty} |\omega| \; e^{-j\omega t} \; d\omega \tag{38}$$

and

$$\Gamma(t,\theta) = \frac{1}{2\pi} \int_{-\infty}^{+\infty} \Gamma(\omega,\theta)e^{-j\omega t} \; d\omega. \tag{39}$$

3.5 Three-Dimensional Imaging on a Plane

Implementation of the three-dimensional Fourier imaging techniques is not practical on present computer systems because of computer storage space. A low-resolution 128x128x128 pixel image uses approximately 8 megabytes of storage. Although there are many computer systems that have large amounts of memory and can generate the high-resolution 3-D images, one must consider whether generating the whole 3-D image is worth the effort. Instead, one may construct several 2-D images that are cuts of the three-dimensional image. First, a three-dimensional imaging algorithm is derived. The algorithm is then written in a convolution backprojection form. From the convolution backprojection equation, the 3-D imaging may be done easily.
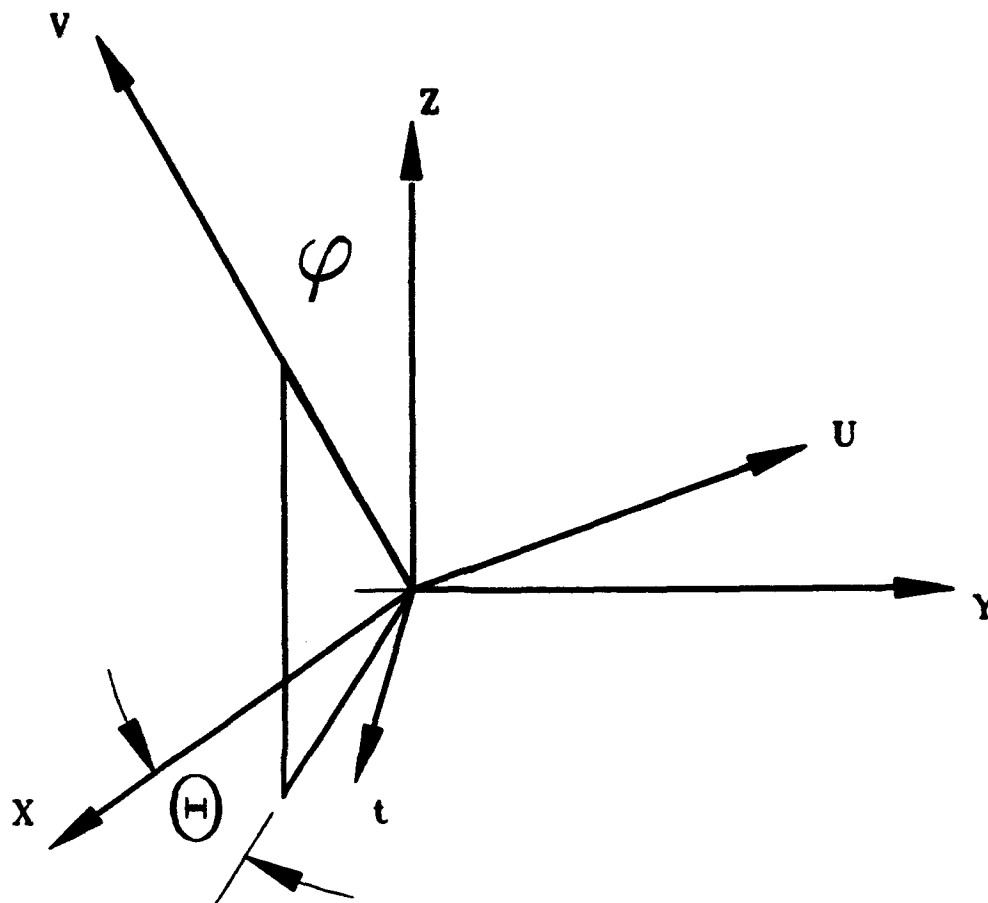
Figure 17: The Three-Dimensional Coordinate System Geometry

3.5.1 Three-Dimensional Fourier Imaging

The derivation of the three dimensional imaging technique parallels the two-dimensional case. The geometry of the problem is shown in Figure 17. In this three dimensional problem, a vector notation is used for convenience. The author will be using $\vec{r} = \begin{bmatrix} x & y & z \end{bmatrix}^T$ and $\vec{p} = \begin{bmatrix} t & u & v \end{bmatrix}^T$, where the ^{T} represents the transpose.

Once again, the assumptions made in Section 3.2 allow a function $g(x, y, z)$ to be defined representing the three-dimensional scattering center distribution. In the

t-u-v coordinate system, the calibrated radar response may be written as

$$\Gamma(t, \theta\phi) = \int_{-\infty}^{+\infty} \int_{-\infty}^{+\infty} g_t(t, u, v) \, du \, dv, \qquad (40)$$

where $g_t(t, u, v)$ is $g(x, y, z)$ in the t-u-v coordinate system.

From Figure 17, one can find the coordinate transformations to change between coordinate systems. The coordinate transform from $\vec{r}$ to $\vec{p}$ is related by a rotation in the $x - y$ plane followed by rotation in the $x - z$ plane. The result given as

$$\begin{bmatrix} t \\ u \\ v \end{bmatrix} = \begin{bmatrix} \cos\phi\sin\theta & \sin\phi\sin\theta & \cos\theta \\ -\sin\phi & \cos\phi & 0 \\ -\cos\phi\cos\theta & -\sin\phi\cos\theta & \sin\theta \end{bmatrix} \begin{bmatrix} x \\ y \\ z \end{bmatrix} \qquad (41)$$

In vector notation, (41) is written as $\vec{p} = T\vec{r}$, where T is the transformation matrix.

The inverse transform of (41) may be found by premultiplying both sides of (41) by the inverse of T. The matrix multiplication results in $\vec{r} = T^{-1}\vec{p}$ or equivalently Equation (42).

$$\begin{bmatrix} x \\ y \\ z \end{bmatrix} = \begin{bmatrix} \cos\phi\sin\theta & -\sin\phi & -\cos\phi\cos\theta \\ \sin\phi\sin\theta & \cos\phi & -\sin\phi\cos\theta \\ \cos\theta & 0 & \sin\theta \end{bmatrix} \begin{bmatrix} t \\ u \\ v \end{bmatrix} \qquad (42)$$

The function, $g_t(t, u, v)$, may now be written in $x - y - z$ coordinate system. Substituting (41) into (40) results in

$$\Gamma(t, \theta, \phi) = \int_{-\infty}^{+\infty} \int_{-\infty}^{+\infty} g(T^{-1}\vec{p}) \, du \, dv. \qquad (43)$$

The Fourier transform of (43) results in

$$\Gamma(\omega, \theta, \phi) = \int_{-\infty}^{+\infty} \int_{-\infty}^{+\infty} \int_{-\infty}^{+\infty} g(T^{-1}\vec{p}) e^{j\omega t} \, du \, dv \, dt \qquad (44)$$

A change, of integration variables in (44) using (42), yields

$$\Gamma(\omega, \theta, \phi) = \int_{-\infty}^{+\infty} \int_{-\infty}^{+\infty} \int_{-\infty}^{+\infty} g(T^{-1} \, T\vec{r}) e^{j\omega \, (\cos\phi\sin\theta + \sin\phi\sin\theta + \cos\theta)} \, dx \, dy \, dz. \qquad (45)$$

30

Making note of the fact that $T^{-1} T = I$, where I is the identity matrix, and writing (45) in scalar notation, results in

$$\Gamma(\omega, \theta, \phi) = \int_{-\infty}^{+\infty} \int_{-\infty}^{+\infty} \int_{-\infty}^{+\infty} g(x, y, z) e^{j\omega \ (\cos\phi\sin\theta + \sin\phi\sin\theta + \cos\theta)} \ dx \ dy \ dz. \quad (46)$$

The three-dimensional Fourier transform of $g(x, y, z)$ is given by

$$G(k_x, k_y, k_z) = \int_{-\infty}^{+\infty} \int_{-\infty}^{+\infty} \int_{-\infty}^{+\infty} g(x, y, z) e^{j \ (k_x x + k_y y + k_z z)} \ dx \ dy \ dz. \quad (47)$$

One notes that (46) and (47) are equal when

$$k_x = \omega \ \cos\phi\sin\theta \quad (48)$$

$$k_y = \omega \ \sin\phi\sin\theta \quad (49)$$

$$k_z = \omega \ \cos\theta. \quad (50)$$

Equations (46), (47), (48), (49), and (50) allows one to easily determine $G(k_x, k_y, k_z)$ from

$$G(k_x, k_y, k_z) = G(\omega \ \cos\phi\sin\theta, \omega \ \sin\phi\sin\theta, \omega \ \cos\theta) = \Gamma(\omega, \phi, \theta) \quad (51)$$

Equation (51) is the Fourier Slice theorem in three dimensions and can be used to reconstruct $G(k_x, k_y, k_z)$. From $G(k_x, k_y, k_z)$, one may determine $g(x, y, z)$ by the inverse three dimensional Fourier transform given by

$$g(x, y, z) = \frac{1}{8\pi^3} \int_{-\infty}^{+\infty} \int_{-\infty}^{+\infty} \int_{-\infty}^{+\infty} G(k_x, k_y, k_z) e^{-j \ (k_x x + k_y y + k_z z)} \ dx \ dy \ dz. \quad (52)$$

3.5.2 Three-Dimensional Convolution Backprojection

The 3-D Fourier Slice theorem may now be written in a convolution backprojection form. The right hand side of (52) may be written in polar coordinates as

$$g(x, y, z) = \frac{1}{8\pi^3} \int_0^{\pi} \int_0^{2\pi} \int_0^{+\infty} \omega^2 \ G(\omega \cos\phi\sin\theta, \omega \sin\phi\sin\theta, \omega \cos\theta)$$
$$e^{-j \ \omega(x\cos\phi\sin\theta + y\sin\phi\sin\theta + z\cos\theta)} \sin\theta \ d\omega \ d\phi \ d\theta. \quad (53)$$

31

By using the property,

$$G(\omega \cos \phi \sin \theta, \omega \sin \phi \sin \theta, \omega \cos \theta) =$$

$$G(-\omega \cos(\phi + \pi) \sin \theta, -\omega \sin(\phi + \pi) \sin \theta, -\omega \cos \theta), \tag{54}$$

and the trigonometric identities, $\cos(\phi + \pi) = -\cos\phi$ and $\sin(\phi + \pi) = -\sin\phi$, Equation (53) may be transformed to

$$g(x, y, z) = \frac{1}{8\pi^3} \int_0^\pi \int_0^\pi \int_{-\infty}^{+\infty} \omega^2 \, G(\omega \cos \phi \sin \theta, \omega \sin \phi \sin \theta, \omega \cos \theta)$$

$$e^{-j \, \omega(x \cos \phi \sin \theta + y \sin \phi \sin \theta + z \cos \theta)} \sin \theta \, d\omega \, d\phi \, d\theta. \tag{55}$$

Using the Fourier Slice theorem and (55), one is able to derive the convolution backprojection technique

$$g(x, y, z) = \frac{1}{8\pi^3} \int_0^\pi \int_0^\pi \int_{-\infty}^{+\infty} \omega^2 \, \Gamma(\omega, \phi, \theta) e^{-j \, \omega \, t} \sin \theta \, d\omega \, d\phi \, d\theta \tag{56}$$

where

$$t = x \cos \phi \sin \theta + y \sin \phi \sin \theta + z \cos \theta \tag{57}$$

Equation (56) may be written in terms of a time domain convolution as

$$g(x, y, z) = \frac{1}{4\pi^2} \int_0^\pi \int_0^\pi \Gamma(t, \phi, \theta) * \Omega_3(t) \sin \theta \, d\phi \, d\theta \tag{58}$$

$$\Gamma(t, \phi, \theta) = \frac{1}{2\pi} \int_{-\infty}^{+\infty} \Gamma(\omega \, \phi, \theta) e^{-j \, \omega \, t} \, d\omega \tag{59}$$

$$\Omega_3(t) = \frac{1}{2\pi} \int_{-\infty}^{+\infty} \omega^2 \, e^{-j \, \omega \, t} \, d\omega \tag{60}$$

3.5.3 Imaging on a Plane

Equation (56) may be rewritten for a constant z and ϕ as

$$g(x, y, z) = \frac{1}{8\pi^3} \int_0^\pi \int_0^\pi \int_{-\infty}^{+\infty} \omega^2 \, \Gamma(\omega, \phi, \theta) e^{-j\omega t' \sin \theta} e^{-j\omega z \cos \theta} \sin \theta d\omega \, d\phi \, d\theta \tag{61}$$

where

$$t' = x \cos \phi + y \sin \phi \tag{62}$$

32

Recognizing that the $e^{-j\omega z\cos\theta}$ is a time delay in time domain and $\sin\theta$ in the exponential term is a time scaling factor, (61) written as a convolution is

$$g(x,y,z) = \frac{1}{4\pi^2} \int_0^\pi \int_0^\pi \Omega(t') * \Omega(t') * \Gamma_t(t'/\sin\theta - z\cos\theta, \phi, \theta)\, d\phi\, d\theta \quad (63)$$

where

$$\Gamma_t(t, \phi, \theta) = \frac{1}{2\pi} \int_{-\infty}^{+\infty} \Gamma(\omega\,\phi, \theta)e^{-j\,\omega\,t}\, d\omega \quad (64)$$

$$\Omega(t) = \frac{1}{2\pi} \int_{-\infty}^{+\infty} \omega\, e^{-j\,\omega\,t}\, d\omega \quad (65)$$

For a constant z, (63) is easily implemented. The equation may be interpreted as a process to determine $g(x,y,z)$ for a single z-plane for conical cuts in the data space. (63) looks similar to (37). The similarity allows one to easily implement (63) in an existing two-dimensional convolution-backprojection technique. The integral is a two-dimensional image generated with an additional convolution term, frequency scaling, and a phase shift.

In implementing (63), one must sample the data needed for the image. If one uses equally spaced angular increments, the results from Section 3.3 may be used in both angular directions, θ and ϕ.

$$\Delta\theta < \frac{c}{2Lf_{max}}. \quad (66)$$

$$\Delta\phi < \frac{c}{2Lf_{max}}. \quad (67)$$

Crossrange resolution may also be computed using the results from the two-dimensional case.

3.6   Near-Field Linear SAR

Although there are many different methods of deriving an algorithm for linear synthetic aperture radar imaging [8], [10], [11], the imaging techniques described in Section 3.4 may be adapted for the linear SAR geometry [11]. Due to the nature of near-field linear SAR, a generated image will inherently have nonuniform resolution

33

due to a finite aperture. Derivations of near-field linear SAR imaging techniques use different approximations, which are not always completely valid. Each imaging technique has its advantages and disadvantages. One of the major advantages for using the adapted convolution-backprojection algorithm, is that the algorithm is easily incorporated into an existing convolution-backprojection program. The derivation is accomplished in two steps. First, the two-dimensional convolution-backprojection will be modified to compensate for wavefront curvature. Then, the algorithm will be adapted for a linear SAR geometry. Sampling and crossrange resolution for linear SAR is then presented.

3.6.1   Near-Field Imaging

For imaging in the near-field, the geometry of the coordinate system is shown in Figure 18. As seen in the figure, the radar is located at a point $R_p(\rho, \Theta)$. Since the radar is in the near field, the radar emits spherical waves. The radar return at time (or distance), ρ, in essence, measures the reflectivity in a spherical shell. Since the image is done on the slant plane, the radar echo returns the ground reflectivity in a circular projection. This circular projection is illustrated as an arc labeled A in Figure 18. In a typical application, the arc is limited by the beamwidth of the antenna.

The radar echo is no longer a straight line projection. Instead, the projection now lies in an arc of radius, ρ. The calibrated radar signal can now be represented as [11]

$$\Gamma(\rho, R_p) = \int_A g(R\cos\Theta - \rho\cos\phi, R\sin\Theta - \rho\sin\phi)d\Theta, \tag{68}$$

where R_p is the radar location and g is the radar reflectivity function in the $x - y$ coordinate system.

The circular arcs of Equation (68) may be converted as an equivalent straight line projection [11]. This conversion may be done by first rotating the $x - y$ plane at an angle Θ . The transformation to the $t - v$ coordinate system can be accomplished

34

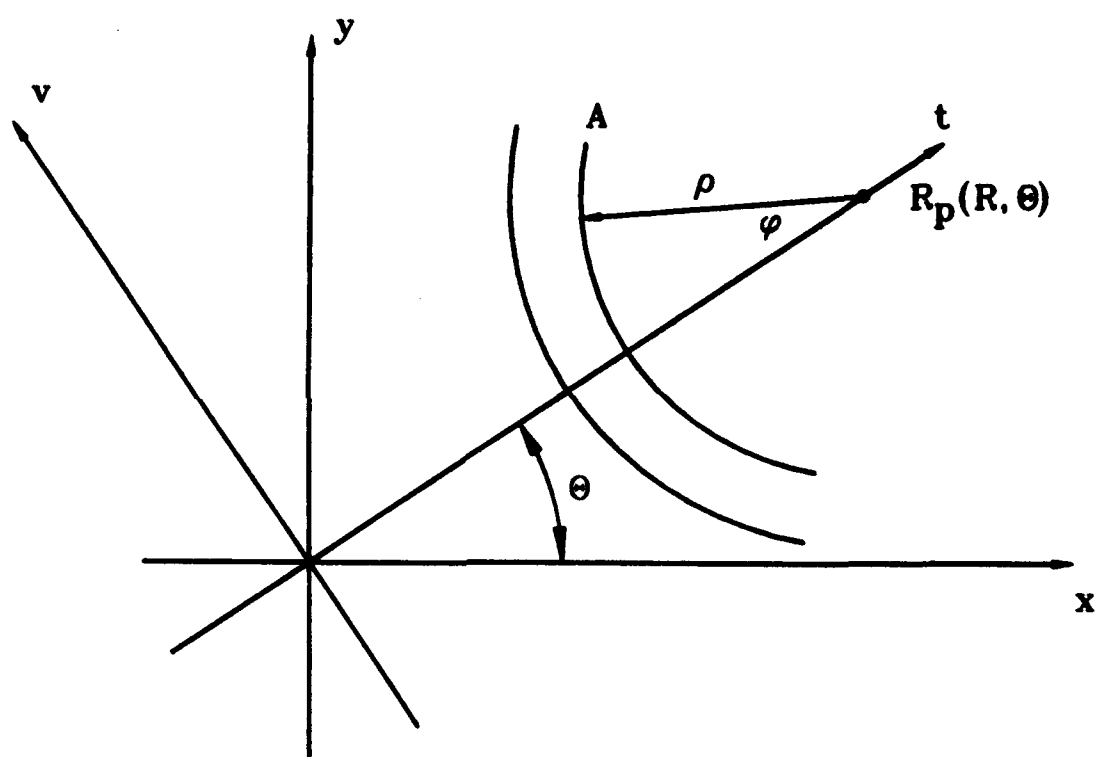Figure 18: Near-Field Imaging Geometry

by using

$$t = x \cdot \cos(\Theta) + y \cdot \sin(\Theta) \tag{69}$$

$$v = -x \cdot \sin(\Theta) + y \cdot \cos(\Theta) \tag{70}$$

The circular arcs may then be "straightened" by transforming to the $t'-v'$ coordinate system given by

$$t' = R - \rho \tag{71}$$

$$v' = \rho\phi, \tag{72}$$

where

$$\rho = \sqrt{(R-t)^2 + v^2} \tag{73}$$

$$\phi = \arcsin \frac{v}{\rho} \tag{74}$$

The straightened projection may then be used to reconstruct $g(x,y)$ by using the standard convolution backprojection algorithm,

$$g(x,y) = \frac{1}{2\pi} \int_0^\pi \Gamma(t',\Theta) \ast \Omega(t) \, d\Theta \tag{75}$$

where $\Gamma(t',\Theta)$ and $\Omega(t')$ are given by (37). Equation (75) is naturally applied in a polar geometry.

3.6.2 Linear SAR

Near-field imaging can be be modified for linear SAR geometry. In the linear SAR geometry shown in Figure 19, measurements are made at points x_i along the x-axis. At each point $P(x,y)$, the radar echo angle of arrival, Θ, is given by

$$\Theta = \arctan \frac{y}{x - x_i} \tag{76}$$

The radar echo that measures the reflectivity at $P(x,y)$ travels a total time (or distance), t', given by,

$$t' = \sqrt{(x - x_i)^2 + y^2} \tag{77}$$

36
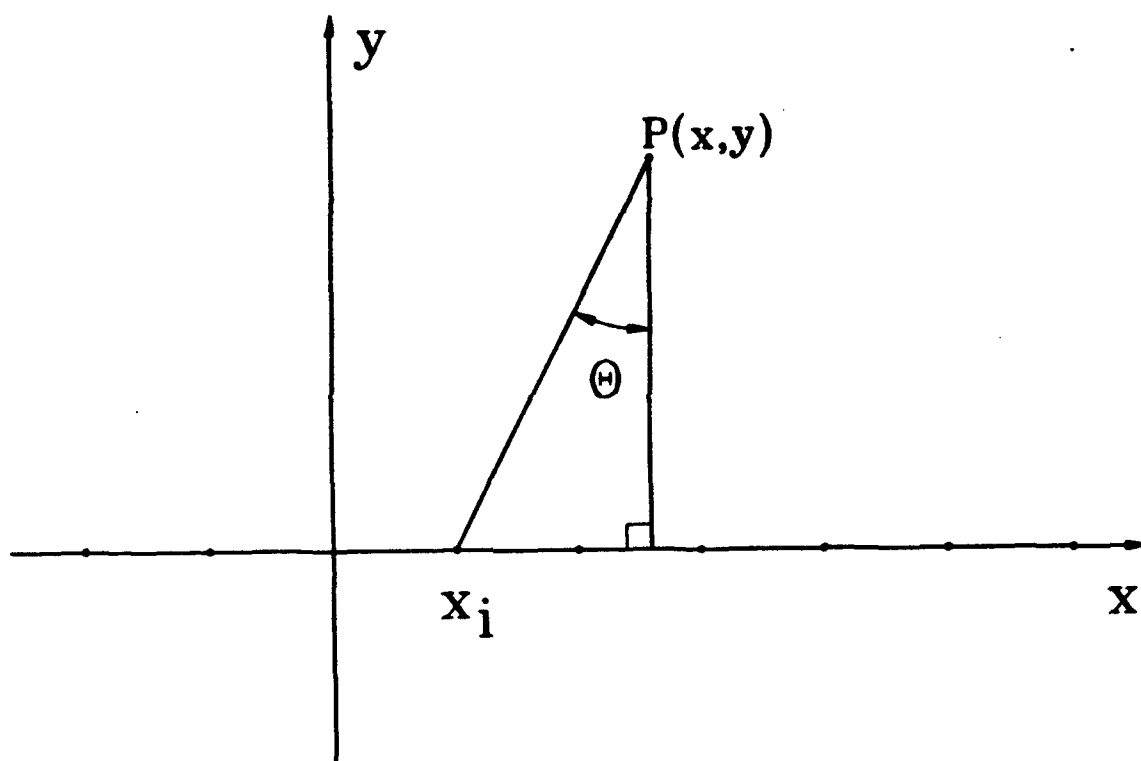
Figure 19: Linear SAR Geometry
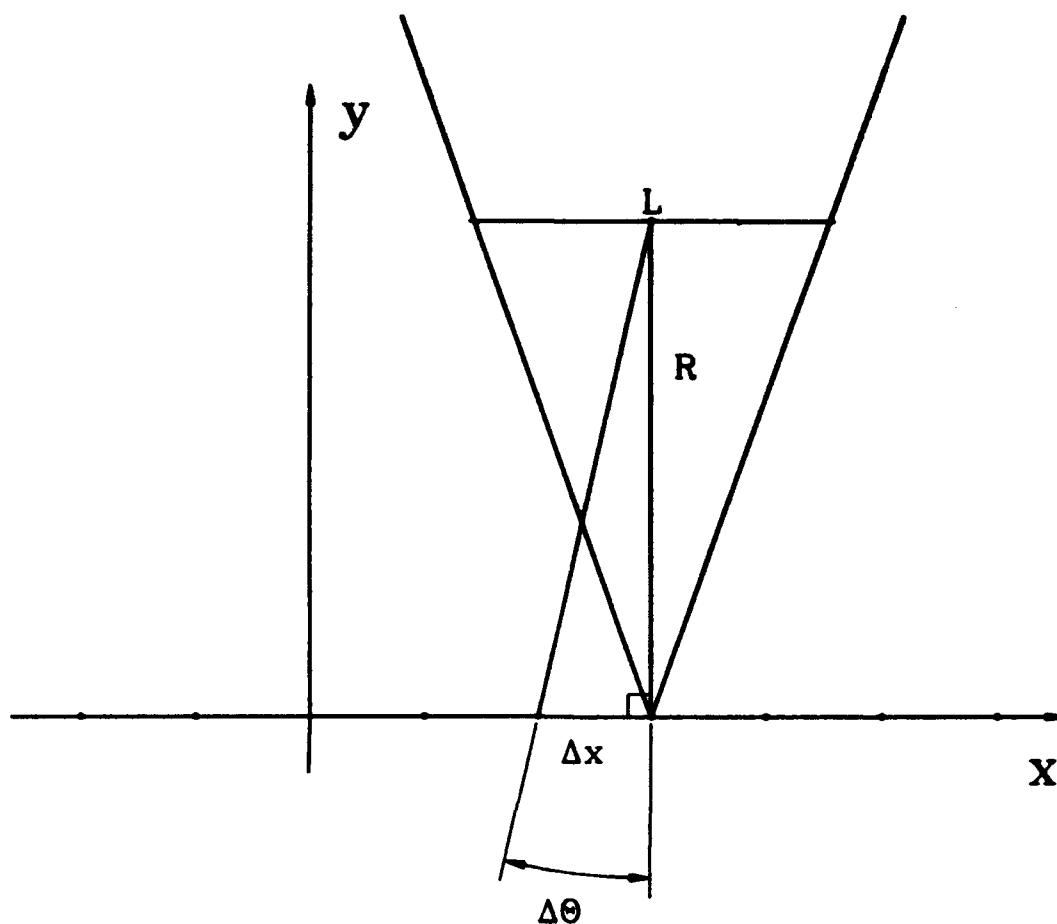
Figure 20: SAR Sampling Geometry

By a change of variables using (76), the modified backprojection becomes

$$g(x,y) = \int_{-\infty}^{+\infty} (\Gamma(t', x_i) * \Omega(t')) \frac{y}{x_i^2 + y^2} dx_i \qquad (78)$$

3.6.3 Measurement Requirements

One must consider the sampling requirements of (78). For a SAR system with an antenna beamwidth of ϕ as shown in Figure 20, Equation (28) may still be used to calculate the sampling requirements of (78). L still represents the largest resolvable object and is found from the antenna beamwidth by

$$L = 2 R_f \sin \frac{\phi}{2} \qquad (79)$$

38

The angular sampling, $\Delta\theta$, is related to the sample spacing, Δx by,

$$\Delta x = R_f \ \sin(\Delta\theta) \tag{80}$$

Combining Equations (28), (79), and (80), the sampling requirement, Δx is found by

$$\Delta x < \frac{c}{4 \ f_{max} \sin\frac{\phi}{2}} \tag{81}$$

Equation (31) may still be used to calculate the crossrange resolution for a finite aperture. As seen in Equations (31) and (78), if the scanning aperture is finite, then the resulting image will have nonuniform resolution. For a point on the perpendicular bisector of an aperture with length L at distance R (from the aperture), the point has an angular aperture of approximately $2 \ \tan^{-1}\frac{L}{2R}$. This equation along with Equation (31) gives the crossrange resolution of the aperture, C_r, as

$$C_r = \frac{cR}{f_{max}L} \tag{82}$$

for $R > \frac{L}{2}$.

3.7   Computer Program Implementation

Several of the algorithms in this chapter were implemented in a computer program. Chapter 5 shows that the images generated by the program are sensitive to the method used to implement the algorithm. This section describes the implementation of the algorithms in the computer program. The program can generate images based on Fourier Slice, convolution backprojection, three-dimensional imaging on a plane, and linear SAR.

In the implementation of the Fourier Slice method, one needs to interpolate polar samples to a rectangular raster. By recognizing that interpolation may be realized as a convolution of an interpolating function with a weighted delta functions located at the sample points, the interpolation may be easily done. For example, a one-dimensional function $y(x)$ is sampled at evenly spaced intervals, Δx. The resulting

sampled function, $y_o(x)$, is found to be

$$y_o(x) = comb(x, \Delta x)y(x),$$ (83)

where *comb* is a comb function given by

$$comb(x, \Delta x) = \sum_{n=-\infty}^{+\infty} \delta(x - n\Delta x).$$ (84)

From sampling theory, if $y(x)$ is a bandlimited signal and finite duration, $y(x)$ may be reconstructed from its samples by applying an ideal lowpass filter as given by

$$y(x) = \sum_{k=-\infty}^{+\infty} y_o(k\Delta x)sinc\left(\frac{x - k\Delta x}{\Delta x}\right)$$ (85)

Interpolation done in this manner with the sinc function is commonly referred to as bandlimited interpolation. The implementation of (85) is not practical, since the sum is extremely time consuming. Instead one usually substitutes a nonperfect interpolator, such as a zero-order hold, a first order hold (i.e. linear interpolation), or Lagrange interpolation, in place of the ideal low-pass filter. One should also note that Lagrange interpolation for an infinite order interpolation converges to the sinc function interpolation [12]. In summary, the interpolation may be done as follows:

$$G(k_x, k_y) = \sum_{n=0}^{N} \sum_{m=-M}^{M} \Gamma(2\pi\Delta f, n\Delta\theta)I_\theta(k_x, k_y, n\Delta\theta, \Delta\theta)I_f(k_x, k_y, 2\pi m\Delta f, \Delta f),$$ (86)

where I_θ is an interpolating function for angle, and I_f is an interpolating function for frequency. The computer program allows linear and n-th order sinc interpolation to be used for I_θ and I_f.

The resulting data plane for a single measured point, $\Gamma(\omega, \theta)$, is given by

$$G_m(k_x, k_y) = \Gamma(2\pi\Delta f, n\Delta\theta)I_\theta(k_x, k_y, \theta, \Delta\theta)I_f(k_x, k_y, \omega, \Delta f).$$ (87)

As seen in Equation (87), the entire $k_x - k_y$ plane needs to be interpolated for each point. Fortunately, the interpolating functions, I_θ and I_f, decay rapidly away from the sample point. As a result, the interpolation needs to be done only at points

40

near each sample point. The number of interpolated points (interpolation size) for each sample is implemented as a user defined variable in the computer program. A 5-point interpolation size centered at the measured sample point gives good results.

The image is generated by first adding up all the G_m, from all the sample points, to get $G(k_x, k_y)$. Once this is done, a simple two-dimensional fast Fourier Transform is performed on $G(k_x, k_y)$ to get $g(x, y)$, the resulting image. A lot of finesse is needed to implement the Fourier Slice theorem to provide the good results in Chapter 5.

Implementation of the other imaging techniques discussed are much simpler. Convolution backprojection is done as a brute force method of implementing Equation (35). If equally spaced angular samples are used, one may easily convert Equation (35) into a discrete sum. Using the same coordinate system as Equation (35), this conversion may be done by writing it as a Riemann sum approximation

$$g(x,y) = \sum_{n=1}^{N} \sum_{m=-M}^{M} \left[| \, m \, | \, (\Delta f)^2 \Gamma(2m\pi\Delta f, n\Delta\theta) \, e^{2\pi j m \Delta f t} \right] \Delta\theta \qquad (88)$$

where

$$t = x\cos(n\Delta\theta) + y\sin(n\Delta\theta), \qquad (89)$$

N is the number of frequency samples, Δf is the frequency sampling interval, M is the number of angular samples, and $\Delta\theta$ is the angular sampling interval. If t is now sampled at an interval of Δt, then the bracketed quantity in Equation (88) is a inverse discrete fast Fourier Transform of a filtered function, IDFFT. As a result, convolution backprojection is done in four steps. First, the measured data, $\Gamma(2m\pi\Delta f, n\Delta\theta)$, for each look angle is scaled and filtered by $| \, m \, | \, (\Delta f)^2$. Next, the IDFFT is appled to the filtered function to give

$$f_m(t_l) = \sum_{m=-M}^{M} | \, m \, | \, (\Delta f)^2 \Gamma(2m\pi\Delta f, n\Delta\theta) \, e^{2\pi j m l \Delta f \Delta t} \qquad (90)$$

The image for each look angle is found by backprojecting the data, look angle is

$$g_m(x,y) = f_m(t)\Delta\theta \qquad (91)$$

41

In backprojecting the data, interpolation is required to interpolate $f_m(t)$. To find the complete image, all the $g_m(x, y)$ are added together.

In the developed computer program, interpolation is done twice in the convolution backprojection. The first is done by the IDFFT. This interpolation is caused by zero padding the measured frequencies. By zero padding the data and performing an IDFFT, Fourier interpolation is done. Usually, zero padding by a factor of 4 is used. The other step in which interpolation is done is in backprojection. A cubic spline is used for the backprojection interpolation. The convolution backprojection is simpler to implement than Fourier Slice.

The three-dimensional imaging is even easier to implement. The imaging on a plane can be accomplished by preprocessing the measured data and using the standard convolution backprojection method. This preprocessing can be done first by a Shepp-Logan filter (multiply the frequency response by ω), then phase shifting the data by $z \cos\theta \sin\theta$, followed a frequency scaling by $sin\theta$. The data are then processed using convolution backprojection.

Although the linear SAR algorithm is based on a modified convolution backprojection technique, the linear SAR algorithm cannot be done by preprocessing the data. As a result, near field linear SAR imaging is also done as a brute force method of Equation (78). Using the same coordinate system as Equation (78), the approximations, $df \approx \Delta f$ and $dx_i \approx \Delta x_i$, are used to write the equation as a Riemann sum approximation,

$$ g(x, y) = \sum_{i=-\infty}^{+\infty} \sum_{m=-M}^{M} \left[|m| (\Delta f)^2 \Gamma(2m\pi\Delta f, x_i) e^{2\pi jm\Delta f t'} \right] \frac{y}{(x - x_i)^2 + y^2} \Delta x_i \quad (92) $$

where t' is given by

$$ t' = \sqrt{(x - x_i)^2 + y^2} \quad (93) $$

With the exception of one step, the linear SAR algorithm is the same as convolution backprojection algorithm, if t is replaced with t'. The only step of the algorithm

that is changed is the backprojection step. The backprojection is done by

$$g_m(x, y) = f_m(t') \frac{y}{(x - x_i)^2 + y^2} \Delta x_i \qquad (94)$$

Implementation of the algorithms into the computer program are easily done. Because the images generated from the computer program are Fourier based, the images have Gibb's phenomena. Because people often find it difficult to view waveforms with Gibb's phenomena, filtering, which is subject of the next chapter, is often used to suppress this phenomenon.

SECTION 4

Filtering

Data are normally filtered mainly because of two reasons. The first reason is to suppress noise, and the second is to allow a human to interpret the data more easily. Several useful filters will be discussed in this chapter.

4.1 Visual Filters

In the past, microwave imaging has viewed $| g(x,y) |$. This quantity is related to the scattered power from each point. Figure 21 shows an image of a 1/72 scale model of an F-4 fighter aircraft. More details of the image will be discussed in Chapter 5. In this chapter, this image will be used to illustrate the effects of filtering. There is information contained in the polarity of $g(x,y)$, so that the information should be preserved.

One important use of polarity pertains to how the human eye perceives color and shading. The eye performs an averaging over a spatial area, so gradual variations of shade usually cannot be easily discriminated. Sharp contrasting objects are prominent. Therefore, if one maps the polarity of g(x,y) to different colors, details that are not very noticeable in $| g(x,y) |$ will appear. Unfortunately, the use of color in this paper is not possible. Instead several clipping filters will be used to illustrate this point. These filters are listed in Table 1. These filters have been applied to the F-4 image. The resulting images are shown in Figures 22 to 24. Note that the
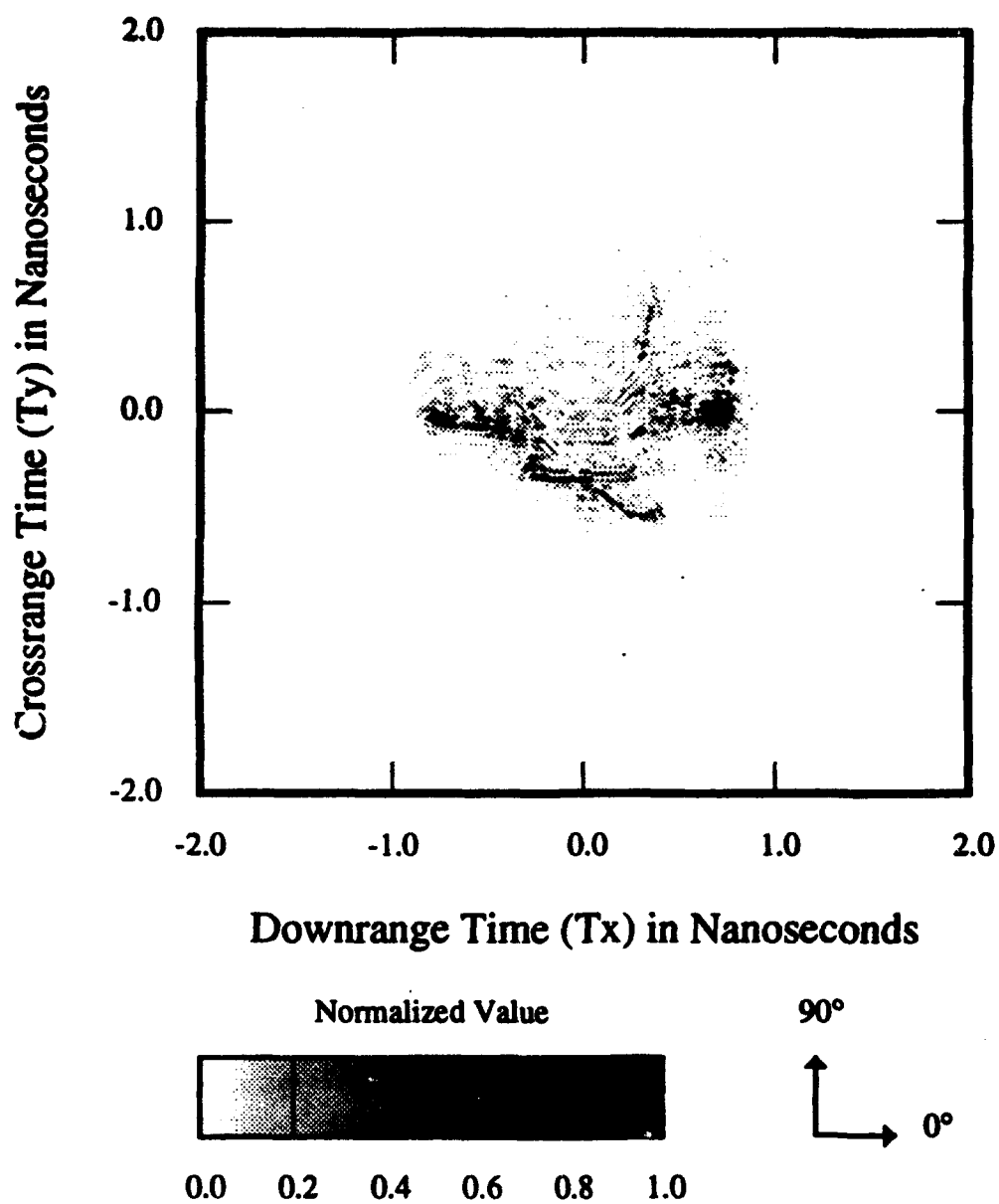
44

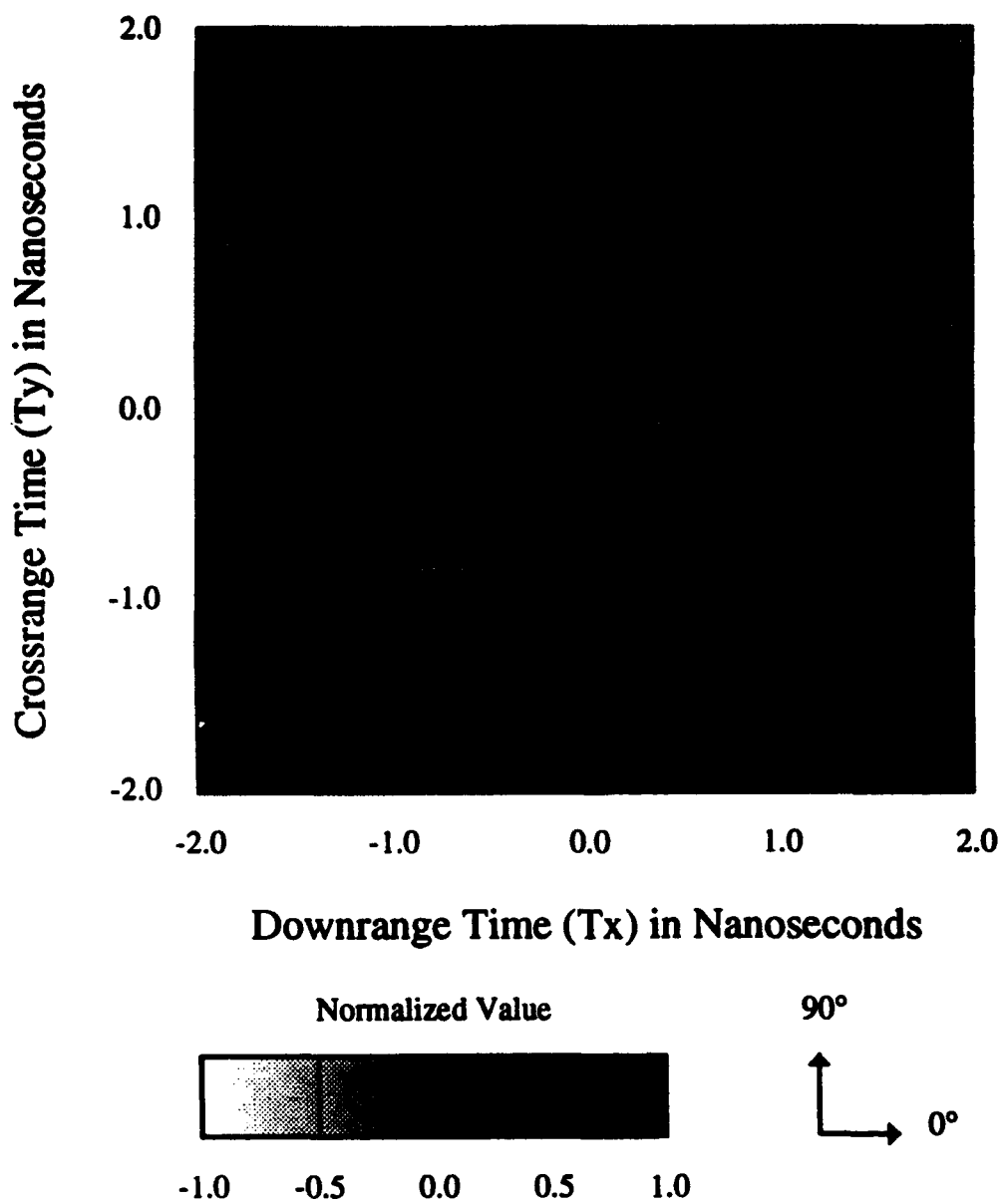Figure 21: F-4 Phantom Model. This plot shows $| g(x,y) |$.

2.0

1.0

Crossrange Time (Ty) in Nanoseconds

0.0

-1.0

-2.0

-2.0   -1.0   0.0   1.0   2.0

Downrange Time (Tx) in Nanoseconds

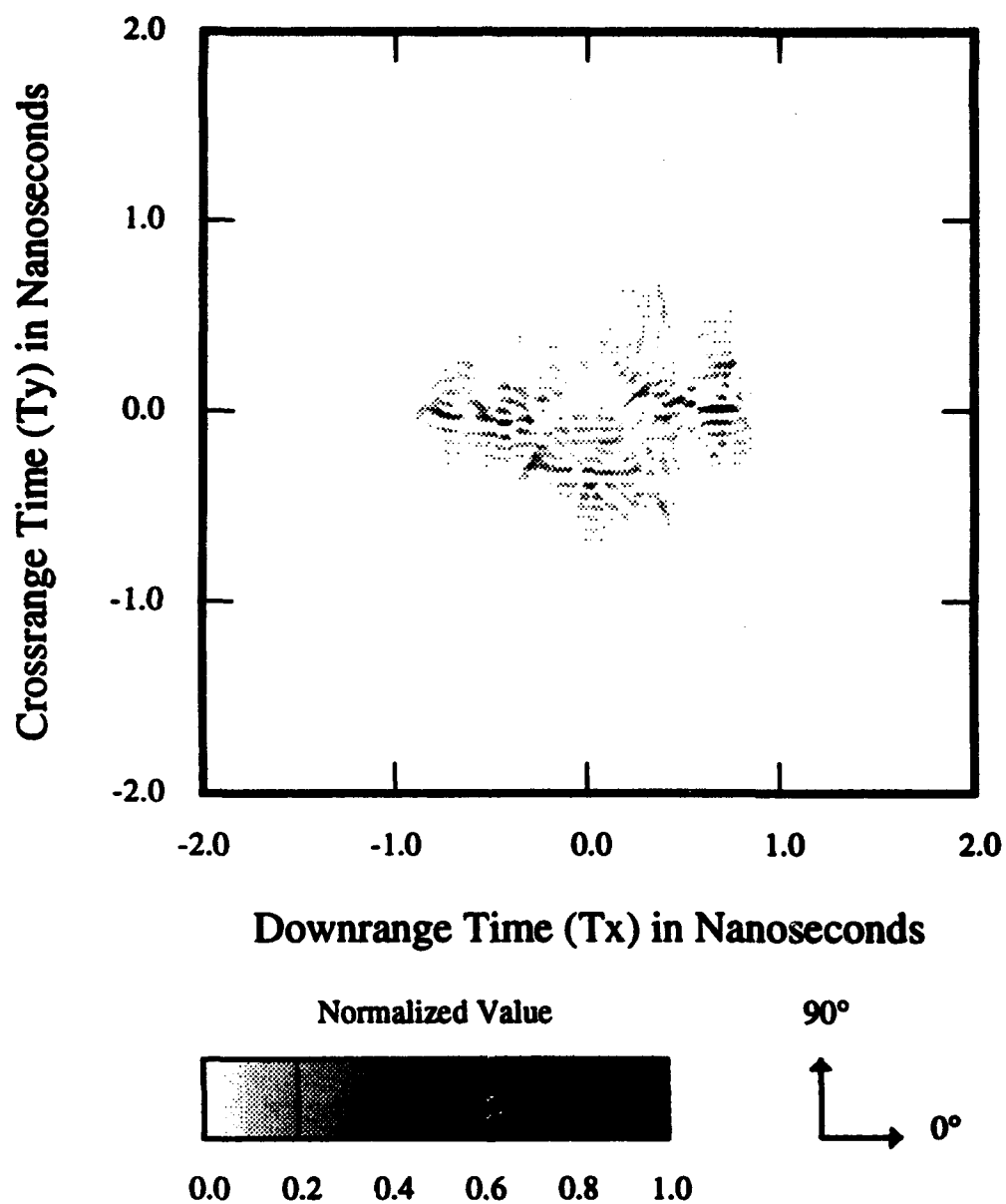Normalized Value   90°

-1.0   -0.5   0.0   0.5   1.0   0°

Figure 22: F-4 Phantom Model. This plot shows $g(x, y)$.

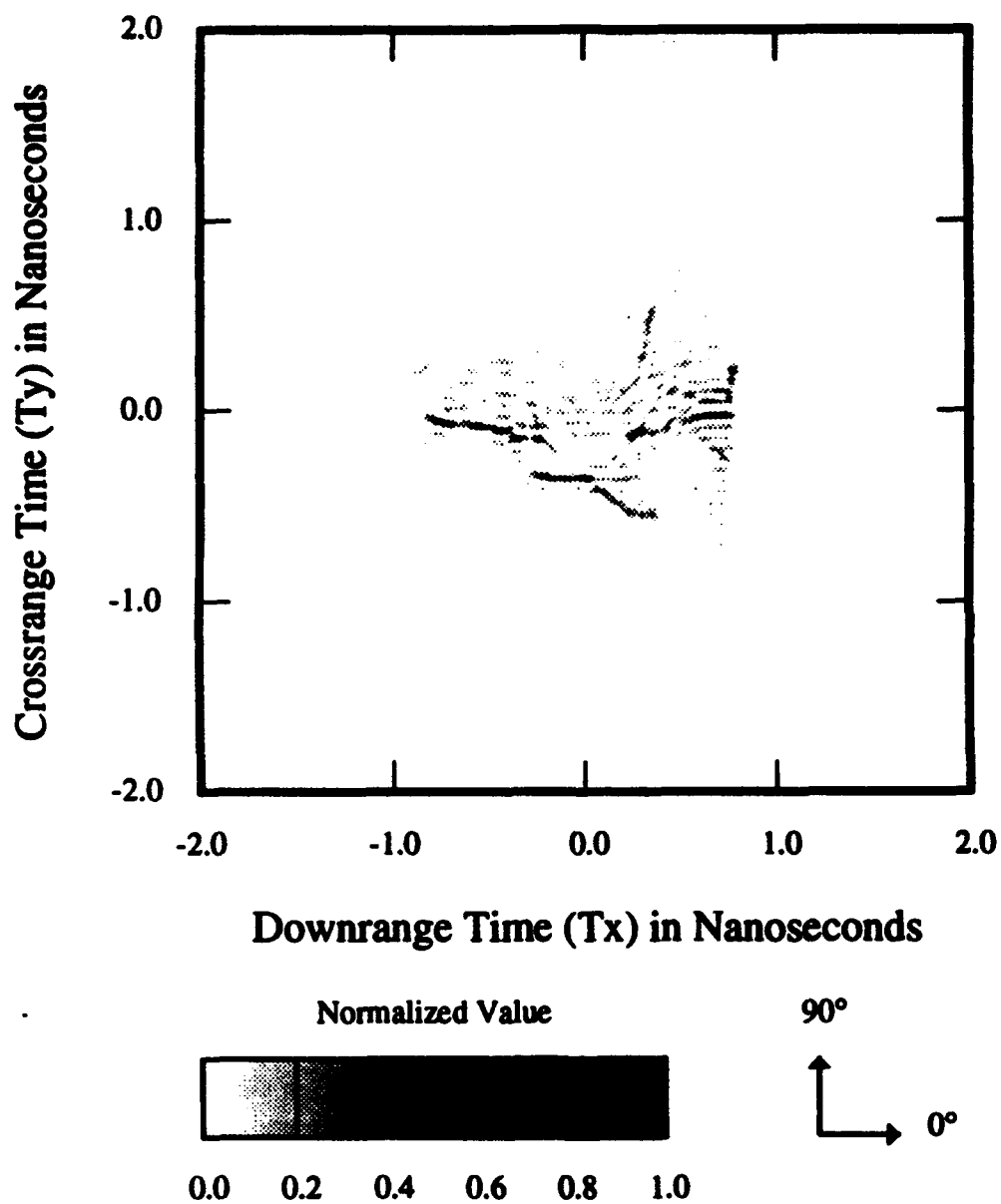Figure 23: F-4 Phantom Model. This plot shows $g(x,y)$ for $g(x,y) > 0$, otherwise 0.

Figure 24: F-4 Phantom Model. This plot shows $| g(x,y) |$ for $g(x,y) < 0$, otherwise 0.

Table 1: Filters for $g(x, y)$

Name	function	
Offset	g(x,y) + constant	
Positive Clip	g(x,y)	if $g(x,y) > 0$
	0	if $g(x,y) < 0$
Negative Clip	0	if $g(x,y) > 0$
	-g(x,y)	if $g(x,y) < 0$
Threshold	g(x,y)	if $|g(x,y)| > c$
	0	otherwise,
		where c is a constant

Gibb's phenomena become more noticeable in these figures because of the contrast. More importantly in Figure 21, the tail of the F-4 is composed of two stripes. In Figures 22 to 24, the same part is composed of negative and positive stripes. One other important visual filter is the threshold filter. The filter suppresses low level signals. In particular for images with a good signal to noise or clutter level, the threshold filter filter will enhance the visual perception of the image. This is illustrated in Figure 25. From this image, the outline of the aircraft is more defined. The increased visual perception of the image also allows Gibb's phenomena to be seen. Since Gibb's phenomena can be seen in the image, suppression of the phenomena can be accomplished by filtering the image.

4.2 Downrange Filter

All of the images shown before this section did not have any filtering functions applied to the data. As a result, Gibb's phenomena are present and is visible in the images. One method of reducing the Gibb's phenomena is to filter the data before generating the image. Often, one desires to have both a full resolution image with
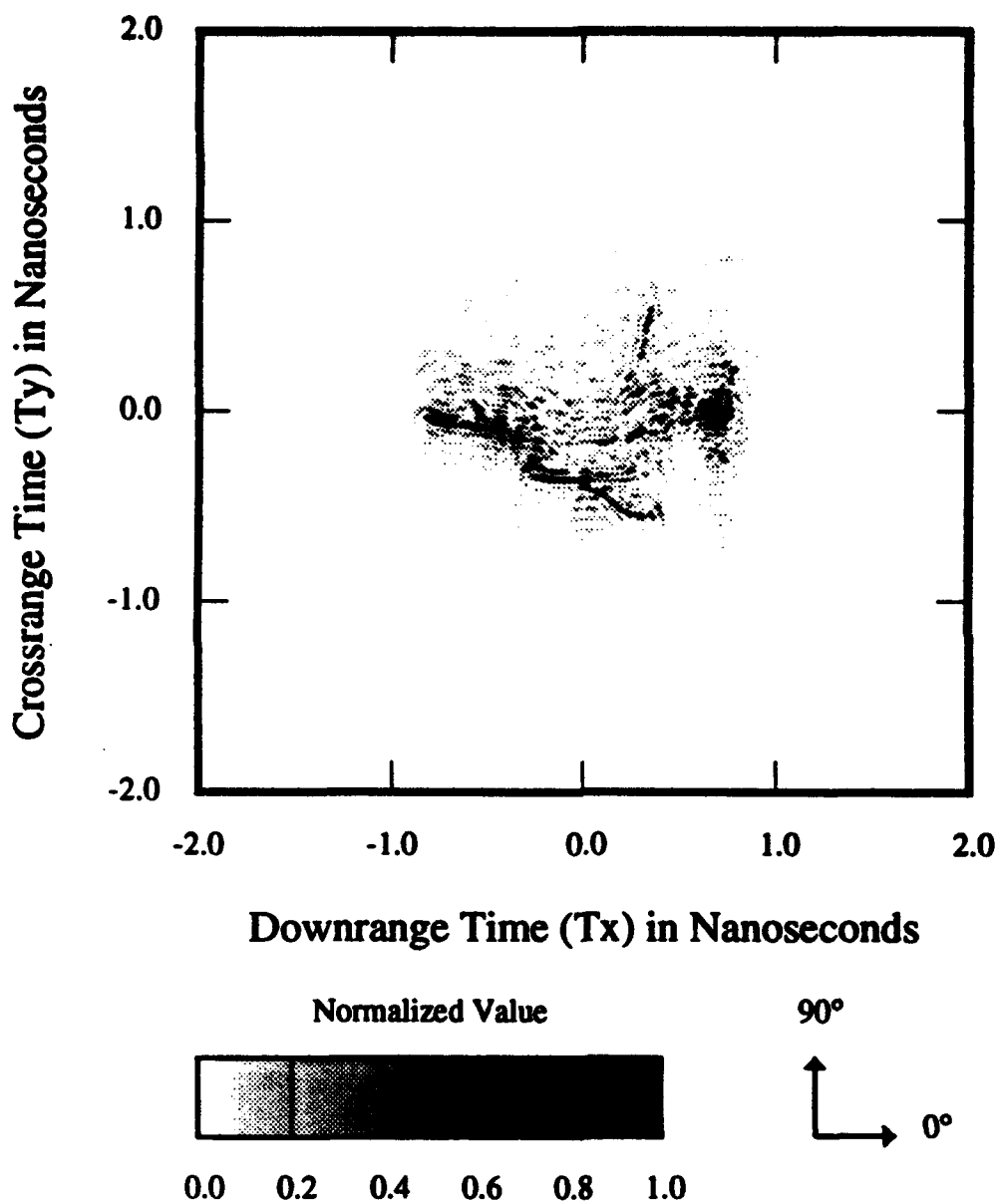
Figure 25: Example of Threshold Filter. F-4 phantom model. This plot shows $|g(x,y)|$. This figure not to scale.

Gibb's phenomena and a filtered image because the full resolution image usually shows more detail. However, this method would require generating two images. Instead, one may note, from Equations (25) and (51), that an equivalent filter be done by filtering the image frequency domain. If $W(\omega)$ is the one-dimensional waveform filter, the equivalent two-dimensional filter is $W_2(\omega, \theta) = W(\omega)$.

Figures 26, 27, and 28 show the F-4 Phantom images after a low-pass, band-pass, and high-pass filtering, respectively. Note that the figures have lost a substantial amount of resolution due to the filters. This effect is known as vignetting. Instead, one may wish to apply the filter over a portion of the frequency spectrum. The results of the frequency domain taper are shown in Figures 29 to 31. In these figures, the tapered images show a shaper peaks when compared with the traditional filtering.

4.3   Angular Filter

Some scattering centers are visible for narrow angular regions. These scattering centers appear weak compared to point scatters because the narrow scatters are averaged over all the measured data even when their response is shadowed. In order to observe these scattering centers, one may generate a limited aperture image. By limiting the angular aperture, the point scatters are "weaker" since fewer look angles are summed. By generating a limited angular aperture, image artifacts appear in the image. These artifacts may be readily seen in Figure 32 which shows an image generated for 90° of data. As one may observe in the images, large stripes are going across the images. These stripes result from the discontinuity in the data space in the angular direction.
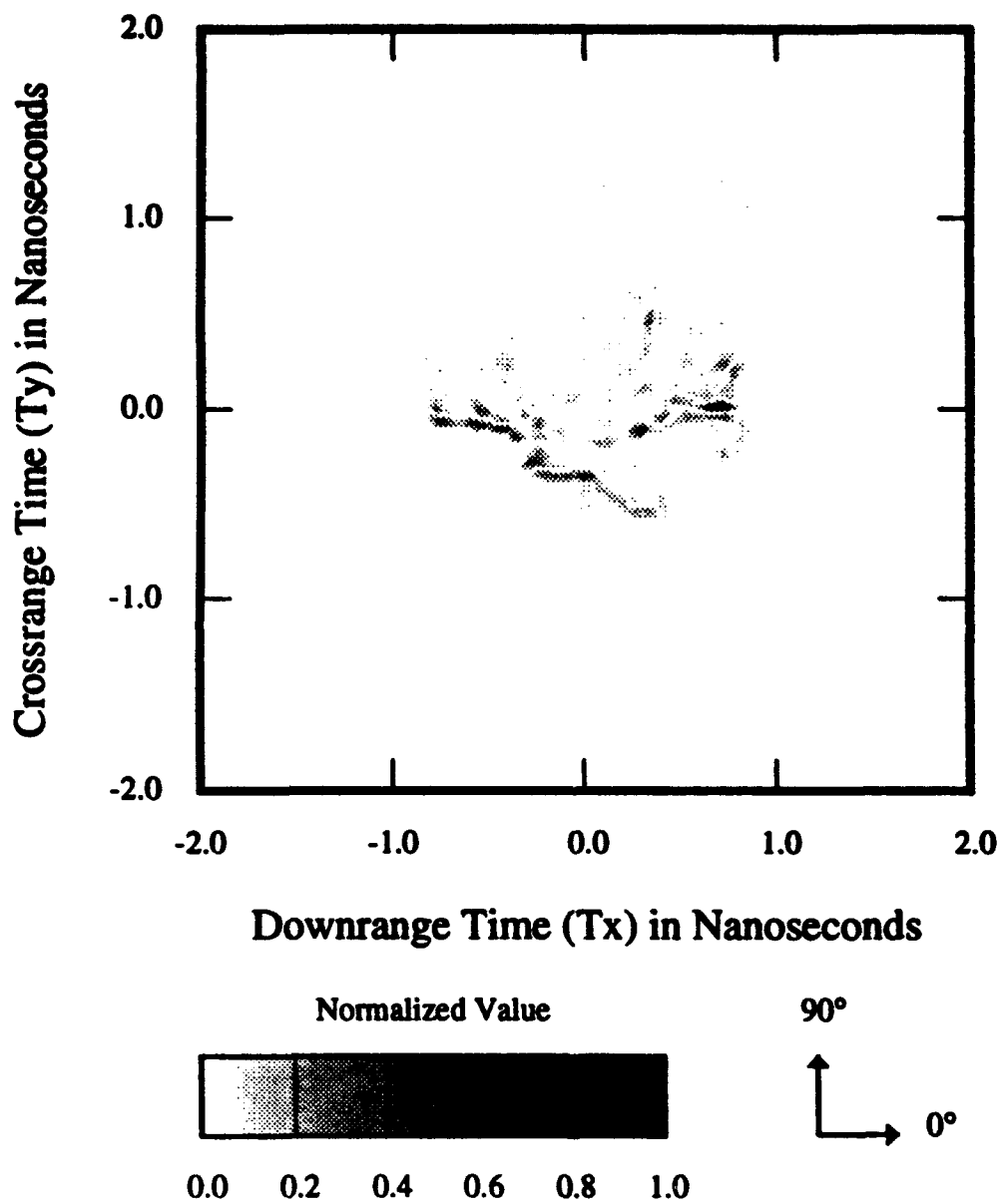
Figure 26: F-4 Phantom Model with a Low-Pass Kaiser-Bessel Filter of Alpha 2.
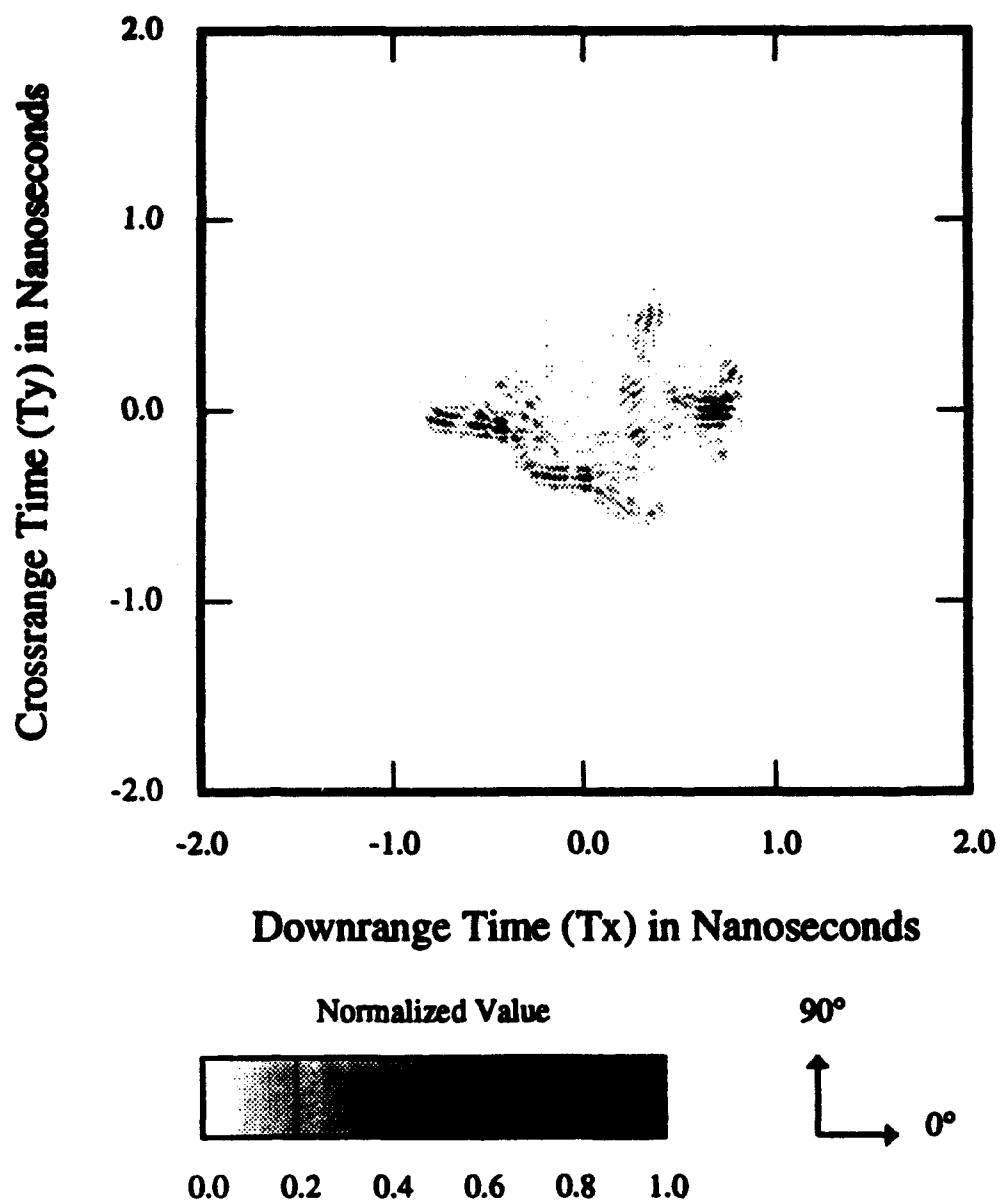This plot shows $| g(x,y) |$.

Figure 27: F-4 Phantom Model with a Band-Pass Kaiser-Bessel Filter of Alpha 2. This plot shows $| g(x, y) |$.
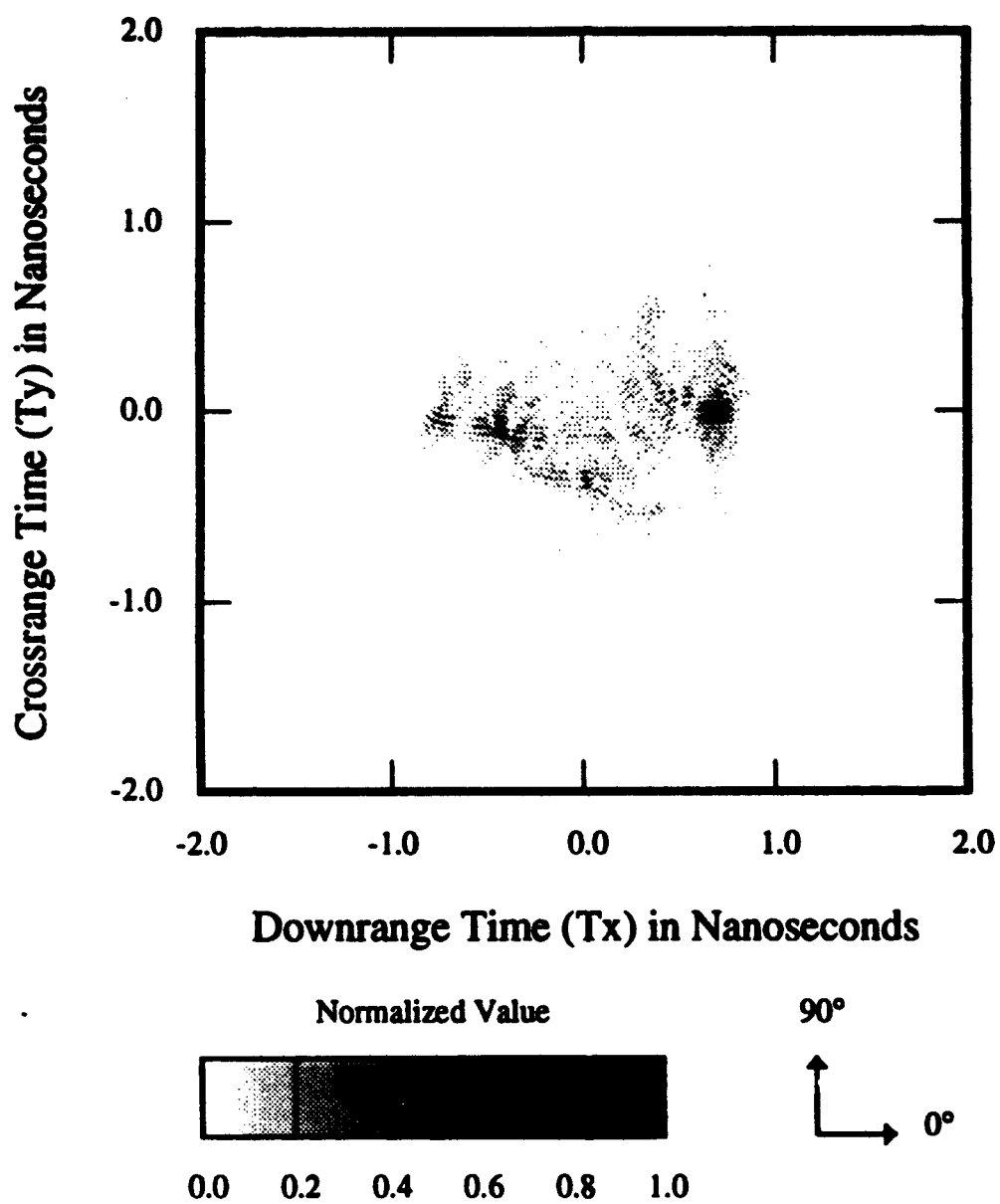
Figure 28: F-4 Phantom Model with a High-Pass Kaiser-Bessel Filter of Alpha 2. This plot shows $| g(x,y) |$.
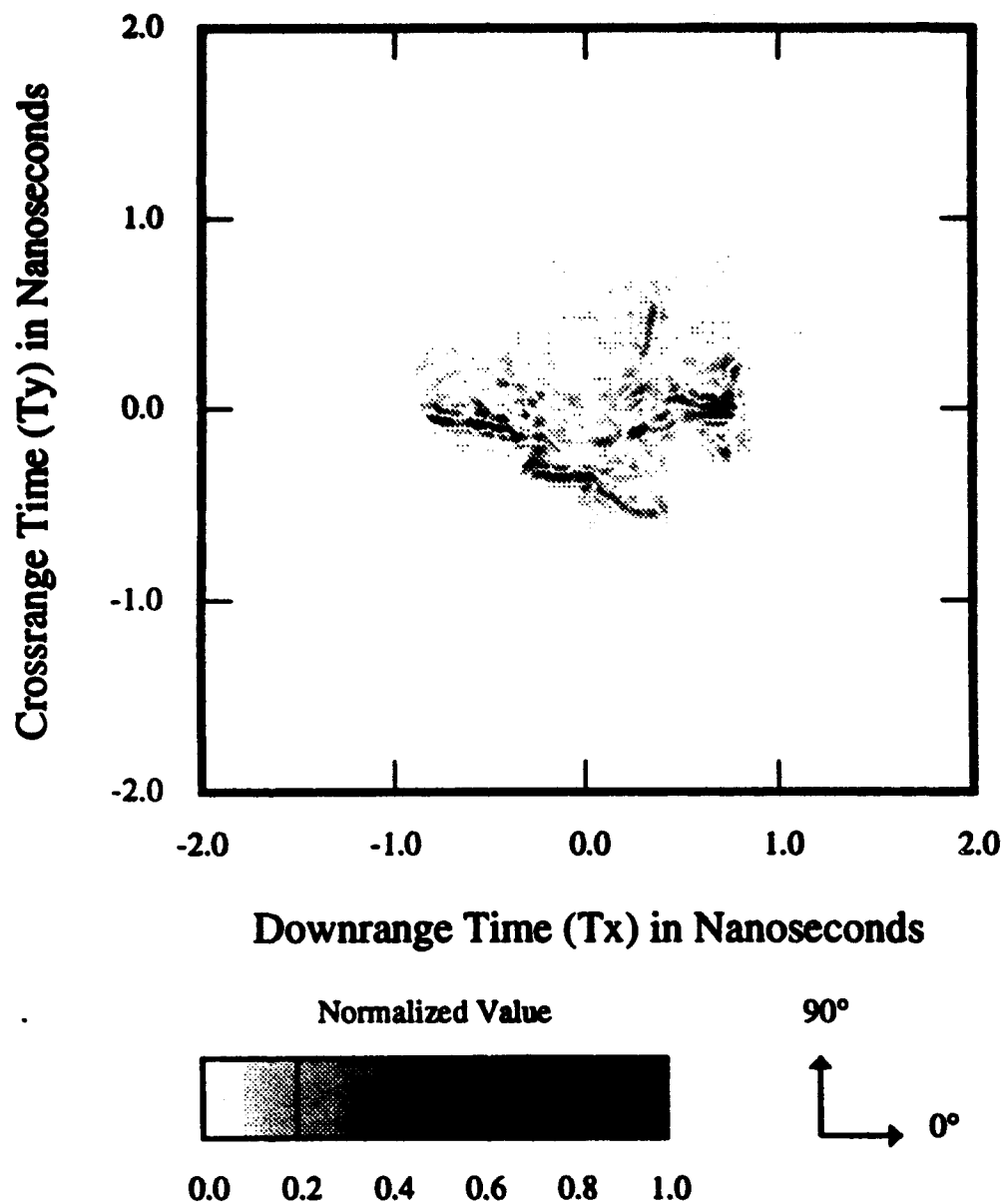
Figure 29: F-4 Phantom Model with a Tapered Low-Pass Kaiser-Bessel Filter of Alpha 2. This plot shows | $g(x, y)$ |.
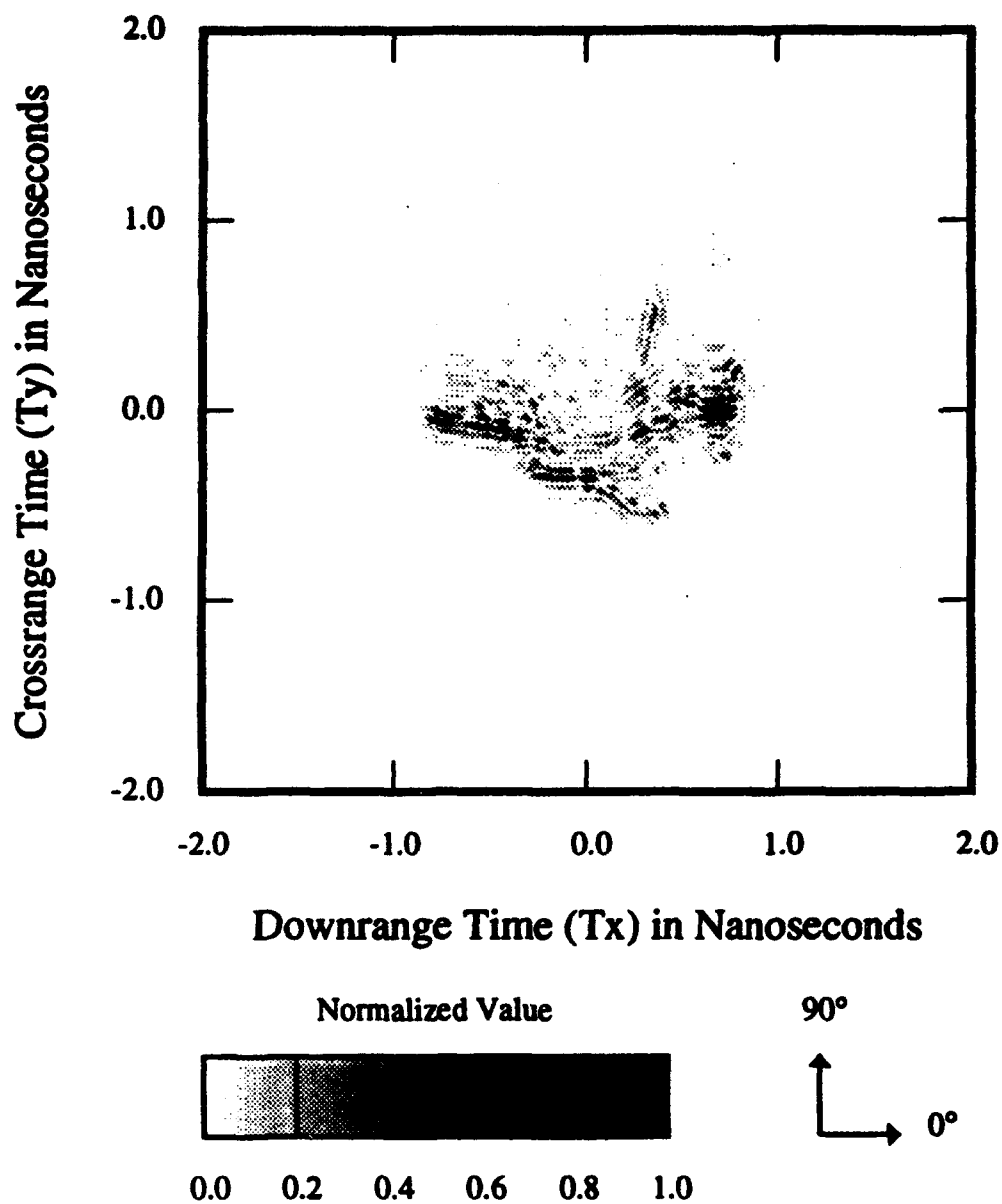
Figure 30: F-4 Phantom Model with a Tapered Band-Pass Kaiser-Bessel Filter of Alpha 2. This plot shows $| g(x,y) |$.
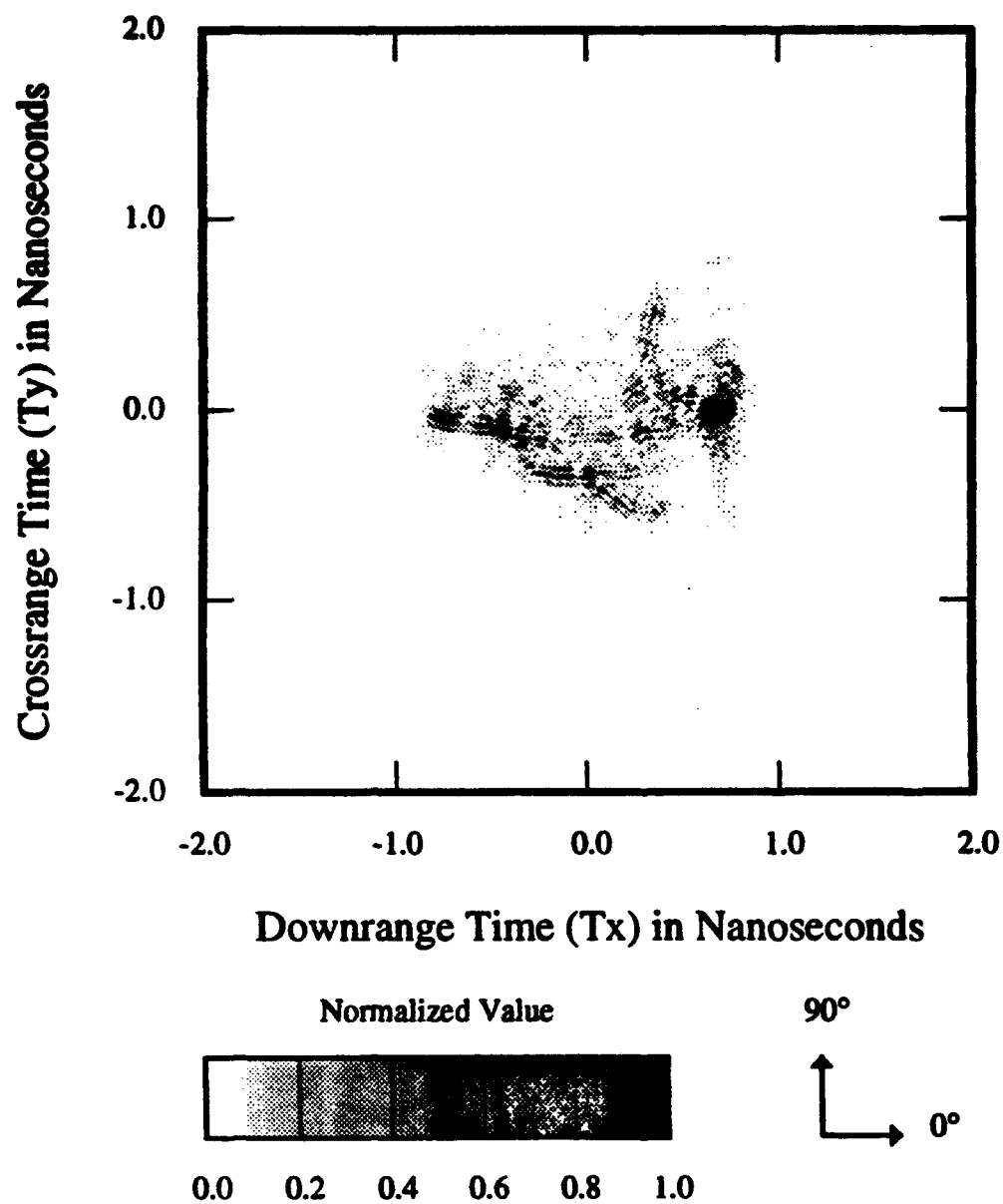
Figure 31: F-4 Phantom Model with a Tapered High-Pass Kaiser-Bessel Filter of Alpha 2. This plot shows | $g(x,y)$ |.
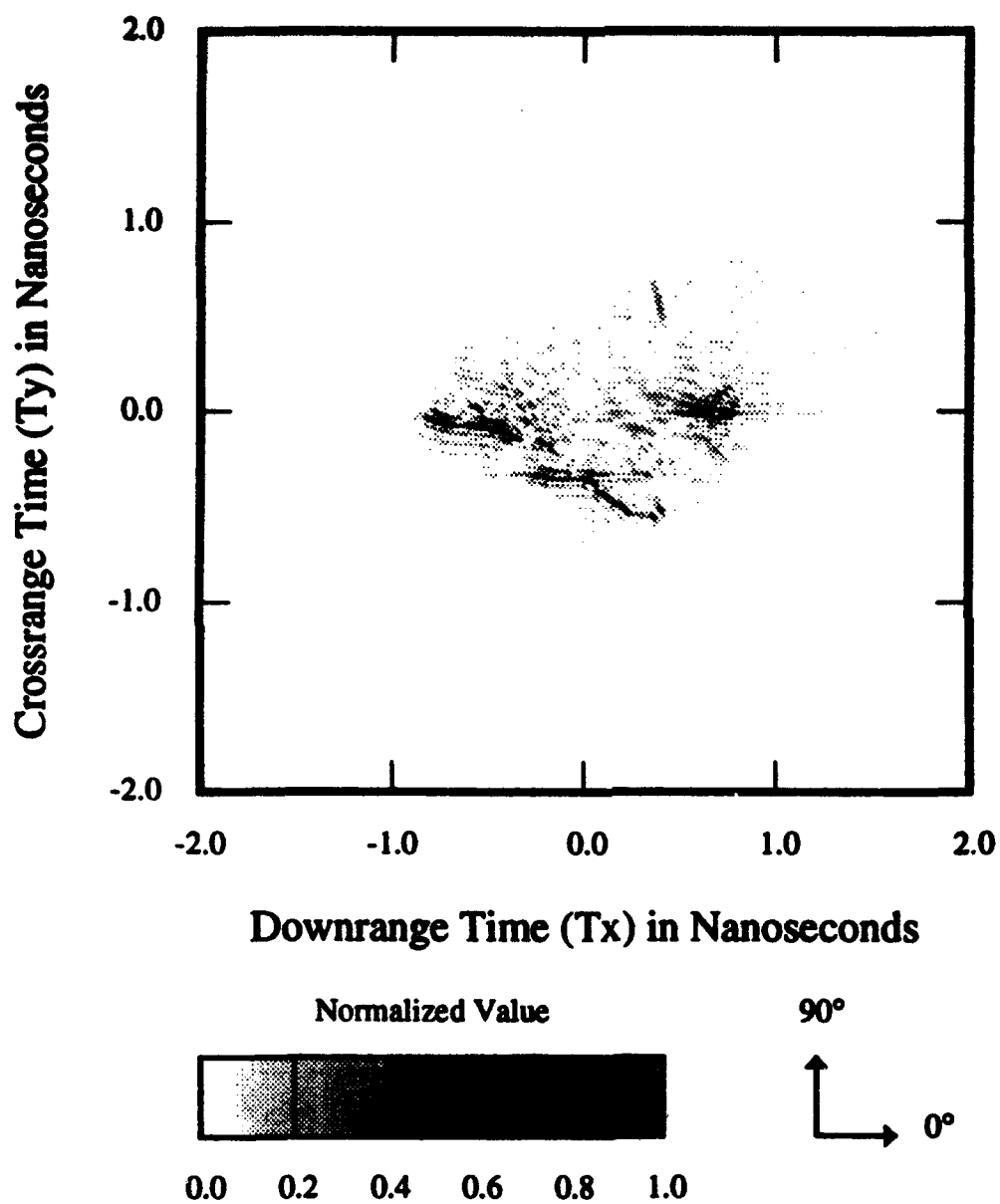
Figure 32: F4 Phantom Model Reconstructed by Interpolation using 90 Deg of Data. The data were taken at 1° increments from 2 GHz to 18 GHz.

SECTION 5

Imaging Results

Imaging results produced by the computer program are shown in this chapter. Images of a scale model F-4 fighter aircraft, a scale model M35 truck, and foliage are shown. All of these images, except the SAR images, were generated using a 512x512 matrix. The SAR images were generated using a 1650x1650 matrix in order to satisfy the Nyquist sampling.

5.1   F-4 Phantom

Data from a 1/72 scale F-4 Phantom model airplane were taken in the OSU compact range to generate an image. The data have a frequency range 2–18 GHz sampled at 20 MHz increments. Angular samples were made at 1° increments. The total model length was 9 inches long. The F-4 data are used for comparing the Fourier Slice and convolution backprojection algorithms. Only horizontal polarization is shown for all the Phantom images. Unless otherwise stated, the author has normalized all F-4 images in the same manner. ·   iparison between the Phantom figures is meaningful.

Figures 33 and 34 show a Fourier Slice image produced using a 5-point sinc interpolation while Figures 35 and 36 shows a convolution backprojection image. Note that Figures 33 and 35 show $| g(x,y) |$ while Figures 34 and 36 show $| G(k_x, k_y) |$. As one would expect, visually the two different methods are comparable since the
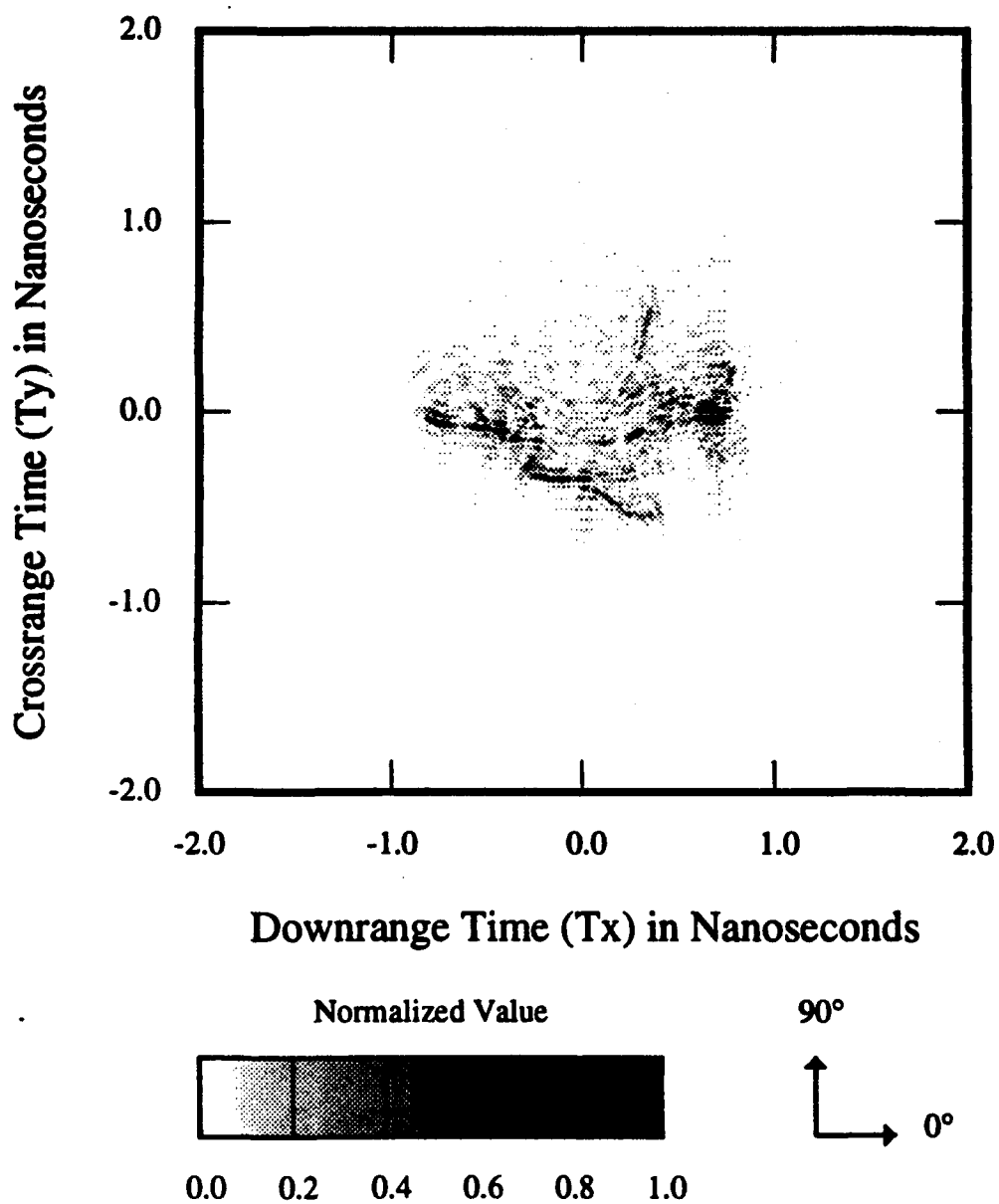
Figure 33: F-4 Phantom Model Reconstructed Using the Fourier Technique Using a 5-Point Sinc Interpolation. This plot shows $| g(x,y) |$.
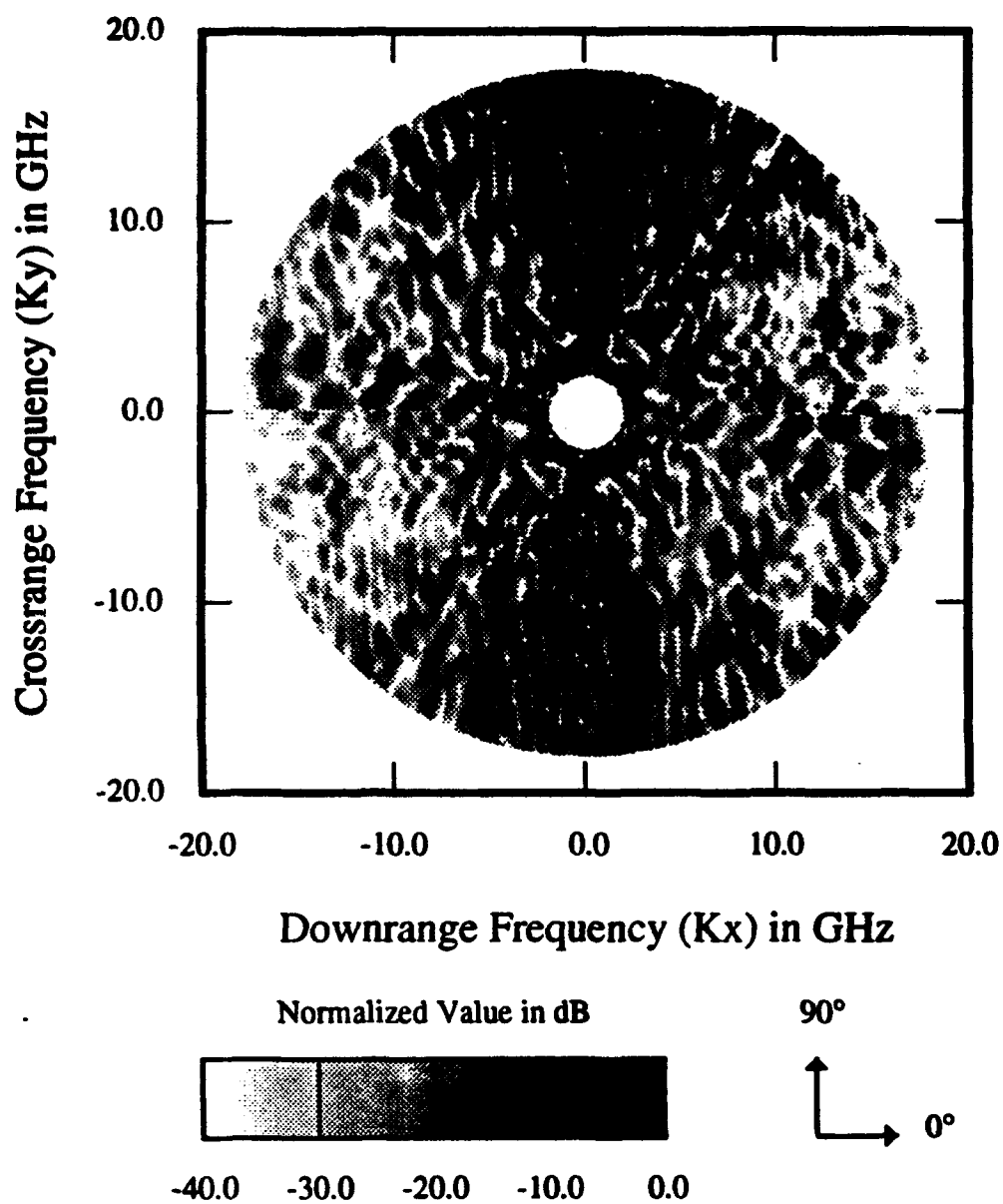
Figure 34: F-4 Phantom Model Reconstructed Using the Fourier Technique Using a 5-Point Sinc Interpolation. This plot shows $| G(k_x, k_y) |$.
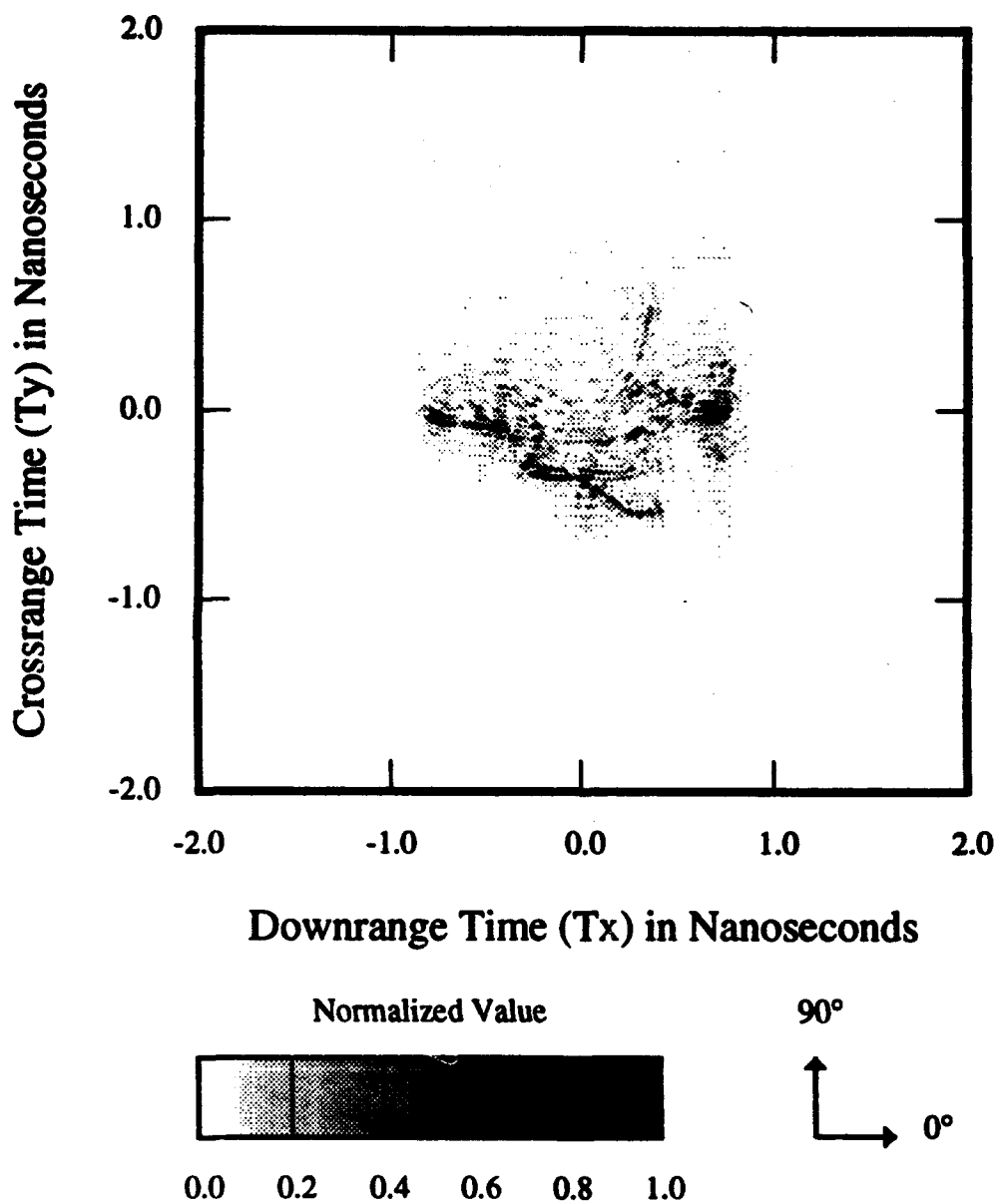
Figure 35: F-4 Phantom Model Reconstructed Using the Convolution Backprojection Method. The data were taken at 1° increments from 2 GHz to 18 GHz. This plot shows $| g(x, y) |$.
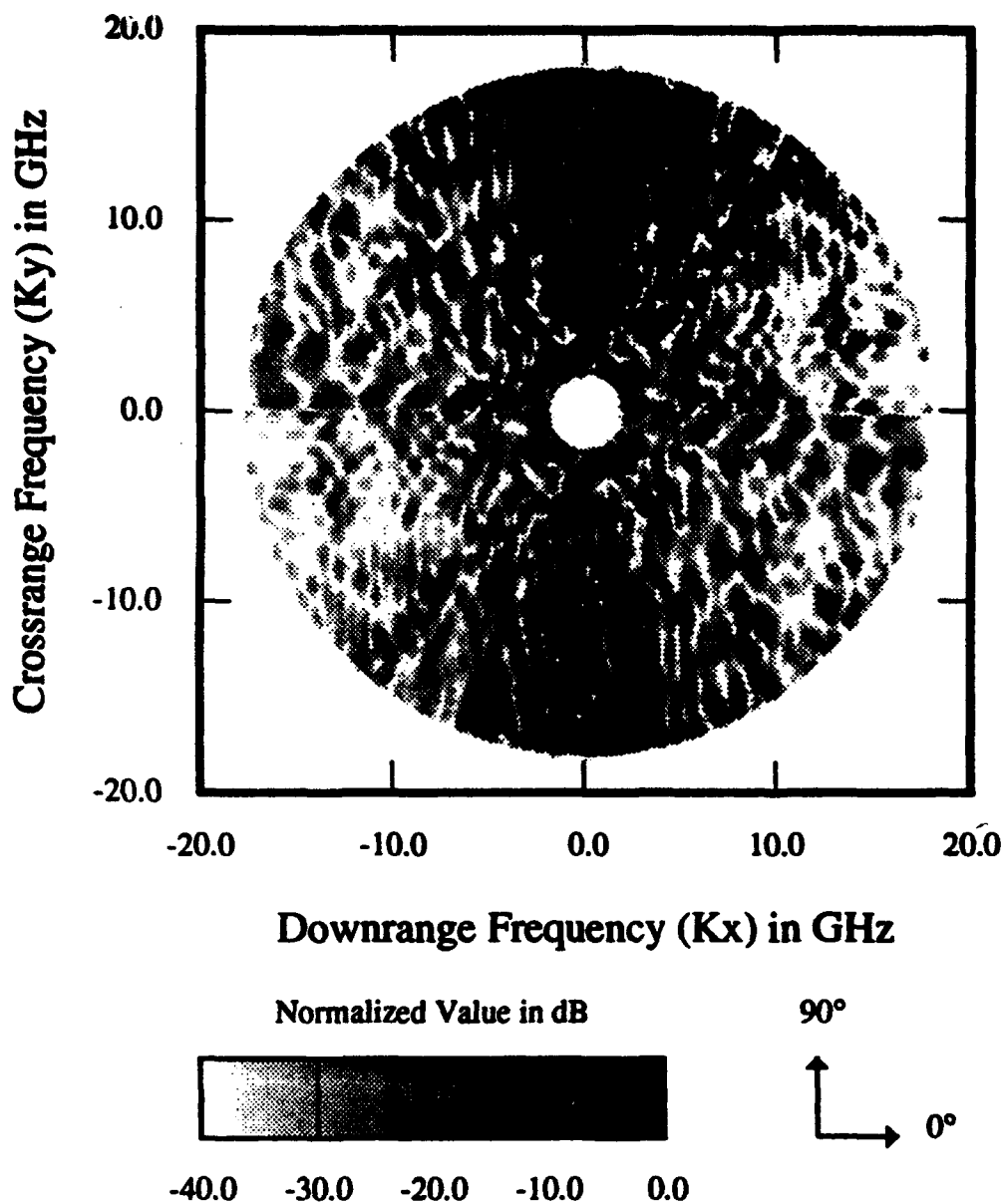
Figure 36: F-4 Phantom Model Reconstructed Using the Convolution Backprojection Method. The data were taken at 1° increments from 2 GHz to 18 GHz. This plot shows $| G(k_x, k_y) |$.

two methods are mathematically equivalent. Figure 37 shows the same model reconstructed by the Fourier Slice method using linear interpolation (same technique, but different interpolation type). The results of the Fourier method using the higher order interpolation is comparable to the convolution backprojection method. Images not explicitly labeled as the Fourier method have been generated using the convolution backprojection technique.

As one may see in the F-4 images, the entire outline of an airplane is not visible for 180 degrees of data. The reason, for only part of the outline being visible, is due to the imaging assumption that the scattering centers behave like isotropic point scatterers. In the real world, some of the "rear" scattering centers are shadowed, and one cannot completely characterize an object with only 180 degrees of data. This may be readily seen as a discontinuity in $| G(k_x, k_y) |$. In Figures 34 and 36, the discontinuity is seen on the x-axis.

Occasionally, one may find it useful to completely characterize an object in an image. One common method, to accomplish this task, is to arbitrarily extend the angular range to 360 degrees instead of the 180 degrees in the imaging algorithm. To illustrate this, Figure 38 shows an image generated using 360 degrees of data by assuming that the target is symmetric. (This assumption was made because only 180 degrees of data were available.) Notice in the frequency domain image, Figure 39, the discontinuity has disappeared. However, the spectrum is different.

Image artifacts also arise in the convolution backprojection imaging technique in images that do not satisfy the angular Nyquist sampling rate. In particular, one needs to understand the effects in the images caused by angular sampling. In the convolution backprojection method, artifacts become prominent near the angular Nyquist rate. For example, Figure 40 shows a convolution-backprojection image of the F-4 Phantom model sampled at 2-degree increments with a maximum frequency of 14 GHz. At the outer edges of the image, one can see some radial lines (and looks like a Moiré pattern). This pattern results from undersampling Equation (28) at
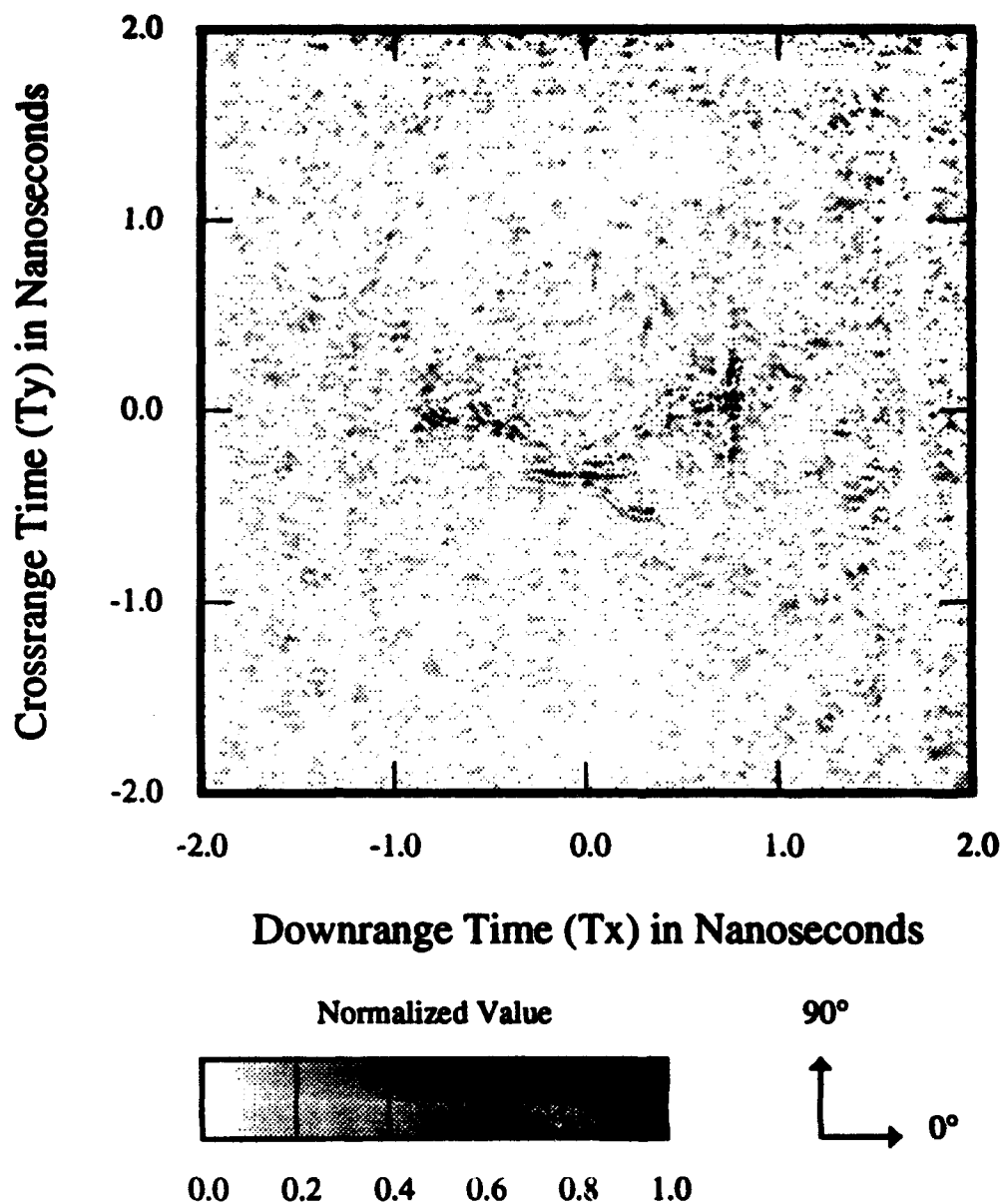
64

Figure 37: F-4 Phantom Model Reconstructed Using the Fourier Technique Using Linear Interpolation. The data were taken at 1° increments from 2 GHz to 18 GHz. This plot shows $| g(x,y) |$. Magnitude is not to scale with other figures.
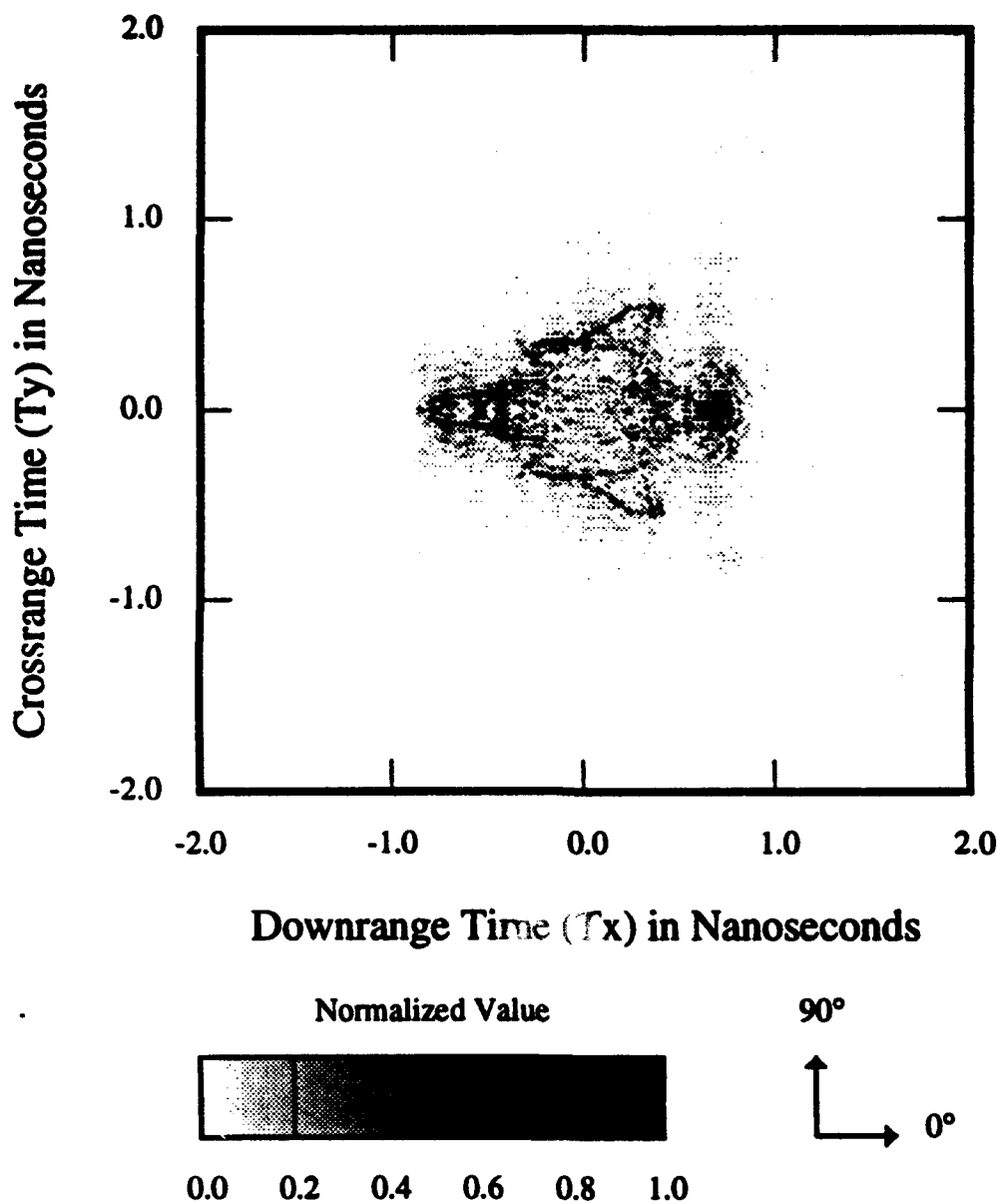
65

Figure 38: F-4 Phantom Model Reconstructed Using 360° of Data. The data were taken at 1° increments from 2 GHz to 18 GHz. This plot shows $| g(x,y) |$.
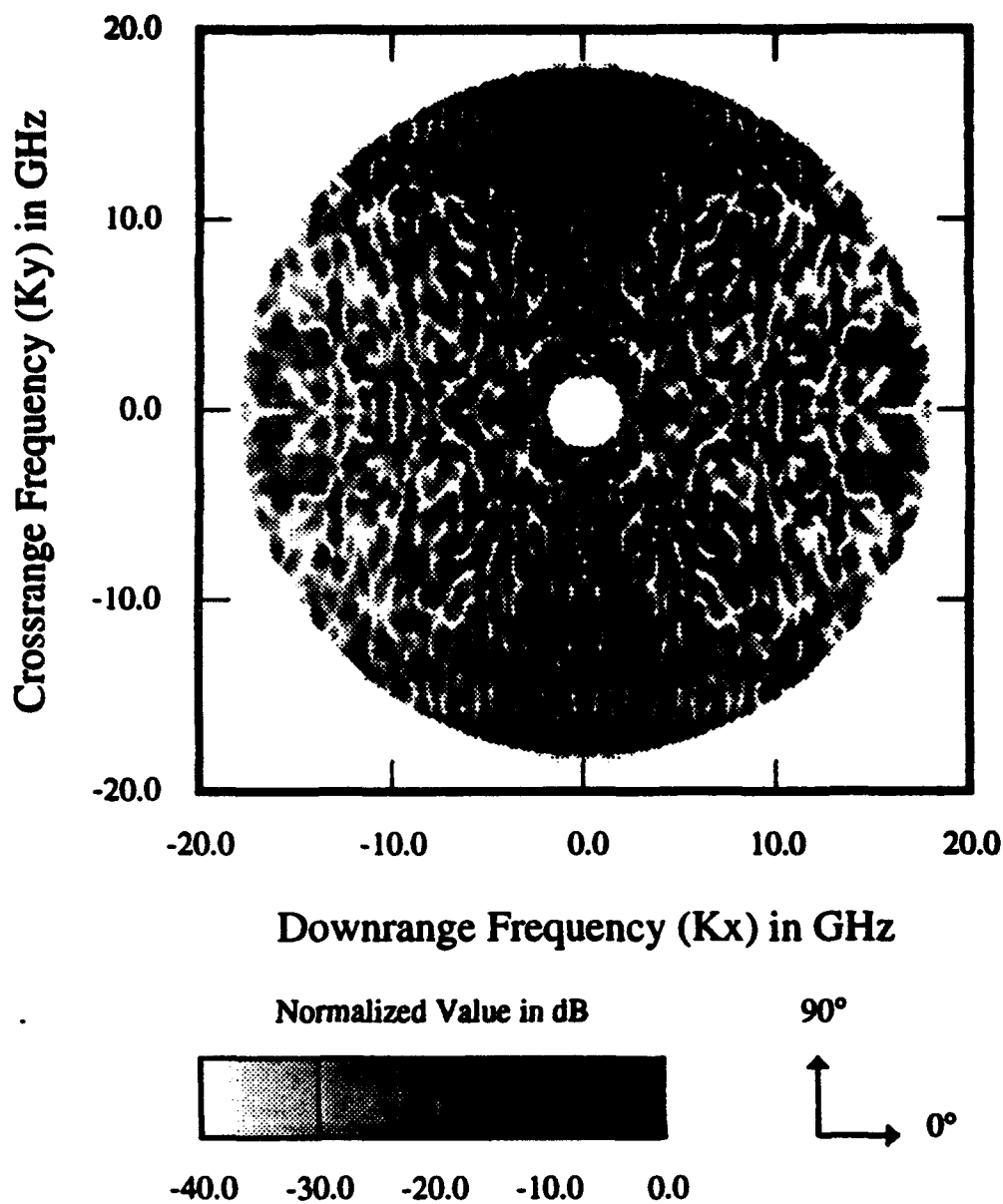
Figure 39: F-4 Phantom Model Reconstructed Using 360° of Data. The data were taken at 1° increments from 2 GHz to 18 GHz. This plot shows $| G(k_x, k_y) |$.

that radial distance. The two-dimensional Fourier transform of the image shown in Figure 40 is shown in Figure 41. At the outer edges of the annulus in the frequency domain image, the frequency spectrum is no longer continuous, and a set of radial lines can be seen. At these frequencies, the angular sampling does not meet the Nyquist criteria. The radial lines are the result of each measured look angle that was used in performing the backprojection when generating the image. Further effects of angular Nyquist sampling are shown with the M35 truck.

5.2 M35 Truck

This section shows two-dimensional images generated from data taken at the OSU compact range. The target selected was a 1/16 scale M35 truck model, shown in Figure 42. Data are available for two elevation angles, 0° and 45°. The data were sampled from 2-18 GHz at 20 MHz increments with the center of the truck as the axis of rotation. The azimuth sampling rates are 1° for 0.9° for 0° and 45° elevation, respectively. Only vertical polarization is shown for the truck images. First a waterfall plot will be shown for 0° elevation. Fourier Slice and convolution backprojection images will also be shown for 0° elevation. A projected three-dimensional image will be shown for the 45° elevation.

Figure 43 shows a waterfall plot of the truck at 0° elevation. Since the target is rotated about an axis, the scattering centers track in sinusoidal fashion, when seen as a function of look angle. The white horizontal stripe seen in the waterfall plot is a missing data file . Many interactions can be seen in the waterfall plot. As seen in the figure, the plot is difficult to interpret when there are many scattering centers.

Imaging is used to help the user interpret the data. Figures 44 through 47 show images of the truck at 0° elevation. Figure 44 was made by convolution backprojection. Figure 45 was made by Fourier Slice. Both convolution backprojection image and Fourier Slice images were generated using the same data. One drawback to the Fourier Slice image is that it is aliased. The aliasing is caused becaused the
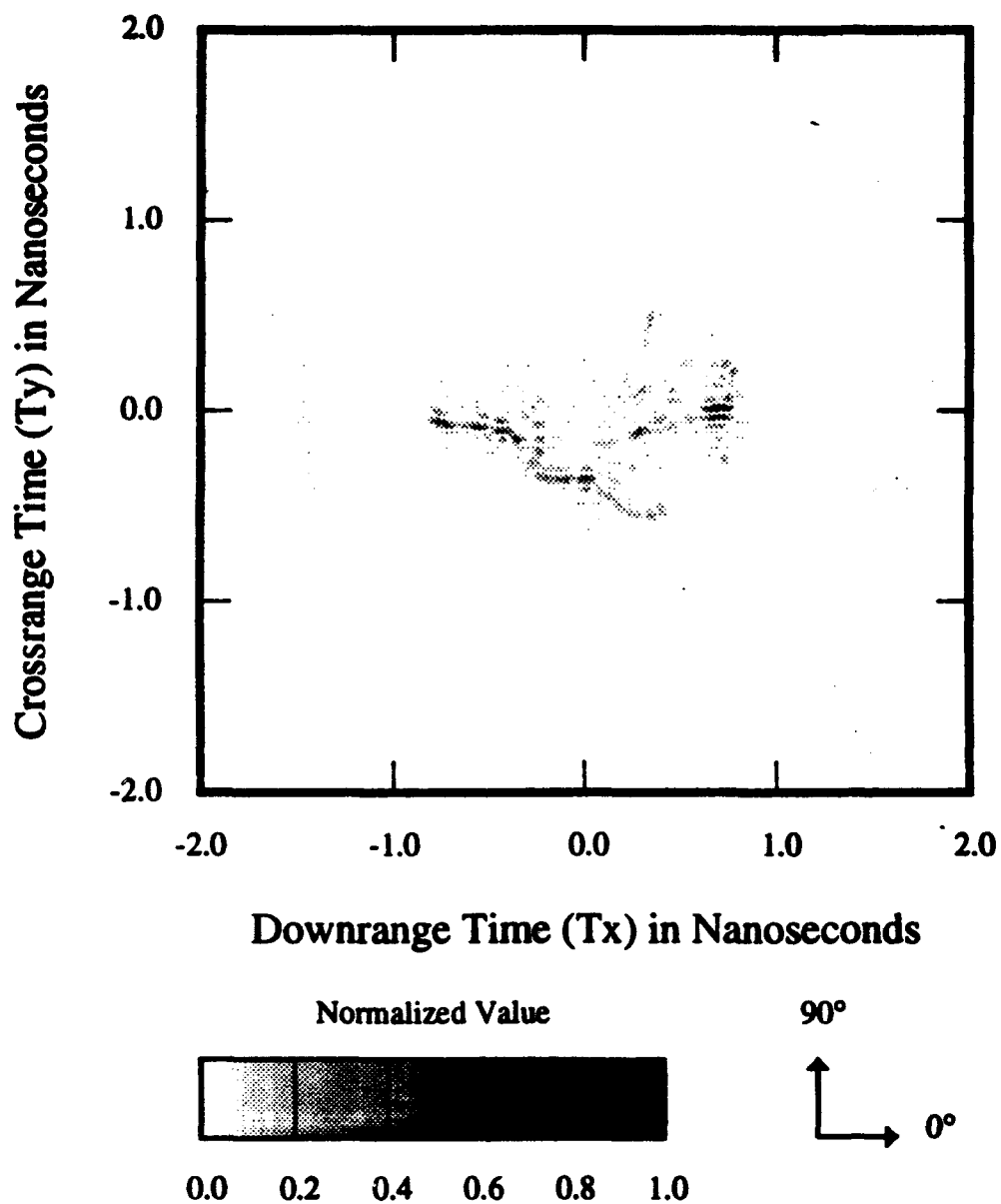
Figure 40: F-4 Phantom Model Reconstructed from Data Taken at 2° Increments from 2 GHz to 14 GHz. This plot shows $| g(x, y) |$.
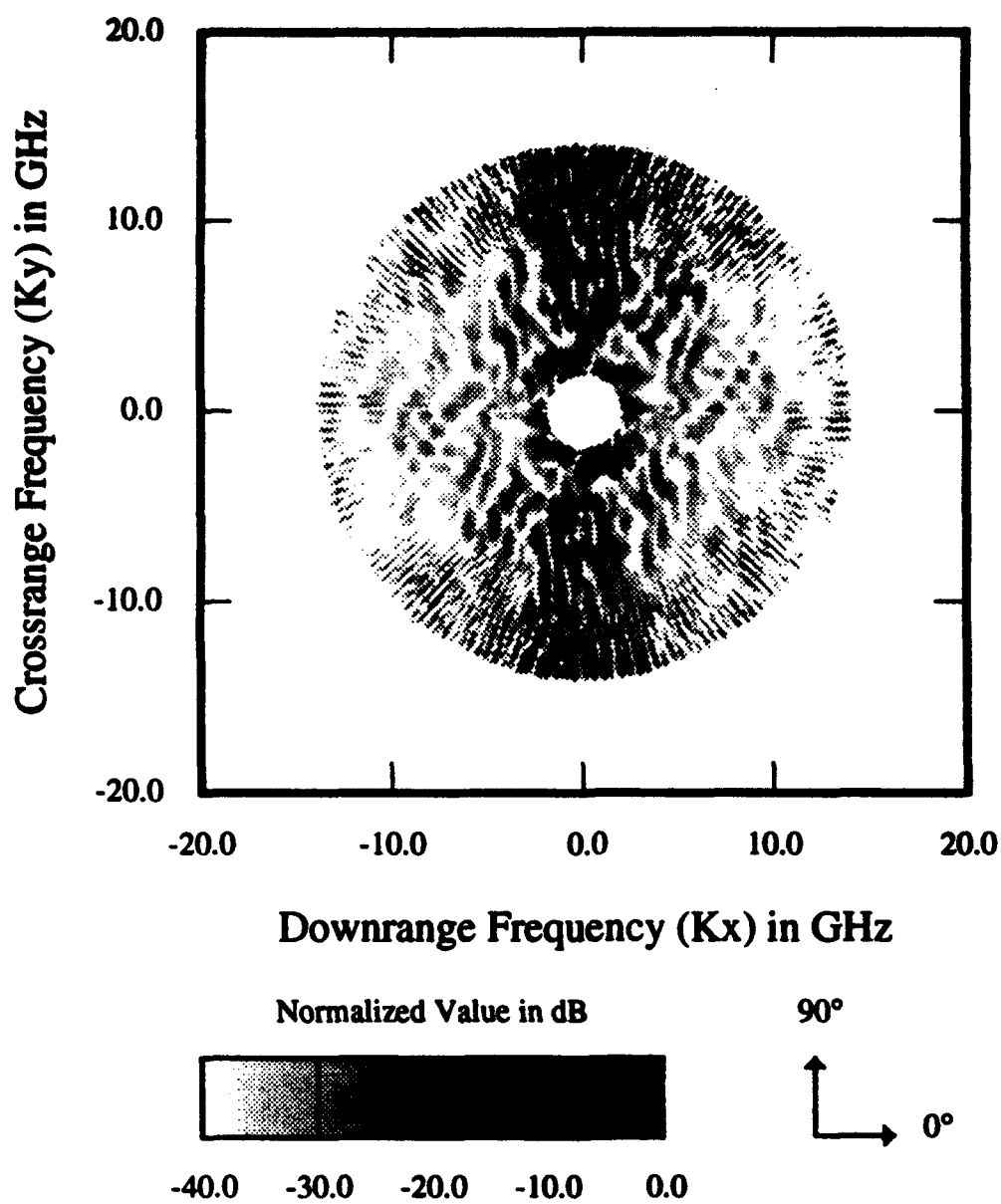
Figure 41: F-4 Phantom Model Reconstructed from Data Taken at 2° Increments from 2 GHz to 14 GHz. This plot shows $| G(k_x, k_y) |$.
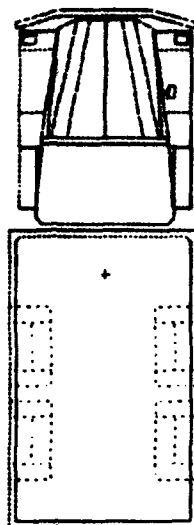
Figure 42: Model M35 Truck. 1/16 Scale.

measured data are sampled for a larger time window. The aliasing occurs in Fourier Slice because the image is generated directly in the frequency domain. In convolution backprojection, the data are transformed into a filtered time domain response and resampled. In order to generate a correct Fourier Slice image, the data need to be time gated before the Fourier Slice algorithm is applied. Figure 46 shows the resulting image. Note that the aliasing near $T_x = 2$ and $T_x = 3$ nS in Figure 45 has been removed.

The two images are equivalent in the region where Nyquist sampling is satisfied. The Moiré pattern is visible in convolution backprojection while there is no Moiré pattern in the Fourier slice image. This lack of pattern in the Fourier Slice image is caused because the implementation of Fourier Slice interpolates angular samples. As a result, an equivalent convolution backprojection image, shown in Figure 47, can be generated by interpolating angular samples. The presence of image artifacts causes difficulty in identifying scattering centers.

Some very noticeable scattering centers in the truck images are the reverberations caused by the truck bed in vertical polarization. Because the reverberation is not a
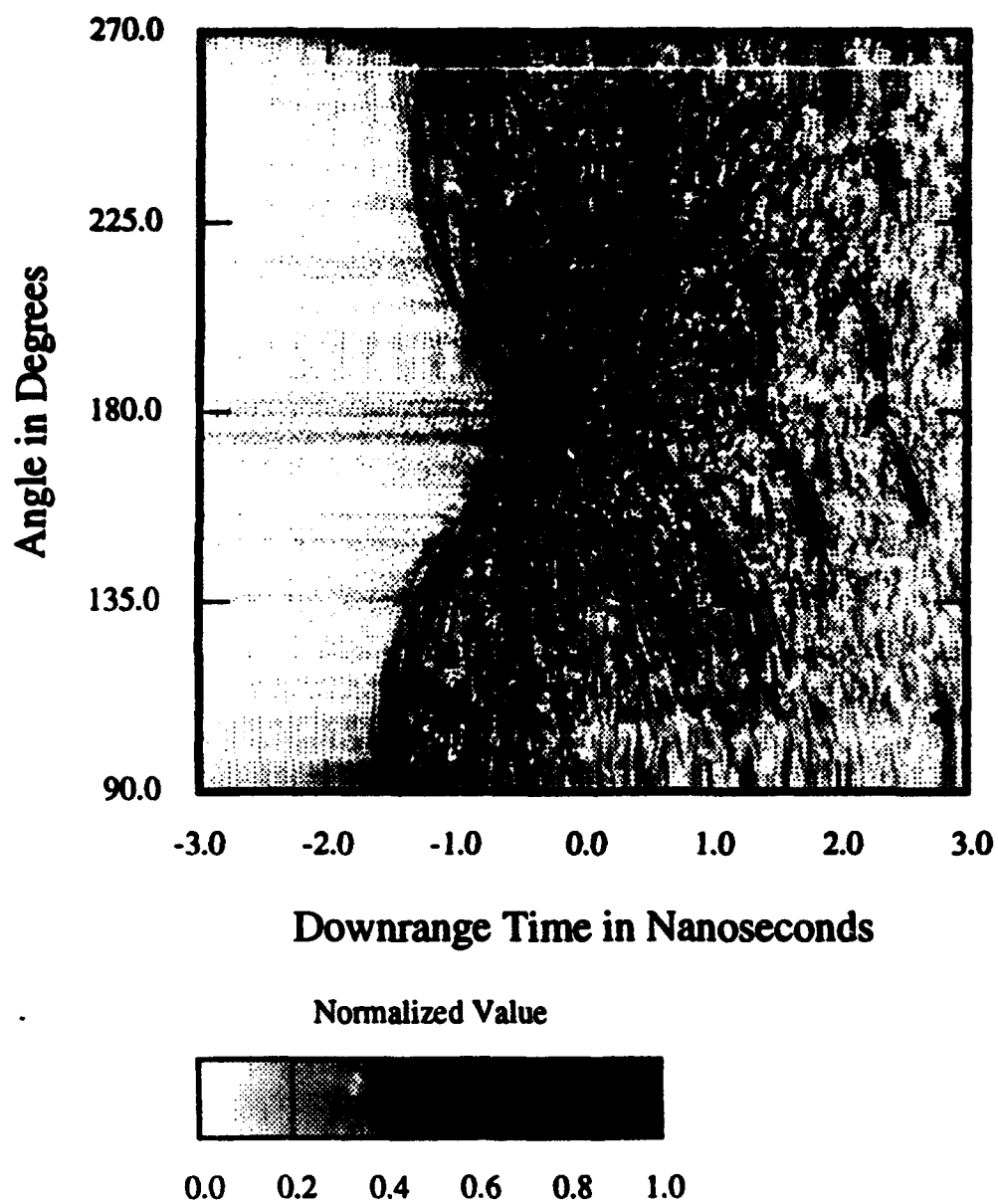
71

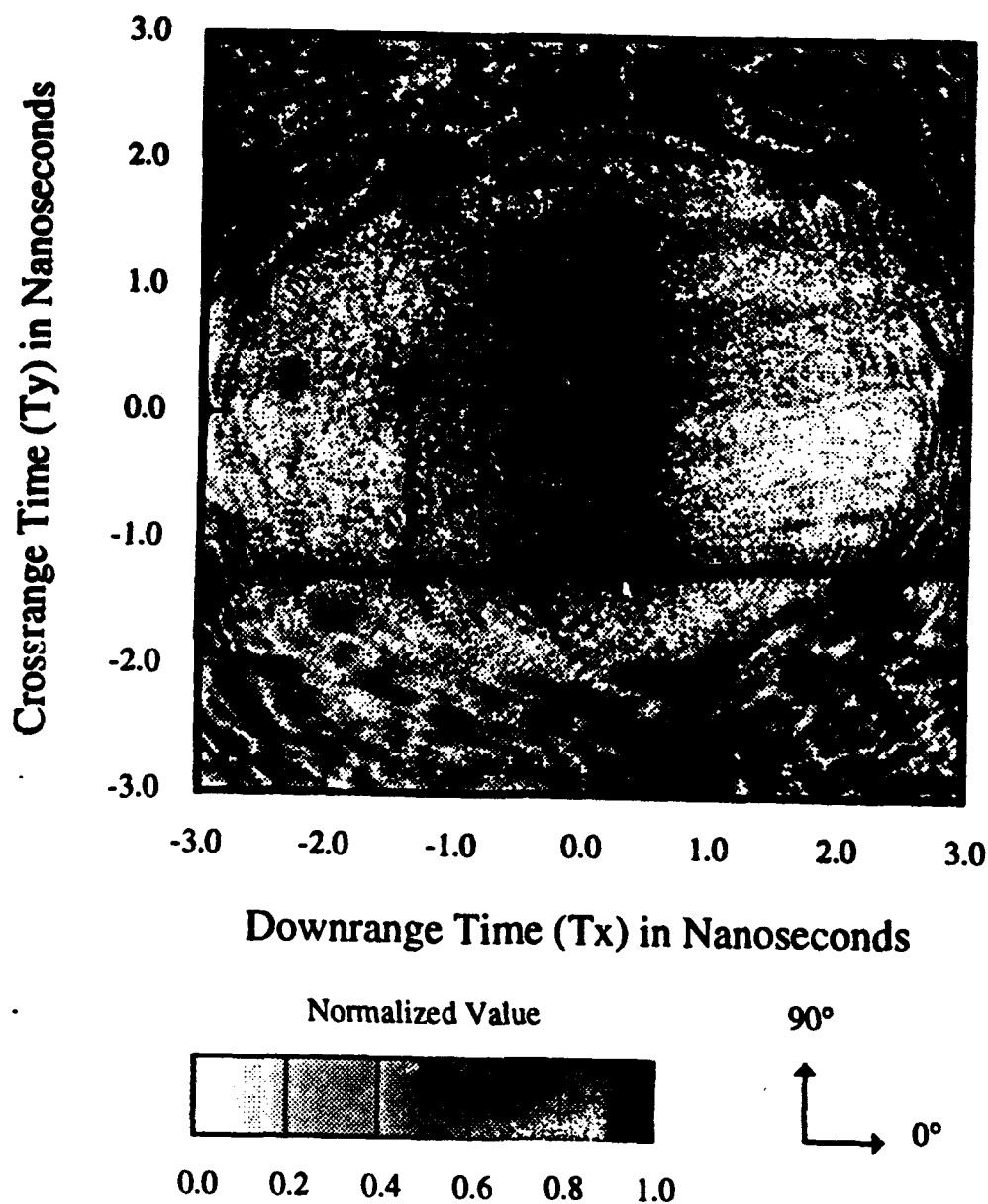Figure 43: Model M35 Truck, Time Domain Response, 0° Elevation, | $g(x,y)$ |, 90°(1°)270° VP.

Figure 44: Model M35 Truck, Convolution Backprojection Image, 0° Elevation, $|g(x,y)|$, 90°(1°)270° VP.
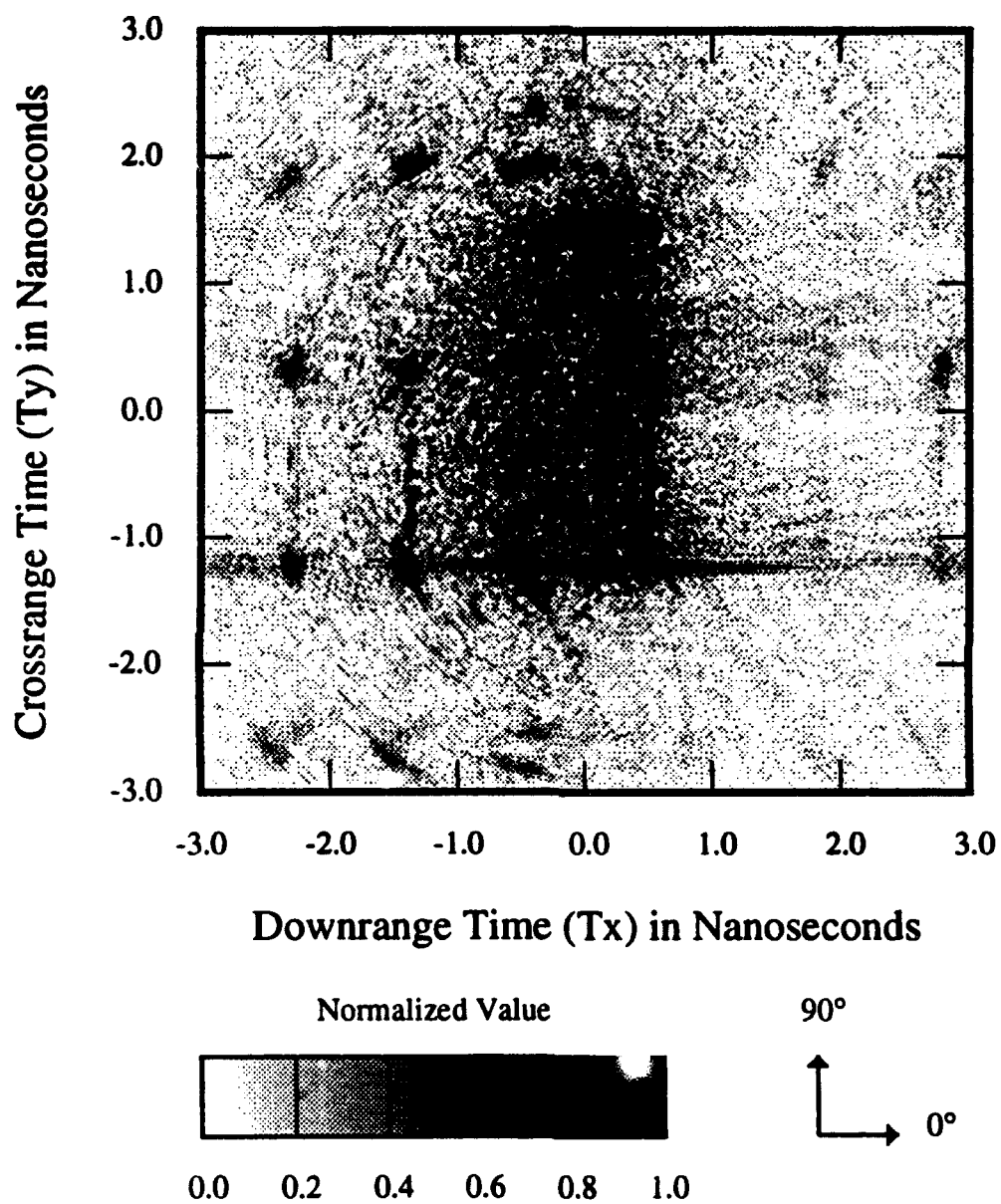
Figure 45: Model M35 Truck, Aliased Frequency Domain Interpolated Image, 0° Elevation, $|\ g(x,y)\ |$, 90°(1°)270° VP.
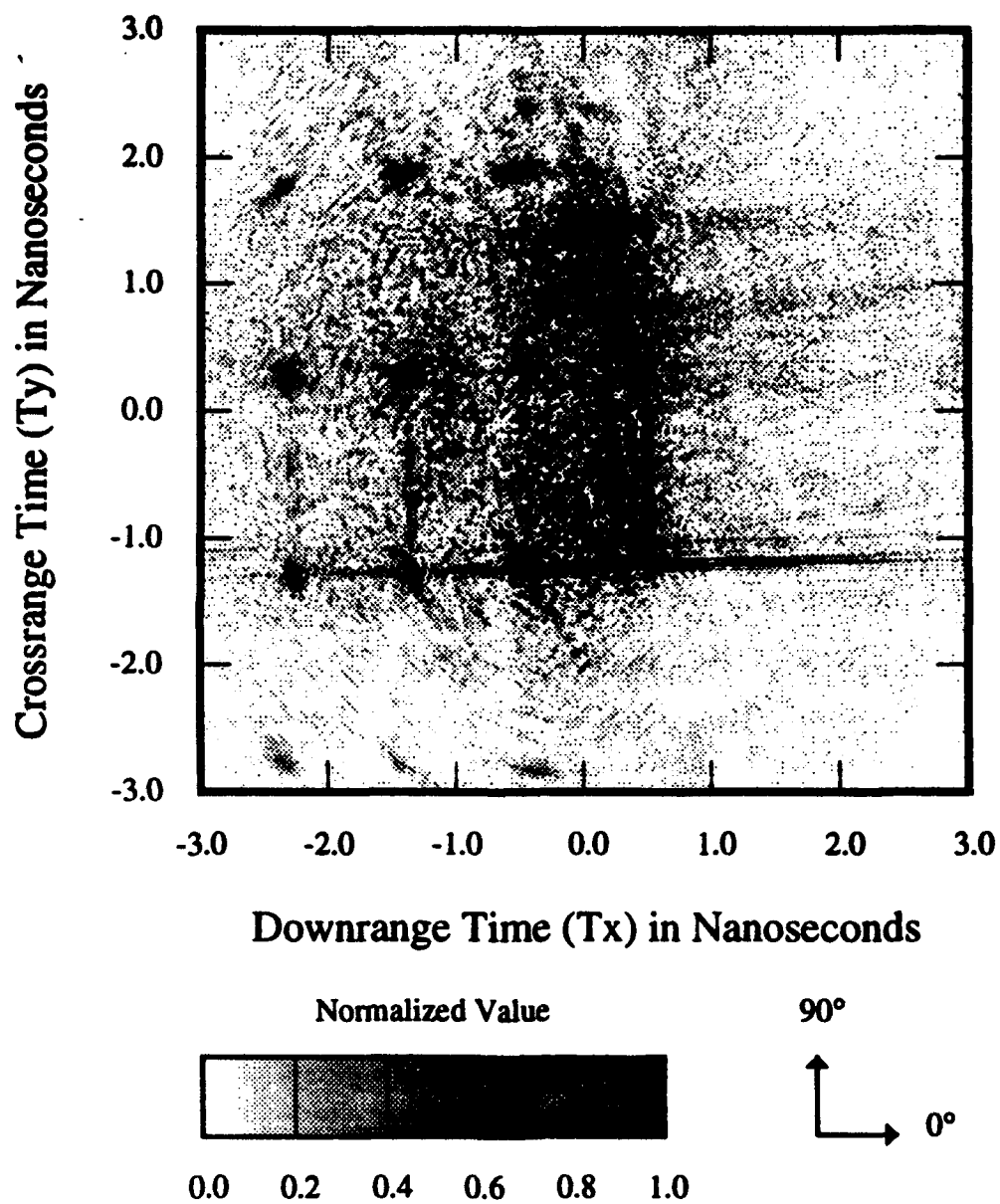
Figure 46: Model M35 Truck, Frequency Domain Interpolated Image, 0° Elevation, $| g(x,y) |$, 90°(1°)270° VP.
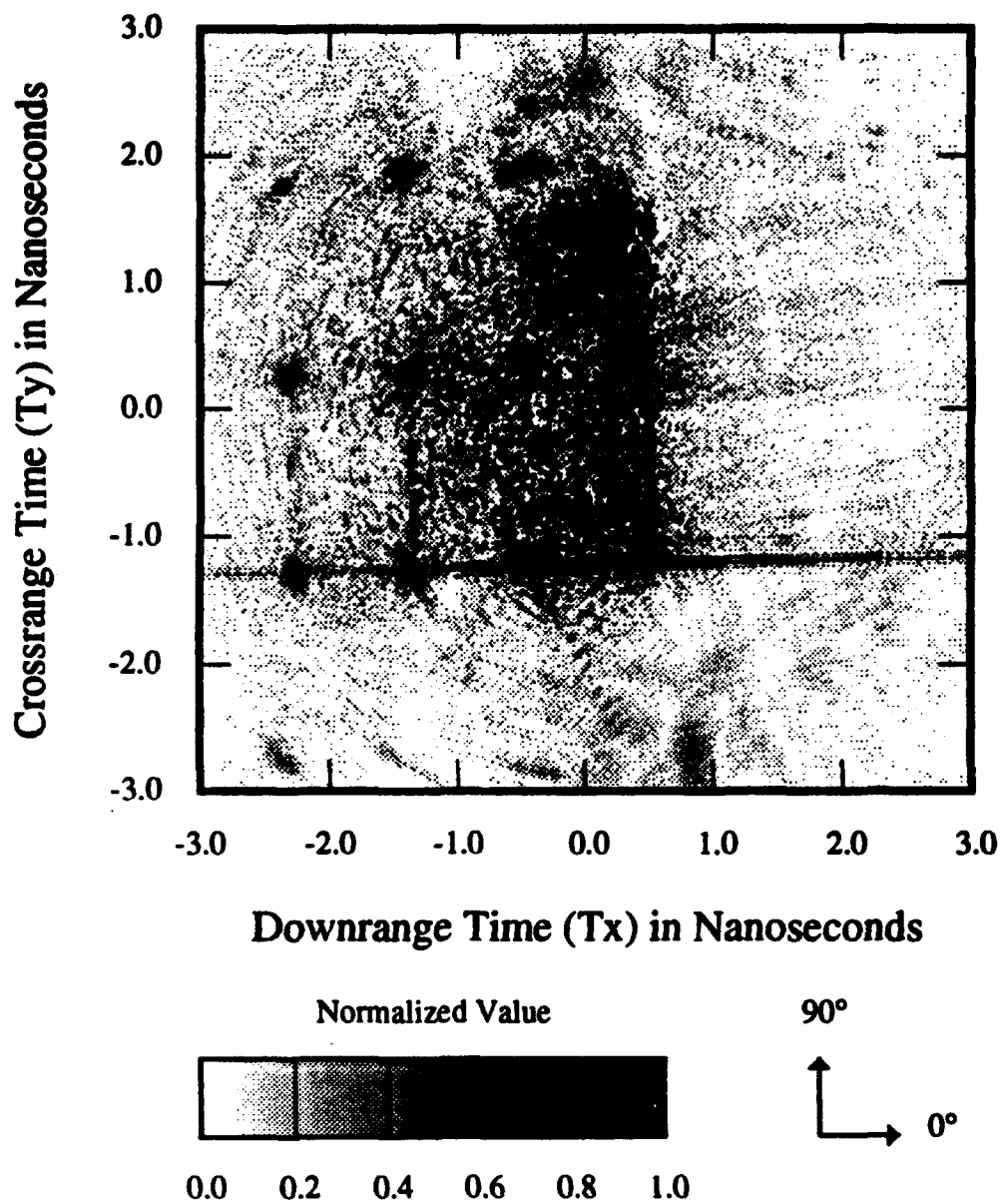
Figure 47: Model M35 Truck, Convolution Backprojection Image with Linear Interpolated Samples of 0.45°, 0° Elevation , | $g(x,y)$ |, 90°(1°)270° VP.

first order scattering mechanism, the scattering does not appear in the images as a dot. Instead, it appears as an arc in the image. In the images, the reverberations are seen as periodic arcs occurring outside of the truck. These reverberations are not part of the physical optics assumption in the imaging algorithm. As a result, the reverberations do not appear in the image at the location causing the scattering. Scattering centers that do not image to a point occur frequently. They are even more apparent in three dimensional imaging when there is insufficient sampling to completely characterize the target.

A cut of a three-dimensional image was done using the 45° elevation data. Figure 48 shows the truck imaged on the ground plane. Since the image was generated using only one elevation angle, there are many "fake" scattering centers at this elevation. These fake scattering centers actually occur at a different altitude. If more elevation angles are used, these fake scatters will disappear. Figure 49 shows the truck focused at 3 inches above the ground plane. Looking at these images, one can see that several of the fake scattering centers (of the 0 inch altitude images) become focused and are actually from a different elevation. Figure 50 shows an image at an altitude of 1.2 inches. The truck bed is located at this altitude and forms a dihedral scattering mechanism. The mechanism response is located at the vertex of the dihedral. When the image is focused at 1.2 inches, the image shows the proper location of the scattering center. At other elevations, this scattering center appears as a "fake."

As mentioned earlier, most fake scattering centers are seen because of insufficient data to completely characterize a target. Often in linear SAR, limited data are available to completely characterize a three-dimensional target.

5.3   SAR Imaging

A foliage penetration study was done at the Big Ear. A small forested area located behind the flat reflector was used. An extensive survey was made of the forest to
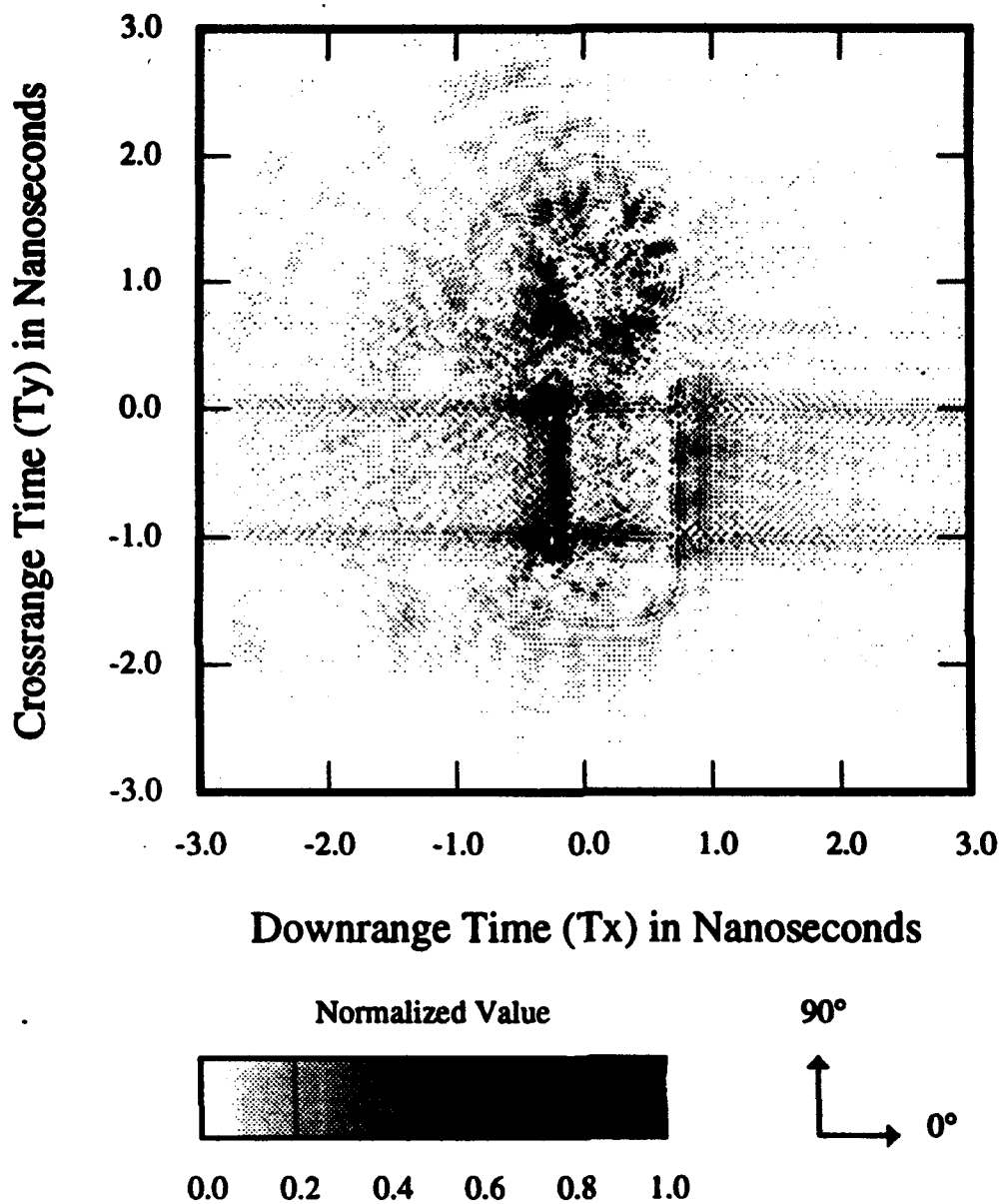
Figure 48: Model M35 Truck, Image on Ground Plane, 45° Elevation, $| g(x,y) |$, 90°(1°)270° VP.
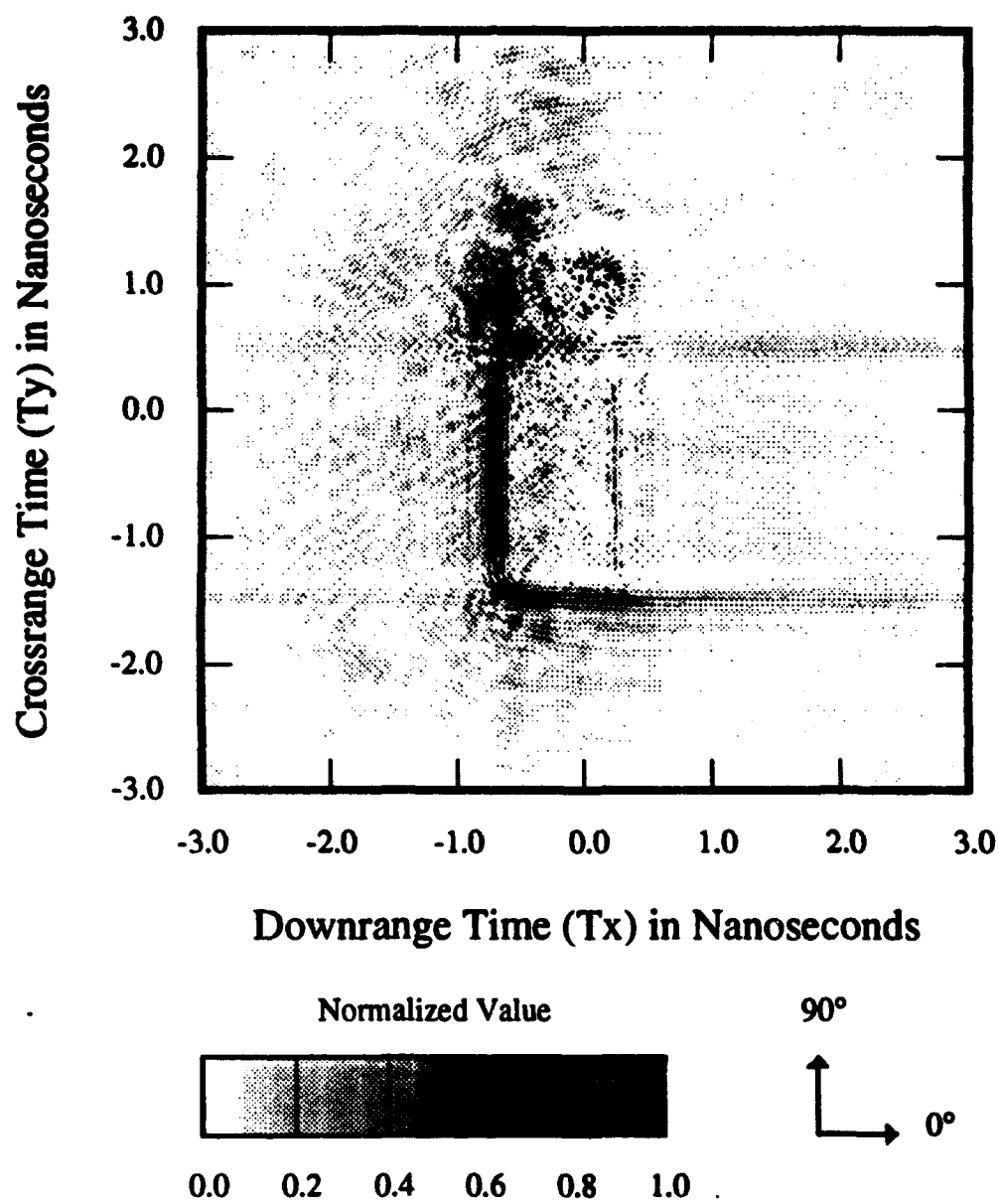
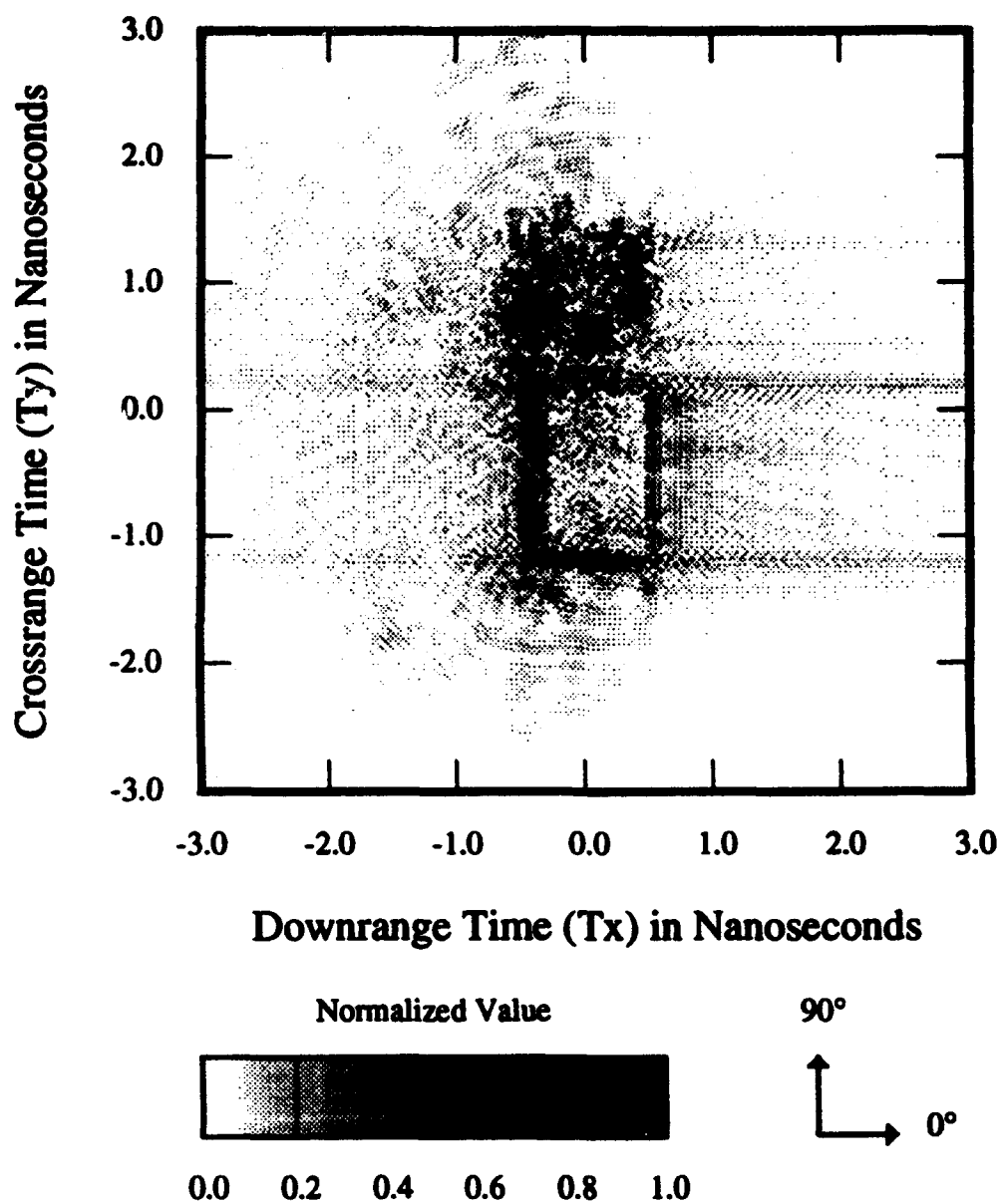Figure 49: Model M35 Truck, Image at 3-inch Elevation, 45° Elevation, $| g(x, y) |$, 90°(1°)270° VP.

Figure 50: Model M35 truck, Image at 1.2-inch Elevation, 45° Elevation, $| g(x,y) |$, 90°(1°)270° VP.
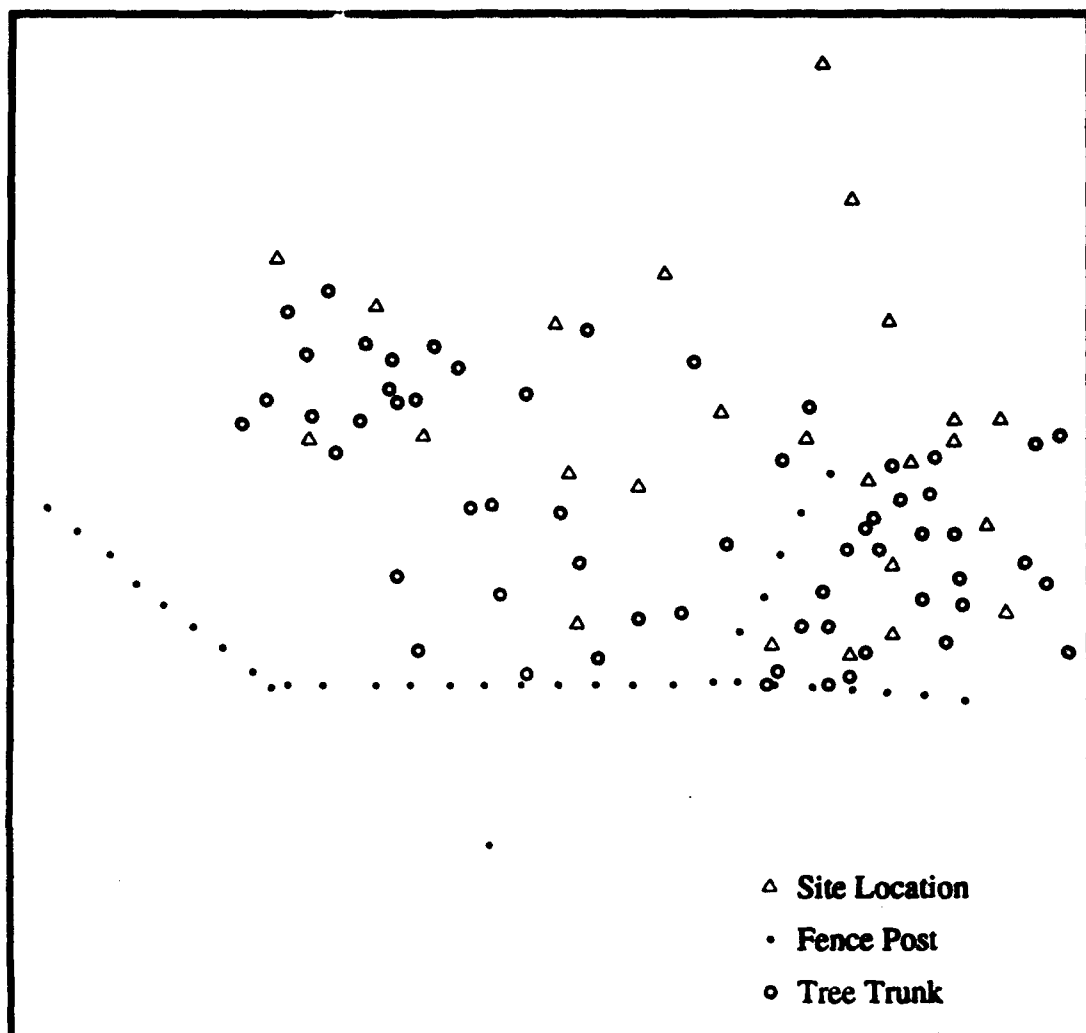
Figure 51: Map of SAR Target Area at the "Big Ear"

produce the map shown in Figure 51. Several small corner reflectors were placed
in the woods such as an 8-foot triangular plate trihedral and 4-foot square plate
trihedrals. Other reflectors were placed in the forest, and their descriptions are
shown in Table 2. A 2-foot dihedral was suspended in the air. The 2-foot dihedral
was used to calibrate the data. In addition, it was also left in the measurements to
provide a known reference location.

. Many measurements were made at the Big Ear. A maximum aperture size of
230 feet was measured. Both 4-inch and 6-inch sampling were measured using the

Table 2: Calibration Target Locations for 1304 and 1305 Data

Quantity	Corner Reflector Type
1	8-foot Triangular Plate Trihedral
3	4-foot Square Plate Trihedral
1	2-m x 1-m Dihedral
2	0.67 x 1-m Dihedral

system. Both time and frequency domain measurements, with a bandwidth of 200 MHz to 1600 MHz, were made of the target region at different times in the year. Measurements were made using a Horizontal E-field (HP) and Vertical E-field (VP). A list of the measured data is shown in Table 3. The data are represented by over 500 megabytes. Only one set of image data will be shown here. This particular data set has an aperture of 200 ft.

From Equation (77), one can conclude that a point scatter in the target region will track as a hyperbola when plotted as a function of the measurement position. Figures 52 through 55 show the time domain response of the foliage as a function of measurement position. These plots show calibrated data without range compensation and show 400nS of downrange distance. Figures 52 and 54 show the first 200nS of downrange distance while Figures 53 and 55 show the the remaining 200nS. Figures 52 and 53 show HP while Figures 54 and 55 show VP. As seen in the figures, the corner reflector response is significantly stronger than the trees. The bent vertical line in Figures 52 and 54 is a metal fence surrounding the forest. A lot of scattering centers are visible in the HP waterfall plot in Figures 52 and 53. However, there are significantly fewer scattering centers in VP, as seen in Figures 54 and 55.

Due to the large distances covered, the calibrated data need to be range compensated because of free space dispersion. The resulting data were then focused as

Table 3: Measured Foliage Data Sets

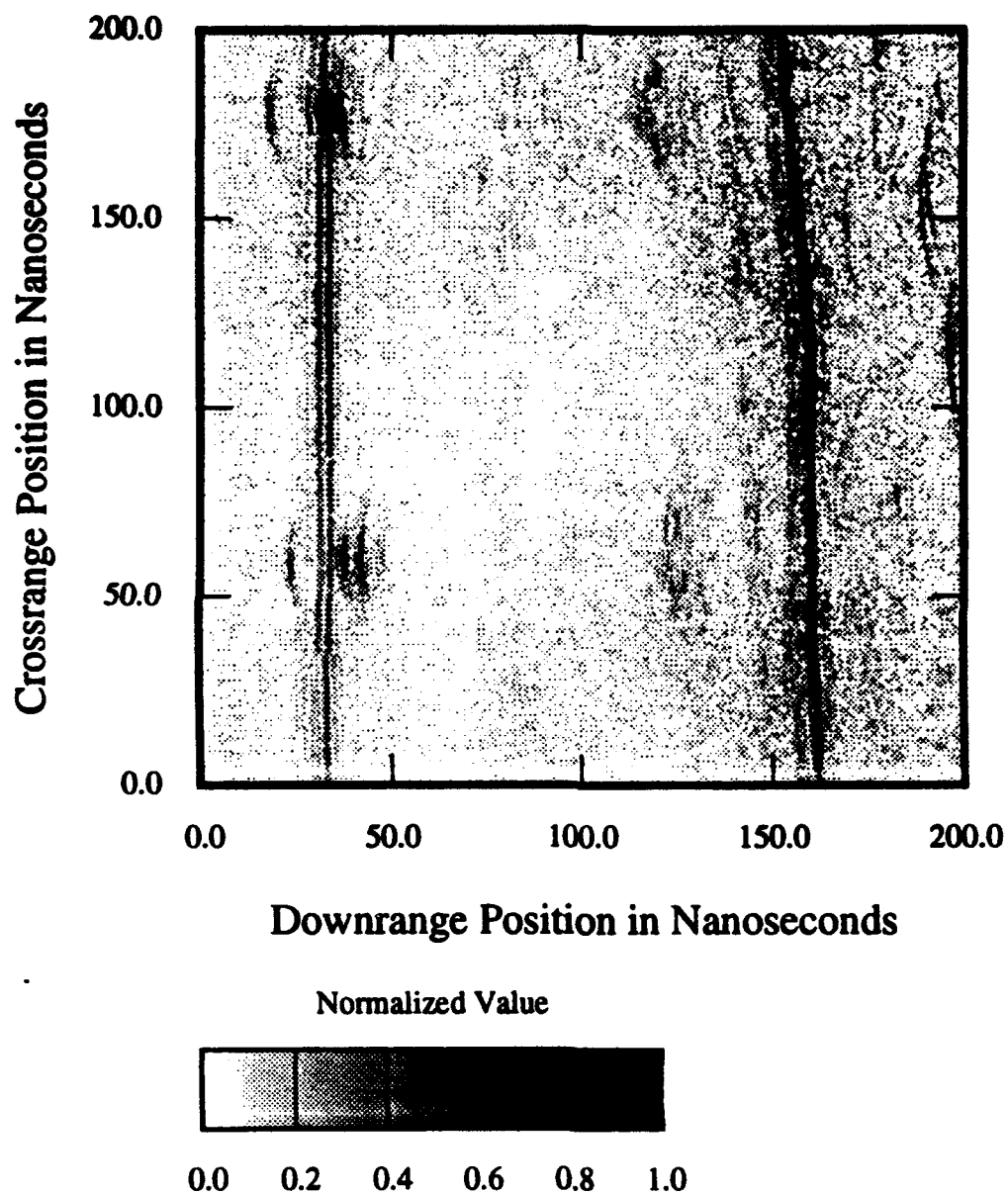| Data Set	Aperture Size in feet	Sample Spacing (in.)	Radar Type	Time of Year
1302	120	4	Frequency	Autumn
1303	120	6	Frequency	Autumn
1304 and 1305	200	6 6	Frequency	Autumn
1309	120	6	Frequency	Autumn
1310	120	4	Frequency	Autumn
1311	120	4	Frequency	Autumn
2161	200	6	Time	Spring
2163	200	6	Time	Spring
2168 and 2169	200	6	Frequency	Spring

Figure 52: SAR Image of Foliage, 6-inch Sampling, HP
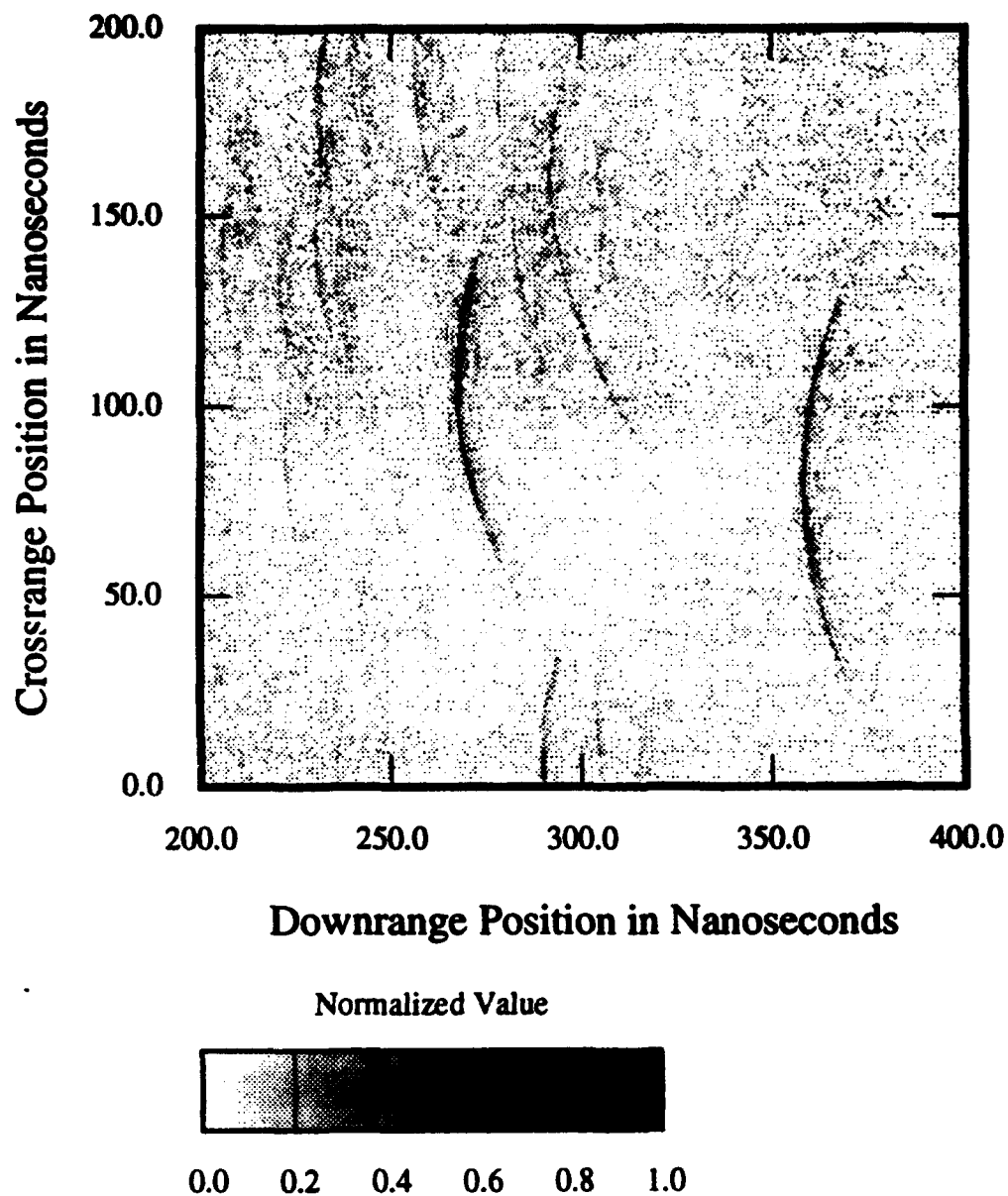
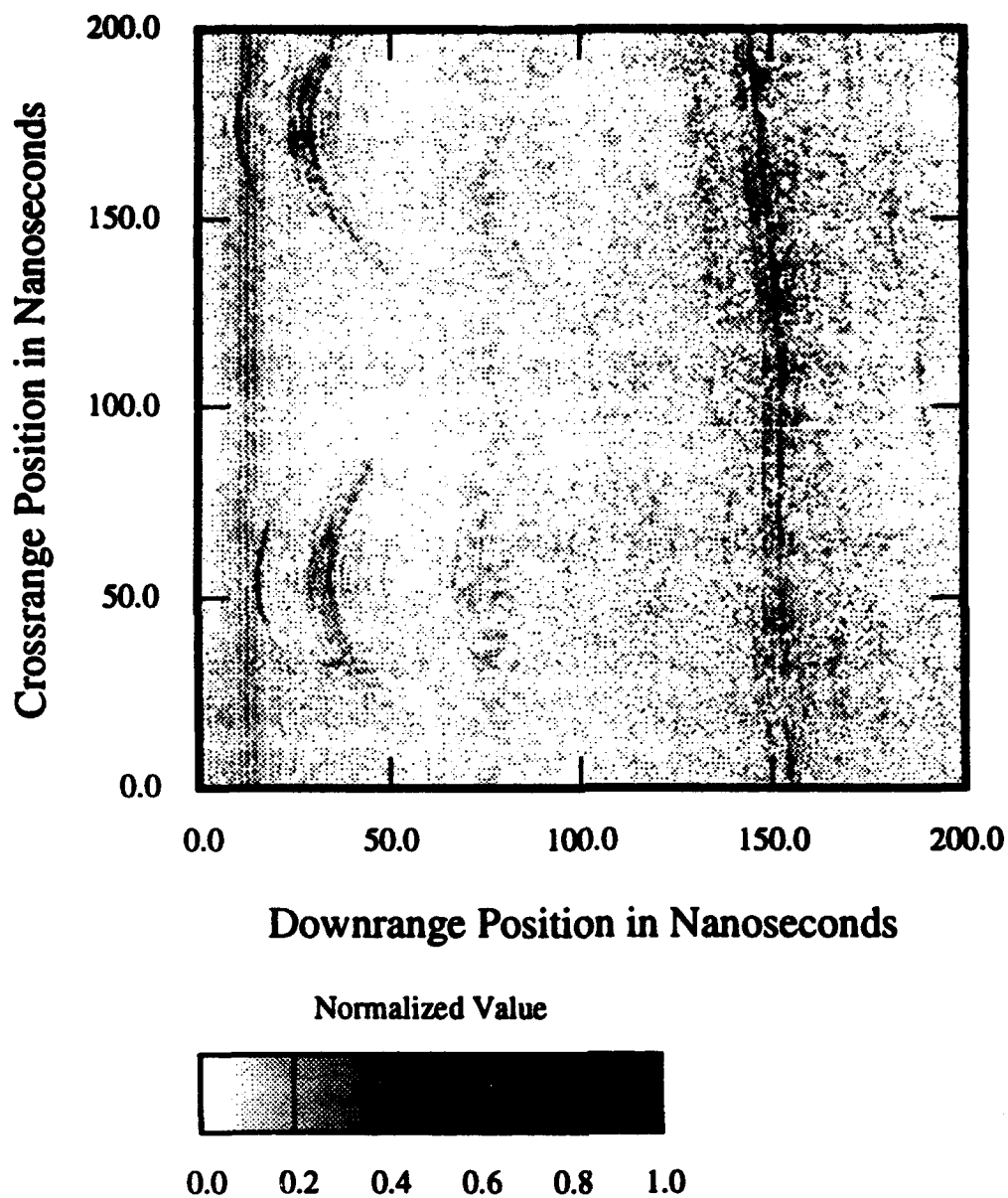Figure 53: SAR Image of Foliage, 6-inch Sampling, HP

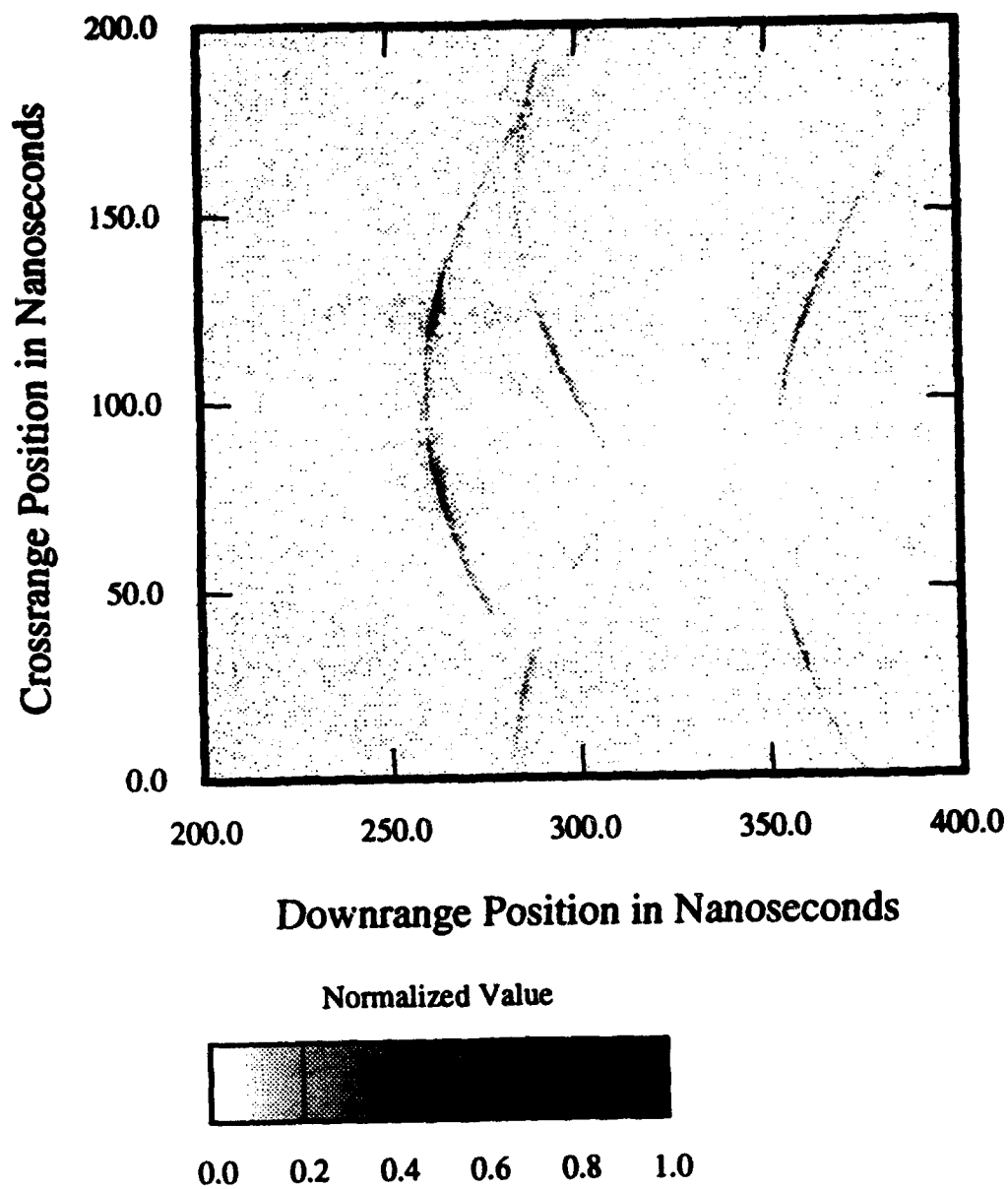Figure 54: SAR Image of Foliage, 6-inch Sampling, VP

Figure 55: SAR Image of Foliage, 6-inch Sampling, VP

a near-field SAR to produce images in the slant plane as shown in Figures 56 and 57. These images were made using Equation (78) with a finite aperture. The images show the scattering centers in the HP waterfall plot image as dots in the SAR image. Most of these dots correspond to the base of the tree trunk in the slant plane. The trunk scattering appears to dominate the response from the forest in HP but not in VP. In HP, the scattering mechanism that causes the trunk scattering is caused by a dihedral-like mechanism. The ground to tree trunk bounce is similar to a dihedral. A Brewster angle effect occurs in VP because of the angle of incidence with respect to the ground. Consequently, the ground reflection is too weak to cause the dihedral effect, [16].
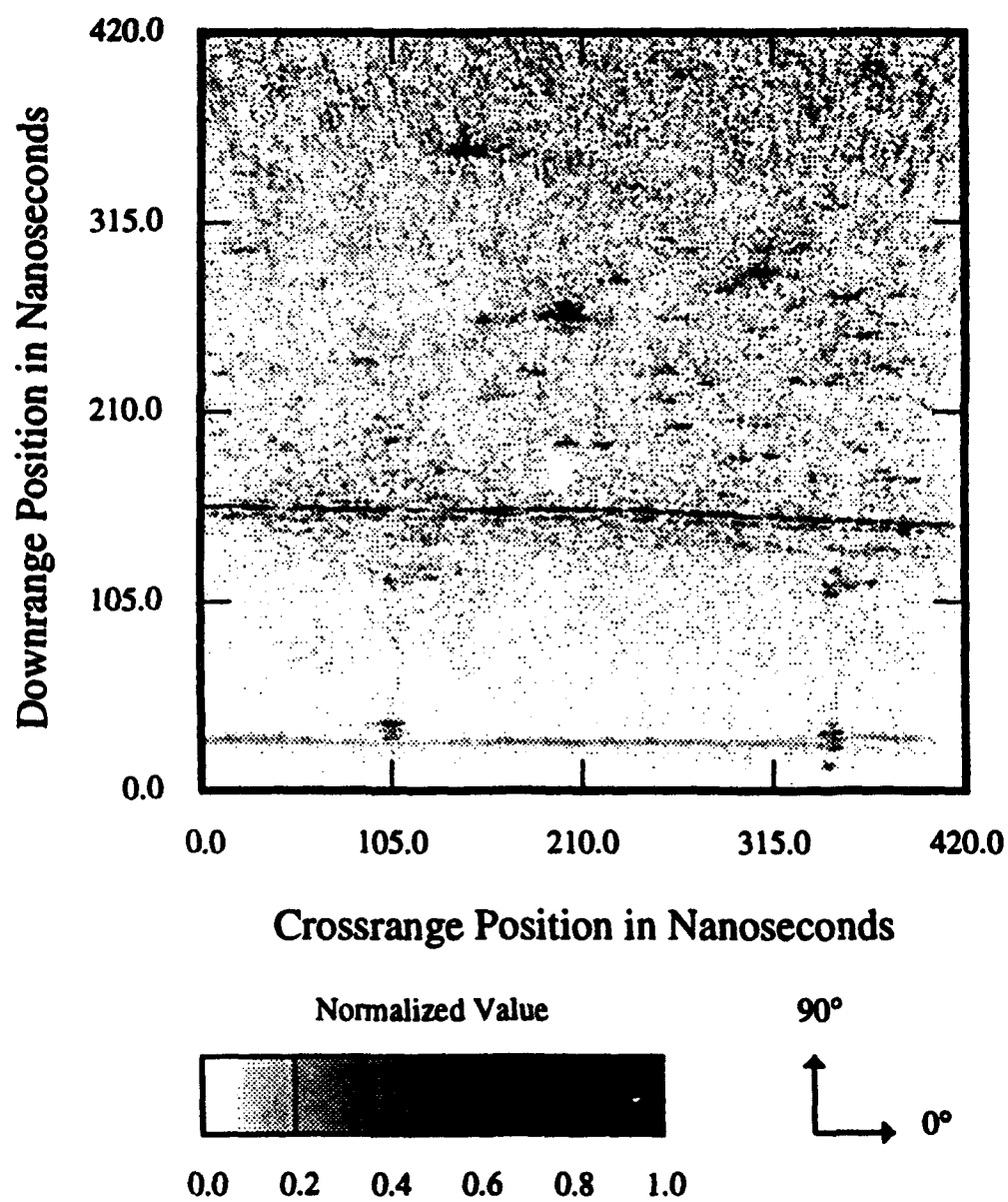
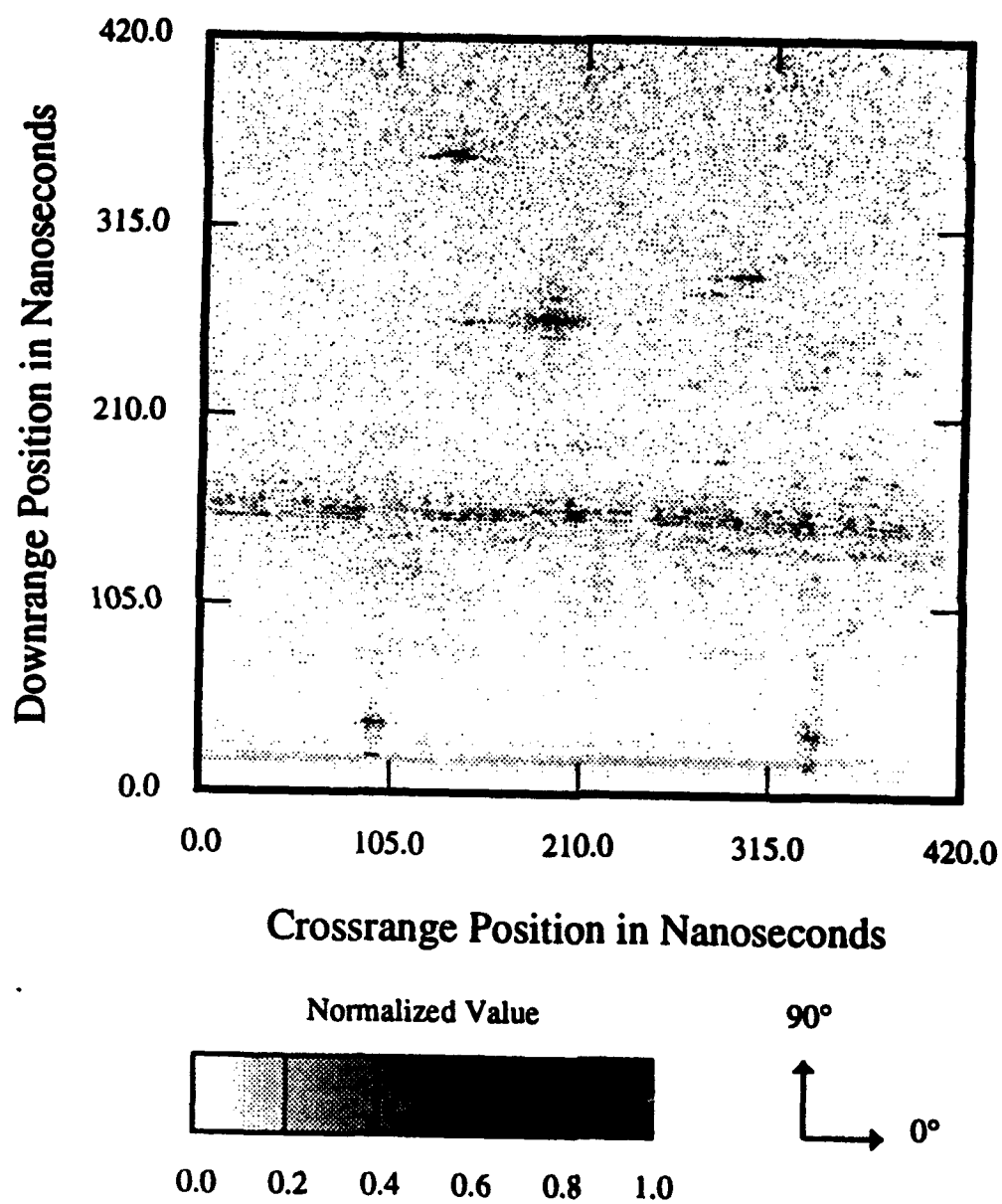Figure 56: SAR Image of Foliage, 6-inch Sampling, HP, $|g(x,y)|$

Figure 57: SAR Image of Foliage, 6-inch Sampling, VP, $| g(x,y) |$

SECTION 6

Conclusions

Fourier based imaging techniques were presented for certain radar geometries such as polarimetric ISAR and linear SAR. In these geometries, the reflectivity characterized by a target is preserved in the generated image. As a result, the image may be used to synthesize the measured data. These geometries described are often used in radar measurement facilities. The facilities at OSU, provide ultrawideband radar measurement systems. Measurement systems for scanning geometries described in this report are available at OSU. The facilities include an indoor compact range, an outdoor compact range (Big Ear), and an outdoor linear SAR system.

Images generated from measurement systems often contain noise. A practical implementation of the imaging algorithms also introduces some numerical noise. In addition, the algorithms also introduce image artifacts caused by Gibb's phenomena and sampling. Examples of these artifacts are shown in Chapters 4 and 5. Gibb's phenomena are suppressed by filtering the image. Traditional full bandwidth filters reduce the image clarity significantly. Instead, a tapered filter should be used. Figures 26 through 31 show these effects.

Filtering is used to improve the reader's perception of the image. Other methods of improving image perception are available. One main problem occurs because the human eye does not distinguish individual shades well. The eye enhances areas of high contrast. Images are usually presented in terms of the absolute value of the

reflectivity function. By including polarity information, perception of scattering centers may be increased. This is shown in Figures 22 through 24. Color images are usually made. However, color images could not be included in this report.

In Chapter 5, images are presented from measured data of the different scanning geometries. These images included a model F-4 fighter aircraft, a model M35 truck, and a forest. These images showed that a proper implementation of the two-dimensional Fourier Slice algorithm provided results as good as convolution backprojection as seen in Figures 33 and 35. Angular Nyquist artifacts can be seen readily in convolution backprojection in its image, Figure 40, and in its frequency domain representation, Figure 41. In addition, implemented Fourier Slice algorithm provided better suppression of sampling image artifacts, when the data were sampled near the angular Nyquist rate as seen in Figures 44 and 46. An equivalent convolution backprojection image can be made by interpolating the polar samples as seen in Figure 47. Although both Fourier Slice and convolution backprojection are mathematically equivalent and produce comparable results, the computer time used to generate the images are significantly different. As implemented in the computer program, convolution backprojection is 20 times slower than the Fourier Slice algorithm.

For data taken in a conical geometry, images were focused on different elevation planes. These images shown in Figures 48 and 50 demonstrate that the individual scattering centers are focused at the correct elevation.

SAR imaging was done in the slant plane for the measured data of foliage. In these SAR images, Figures 56 and 57, scatt- -- -: enters, such as tree trunks, can be easily identified in the images. By usin: ---zation information, a scattering mechanism, caused by a tree trunk ground interaction, was verified.

Other modifications to the basic imaging algorithm can be done. One such change is to focus the SAR image onto a patch of ground or at an arbitrary plane. Future work will include these changes. These changes should provide insight into foliage

scattering. In addition, nearly real-time image generation is currently being worked on for the Big Ear compact range.

REFERENCES

[1] W. D. Burnside, T. Barnum, P. Bohley, W. Lin, M. Poirier,P. Swetnam. *Operating Manual for the OSU/ESL Transceiver System*. Technical report number 719493, Electroscience Laboratory, The Ohio State University, February, 1989.

[2] J. D. Young, J. D. Kraus, R. Caldecott, M. Poirier, D. and Barnum. "The 'Big Ear' Radio Telescope as a Compact Radar Range," The Ohio State University ElectroScience Laboratory, Final Report 718606-2, prepared under contract no. F49682-86-C0018 for Research Projects Office (SAF/OR), Washington, DC, June 1987.

[3] J. S. Gwynne "An Assessment of Three Experimental Radar Scattering Measurement Systems Operating Below 2 GHz," M.S. Thesis, The Ohio State University 1991.

[4] J. S. Gwynne. "Time Domain Characterization of UWB Antennas," Antenna Measurement Techniques Association, 14th Annual Meeting and Symposium, The Ohio State University, October 19-23, 1992

[5] C. M. Glass. Selected Topics in Synthetic Aperture Radar. Goodyear Aerospace, AEEM-653, November 1986.

[6] S. Scarborough, "UltraWideband Radar Imaging and Diagnosis of Scattering Centers," M.S. Thesis, The Ohio State University, Electroscience Laboratory, September 1990.

[7] A. V. Oppenheim, A. S. Willsky, and I. T. Young. *Signal and Systems*. Prentic-Hall, Inc., New Jersey 1983.

[8] G. T. Herman, H. K. Tuy, K. J. Langenberg, and P. C. Sabatier. *Basic Methods of Tomography and Inverse Problems*. Adam Hilger, Philadelphia, 1987.

[9] D. Mensa. *High-Resolution Radar Cross-Section Imaging*. Artech House, Inc., Dedham, Massachusetts, 1991.

[10] M. Soumekh, "A System Model and Inversion for Synthetic Aperture Radar Imaging," *IEEE Transactions on Image Processing*, Vol. 1, No. 1, January 1982.

[11] J. L. Bauck and W. K. Jenkins. "Tomographic Processing of Spotlight-mode Synthetic Aperture Radar Signals with Compensation for Wavefront Curvature," *IEEE International Conference on Acoustics Speech and Signal Processing*, April 11-14, 1988.

[12] A. K. Jain. *Fundamentals of Digital Image Processing*. Prentice-hall, Inc. Englewood Cliffs, New Jersey, 1989.

[13] F. J. Harris "On the Use of Windows for Harmonic Analysis with the Discrete fourier Transform." *Proceedings of the IEEE*, Vol. 66, No.1 , January 1978.

[14] R. Harrington. *Time-Harmonic Electromagnetic Fields*. McGraw-Hill, 1961.

[15] G. M. Dural *Polarimetric ISAR Imaging to Identify Basic Scattering Mechanisms Using Transient Signatures*. Ph. D. Dissertation, The Ohio State University, 1988.

[16] A. A. Nowotarski "Electromagnetic Scattering from the Trunks and Branches of Trees," M.S. Thesis, The Ohio State University 1993.